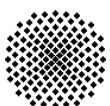


**Impact of neutron thermal scattering  
laws on the burn-up analysis of  
Supercritical LWR's fuel assemblies**

**Andrea Conti**





# **Impact of neutron thermal scattering laws on the burn-up analysis of Supercritical LWR's fuel assemblies**

Von der Fakultät Energie-, Verfahrens- und Biotechnik der Universität Stuttgart  
zur Erlangung der Würde eines  
Doktor-Ingenieurs (Dr.-Ing.) genehmigte Abhandlung

Vorgelegt von

**Andrea Conti**

aus Bozzolo (MN), Italien

Hauptberichter: Prof. G. Lohnert, Ph.D.

Mitberichter: Prof. Dr. ir. J. L. Kloosterman

Tag der Einreichung: 03. Dezember 2010

Tag der mündlichen Prüfung: 06. Juli 2011

ISSN – 0173 – 6892





## Acknowledgements

The realization of this project has been made possible fundamentally by Prof. G. Lohnert, who in 2003 looked on me as trustworthy enough to grant me a position as PhD student at the IKE, and by the Helmholtz Gemeinschaft, which financed my research.

The person who helped me the most in my concrete work has been Dr. W. Bernnat, who showed in these years to possess great selflessness and a nearly infinite patience. Bernnat offered me both theoretical consultancy and technical support in dealing with the computational means.

The experimental work core of this dissertation consists of burn-up simulations which have been carried out with reference to fuel element designs conceived at the IKET in the FZK. In particular, I have had the opportunity to severely test Dr. C. L. Waata's and Dr B. Vogt's willingness to provide any complementary information and to confront results.

I also would like to thank J. Martí from the Department of Physics and Nuclear Engineering, Technical University of Catalonia, for his consultancy on his Molecular dynamics simulations.

Special thanks go to Dr. A. Piater and Mr. J. C. Lapins, who gave me consultancy on how to consistently structure my results into a PhD thesis and boosted my morale in very difficult moments.

## Abstract

This work is a contribution of the Institut für Kernenergetik und Energiesysteme of the University of Stuttgart to the HPLWR2 (High Performance Light Water Reactor Phase 2), a research project sponsored by the European Union having the goal to investigate the technical feasibility of the High Performance Light Water Reactor.

The basic idea of the HPLWR is that of an LWR working at supercritical pressure, which would allow heating up the coolant to a temperature of about 500 °C without having phase transition and sending the coolant directly to the turbine.

There are three characteristics that make this concept, in principle, particularly attractive:

- 1) The very high coolant outlet temperature would make possible attaining high plant efficiency, which should be of about 44 %.
- 2) Like in a BWR, there would be no secondary circuit. Moreover, the fact that no phase transition would take place would allow a high simplification of the plant in comparison with the BWR, because recirculation pumps, steam separators and steam dryers would not be necessary.
- 3) The HPLWR would build upon the experience of the existing supercritical coal-fired plants.

The concurrence of these advantages would make this reactor particularly competitive from an economical point of view and it is just this economical competitiveness that led the Gen IV International Forum to select this design as one of the most promising candidates - together with other 5 - to be implemented as reactor of generation IV.

On the other hand, this design also aroused some issues that need to be addressed by additional research.

First of all, according to the layout adopted in Europe, the coolant should flow through the core passing from 280 °C at the inlet to 500 °C at the outlet, undergoing a density variation of a factor of about 9. This could imply a very asymmetrical power distribution. It is for this reason that all assembly geometries put forward since the beginning feature the so called “moderator channels”, through which part of the cold, dense inlet water should flow downwards acting as moderator. The rest of the water should flow downwards along the downcomer, mix up with the water coming out of the moderator channels and then flow upwards around the fuel rods acting as coolant.

Another source of concern regards the fidelity of the models applied to simulate the neutron transport in such a system.

The solution of the Boltzmann equation requires the knowledge of the laws that rule the neutron interactions with the nuclei in fuel, cladding, moderator and coolant. Representing the neutron state through its velocity and direction of flight, the mathematical representation of these laws consists in the distribution function of the average number of neutrons over the possible final states (that is, after the interaction with a nucleus) given the single incoming neutron initial state (that is, before the interaction), which is called “scattering kernel”.

The neutrons generated by fission slow down thanks most of all to collisions with the light nuclei of the moderator until they reach the thermal range of energies, where fission is most likely to occur.

In the case of elastic scattering, the relation between outgoing neutron’s direction and energy can be derived from the laws of classical mechanics, approximating matter as a mixture of standalone, free nuclei, because the binding energy of the nuclei to the respective molecule or crystal is usually much smaller than the slowing down neutrons’ kinetic energy and can therefore be neglected.

At thermal energies, the De Broglie wavelength associated with the neutron is comparable to the interatomic distances in crystals and molecules and the scattering is fully governed by the laws of quantum mechanics, according to which the geometry of the aggregates the nuclei are bound to and their intra- and intermolecular dynamics are of crucial importance.

So, it is necessary to switch to a second scattering kernel, which will be different depending on the structure the nucleus is bound to.

The geometry and the dynamics of the system for the purposes of quantum mechanics can be modelled through an appropriate choice of coordinates and the Hamiltonian built upon them. Therefore, according to this scheme, it should be possible to calculate the double-differential scattering cross section knowing the Hamiltonian of the system. Effectively, it is so.

In the case of vapour, the Hamiltonian is quite simple in its vibrational, rotational and translational parts, because one can neglect any intermolecular interaction.

In the liquid case, the molecule’s rotations, hindered by the interaction with the neighbours, can be modelled through a torsional harmonic oscillator, but the translational behaviour of the molecules is not yet well understood. In order to overcome the problem of the unknown parts of the Hamiltonian, some new methodology has been developed, which permits to take advantage of experimental measures without necessarily knowing the full Hamiltonian.

In particular it can be shown that there is a certain mathematical relation between the Fourier-transform of the hydrogen atoms' velocity autocorrelation function ( $\langle \mathbf{v}(t)\mathbf{v}(0) \rangle$ ) and their double-differential scattering cross section. This Fourier-transform, called "generalized frequency distribution", can be derived from experimental measurements and, effectively, Bernnat et al. of the Institut für Kernenergetik und Energiesysteme of the University of Stuttgart derived the generalized frequency distribution for liquid water on the basis of experimental results of Page and Haywood.

Unfortunately there exists no experimental facility nowadays to support a thorough work of this type on supercritical water and therefore the scattering kernel for thermal neutrons in supercritical water is unknown.

In criticality calculations involving supercritical water one can turn to one of the thermal scattering kernels available nowadays for hydrogen bound to the H<sub>2</sub>O molecule: for liquid water, for vapour or considering the nuclei of hydrogen as unbound (in a mixture including also unbound nuclei of oxygen of course). The third, most naïve option is called the "free gas approximation".

It is the goal of this work to make an estimate of the criticality calculations' inaccuracy due to the inadequate employed physical model and to determine which one of the available models can be the best replacement.

The accuracy of criticality calculations referring to the HPLWR is a problem that has already been raised in the past. In 2006 Waata published in her Ph.D. thesis the results of a coupled transport – thermal hydraulics calculation of a fuel element performed coupling MCNP (Monte Carlo N-Particle Transport Code System) and STAFAS (Sub-channel Thermal-hydraulic Analysis in Fuel Assemblies under Supercritical conditions) and pursuing the convergence of the axial power profile through the iteration of alternating runs of the two programs.

Given the lack of specific libraries for the thermal treatment of the neutrons in supercritical water, Waata opted for the free gas approximation, implicitly assuming it as a "neutral" option.

In her thesis Waata sifts through the factors that can affect her MCNP runs' accuracy, but leaves the inappropriate thermal treatment completely out.

In this work, the approach to the estimate of the criticality calculations' results inaccuracy has been determined through certain assumptions.

First of all, it was assumed that the variability of criticality calculations results in dependence of the available thermal cross sections should be a good index of the magnitude of the inaccuracy due to the inadequate thermal scattering treatment. Hence the

idea to assess this inaccuracy carrying out, in principle, three criticality calculations differing from each other only in the applied thermal scattering kernel.

Second, it was assumed that the magnitude of the results' inaccuracy (not only the results themselves, which is clear) is influenced by the water density. Hence the plan to repeat the above-mentioned simulations implementing different coolant and moderator densities.

Third, it was assumed that the inaccuracy is also influenced by the fuel composition. Hence, in principle, the repetition of the above mentioned criticality simulations implementing different levels of fuel burn up, that is, in practice, their replacement with burn up simulations.

The fact that the burn-up simulations must be 2-dimensional, in order to isolate the influence of the above mentioned factors from other interfering phenomena rounded off the research methodology guidelines.

The burn-up simulations were carried out referring to Bittermann's so-called "square" geometry. In particular, the configurations of the fuel assembly's top and bottom layers were implemented.

The largest discrepancies between the results obtained with different thermal scattering kernels were detected for the bottom layer (where the average water density is highest) and for fresh fuel:  $\Delta\rho \approx -0.64$  \$ between liquid and free gas models,  $\Delta\rho \approx -0.40$  \$ between vapour and free gas models,  $\Delta\rho \approx -0.25$  \$ between liquid and vapour models.

The remarkable gaps between the free gas and the other two models in conjunction with the fact that the free gas does not even keep in count the molecular structure of H<sub>2</sub>O suggested to discard it and to focus the investigation on the vapour and liquid models.

One of the advantages of the method based on the generalized frequency distribution is that it is possible to computationally simulate the behaviour of a limited number of molecules in a given thermodynamic state and to register the generalized frequency distribution associated to the simulated movement.

Therefore, in this work, the search for the best thermal cross section set for supercritical water has been pursued through the search for molecular dynamics simulations reports in the literature.

The most useful data for the scope of this work were found in an article written by Dr. J. Martí (1999), from the Universitat Politècnica de Catalunya, Barcelona, Spain, who registered the generalized frequency distributions obtained from the molecular dynamics simulations of 216 molecules of H<sub>2</sub>O in 10 simulated supercritical states and published in numerical format the frequencies of the three characteristic distribution peaks for each simulated state.

A confrontation with the corresponding peaks from Bernnat's available frequency distributions for liquid water and vapour revealed the peaks of the latter to be closest to the supercritical water ones in nearly all cases. Hence the inference that thermal cross section sets for vapour are for the time being the best replacement for the missing thermal cross section sets for supercritical water.

This conclusion can not be considered definitive because molecular dynamics simulations' results are strongly dependent on the models adopted to reproduce the intra- and intermolecular interactions. Moreover, once a model has been chosen, a number of parameters must be appropriately set and, though the availability of some experimental data that can be used as reference, the trimming is usually problematic.

Nevertheless, an assuring argument reinforcing this conclusion is the ascertainment that criticality calculations results obtained applying different molecular models of H<sub>2</sub>O (that is, no free gas) in general do not differ very much from each other and therefore it seems that the most important factor influencing the results is the molecular structure of H<sub>2</sub>O, rather than the collective behaviour of the molecules, which is what sets supercritical water apart from vapour.

## Kurzfassung

Diese Arbeit stellt einen Beitrag des Institut für Kernenergetik und Energiesysteme der Universität Stuttgart zum HPLWR2 (High Performance Light Water Reactor Phase 2) dar, einem von der europäischen Union geförderten Forschungsprojekt mit dem Ziel, die technische Machbarkeit vom High Performance Light Water Reactor zu ermitteln.

Der HPLWR wäre prinzipiell ein mit superkritischem Wasser betriebener LWR. Der superkritische Betriebsdruck würde ermöglichen, das Kühlmittel ohne Phasenübergang bis auf eine Temperatur von ungefähr 500 °C zu erwärmen und es danach direkt auf die Turbine zuzuleiten.

Drei Eigenschaften machen dieses Konzept, prinzipiell, besonders interessant:

- 1) Die sehr hohe Kühlmittelaustrittstemperatur würde einen hohen Kraftwerkswirkungsgrad ermöglichen, der ungefähr 44 % betragen soll.
- 2) Wie in einem SWR, gäbe es keinen Sekundärkreislauf. Außerdem würde der ausbleibende Phasenübergang eine erhebliche Vereinfachung der Kraftwerksauslegung im Vergleich zum SWR ermöglichen, da keine Umwälzpumpen, Dampfseparatoren und Dampftrockner notwendig wären.
- 3) Die Auslegung des HPLWR würde von der Erfahrung mit den superkritischen Kohlekraftwerken profitieren.

Das Zusammenkommen dieser Vorzüge würde diesen Reaktor wirtschaftlich besonders wettbewerbsfähig machen und es ist ausgerechnet diese wirtschaftliche Wettbewerbsfähigkeit, die das Gen IV International Forum dazu veranlagte, dieses Design als einer der interessantesten Bewerber – gemeinsam mit weiteren fünf – für die Umsetzung in einen Reaktor der Generation IV auszuwählen.

Andererseits hat dieses Design auch manche Fragen aufgeworfen, deren Bewältigung weitere Forschung benötigt.

Zuerst, sieht die europäische Auslegung vor, dass das Kühlmittel im Reaktor von einer Eintrittstemperatur von 280 °C auf eine Austrittstemperatur von 500 °C erhitzen soll. Dadurch soll sich die Kühlmitteldichte um einen Faktor von ungefähr 9 verändern. Das wäre die Voraussetzung für eine sehr unausgewogene Leistungsverteilung. Deswegen, weisen alle von Anfang an vorgebrachten Brennelementgeometrien die Anwesenheit von den sogenannten „ModeratorKanälen“ auf, durch die ein Anteil des kalten, dichten Speisewassers nach unten fließen und dabei als Moderator wirken soll. Das übrige Wasser soll durch den Downcomer nach unten fließen, sich mit dem aus den Moderatorka-

nälen herausfließenden Wasser vermischen und dann als Kühlmittel nach oben um die Brennstäbe fließen.

Weitere Sorge bereitet die Frage der Realitätsnähe der Modelle, die eingesetzt werden, um den Neutronentransport in einem derartigen System zu simulieren.

Die Lösung der Boltzmann-Gleichung setzt die Kenntnis der Gesetze voraus, die die Wechselwirkung der Neutronen mit den Atomkernen im Brennstoff, Brennelementhüllen, Moderator und Kühlmittel beschreiben. Stellt man den Neutronenzustand mittels seiner Geschwindigkeit und Richtung dar, besteht die mathematische Formulierung dieser Gesetze in der Verteilungsfunktion der durchschnittlichen Anzahl Neutronen über die erreichbaren Neutronenzustände (das heißt, nach dem Streuakt) in Abhängigkeit vom jeweiligen Neutronenausgangszustand (das heißt, vor dem Streuakt), welche als „Streukern“ bezeichnet wird.

Die Spaltneutronen werden überwiegend mittels Streuung mit den leichten Atomkernen des Moderators gebremst, bis sie den thermischen Bereich erreichen, wo die Kernspaltung am wahrscheinlichsten auftritt.

Die Beziehung zwischen Richtung und Energie des aus dem elastischen Streuakt kommenden schnellen Neutrons kann von den Gesetzen der klassischen Mechanik abgeleitet werden, wobei die Materie annäherungsweise als eine Mischung freier einzelner Atomkerne modelliert werden kann, da die Bindungsenergie der Atome zum jeweiligen Molekül oder Kristallgitter normalerweise viel kleiner ist, als die kinetische Energie der schnellen Neutronen und darf also vernachlässigt werden.

Im thermischen Bereich ist die mit dem Neutron assoziierte De Broglie-Wellenlänge mit den Atomabständen in Kristallgittern und Molekülen vergleichbar und die Streuung wird ausschließlich von den Gesetzen der Quantenmechanik beschrieben, nach denen die Geometrie der Strukturen an die die Atomkerne angebunden sind und ihre intra- und intermolekulare Dynamik von höchster Wichtigkeit sind.

Man muss also zu einem zweiten Streukern wechseln, der von der jeweiligen Struktur, an die der Atomkern angebunden ist, abhängig sein wird.

Die Geometrie und die Dynamik des Systems zum quantenmechanischen Zwecke werden durch die Wahl geeigneter generalisierter Koordinaten und die darauf basierende Hamilton-Funktion dargestellt. Deswegen, nach diesem theoretischen Gerüst, soll die Ableitung des doppeltdifferentiellen Wirkungsquerschnittes anhand der Kenntnis der Hamilton-Funktion möglich sein. Es ist tatsächlich so.

In dem Fall von Dampf ist die Hamilton-Funktion ziemlich simpel in seine Schwingungs-, Rotations- und Translationskomponenten gegliedert, da jegliche intermolekulare Wechselwirkung zu vernachlässigen ist.

In dem Fall des flüssigen Zustandes dürfen die Rotationsbewegungen als harmonische Drehschwingungen modelliert werden, die translatorischen Bewegungen der Moleküle sind jedoch noch nicht völlig verstanden. Um das Problem der unbekanntenen Teile der Hamiltonian-Funktion zu bewältigen wurde ein neuer Ansatz entwickelt, um von experimentellen Untersuchungen zu profitieren ohne notwendigerweise die vollständige Hamilton-Funktion zu kennen.

Im Besonderen kann man zeigen, dass eine gewisse mathematische Beziehung zwischen der Fourier-Transformierten der Autokorrelationsfunktion der Wasserstoffatomengeschwindigkeit ( $\langle \mathbf{v}(t)\mathbf{v}(0) \rangle$ ) und ihrem doppeltdifferenziellen Wirkungsquerschnitt besteht. Diese Fourier-Transformierte, die „generalisierte Frequenzverteilung“ bezeichnet wird, kann anhand von Versuchsmesswerten abgeleitet werden und, in der Tat, leiteten Bernnat et al. vom Institut für Kernenergetik und Energiesysteme der Universität Stuttgart die generalisierte Frequenzverteilung für flüssiges Wasser aus Versuchsergebnissen von Page und Haywood her.

Es besteht heutzutage leider keine Einrichtung, die eine vollständige derartige Arbeit an superkritischem Wasser ermöglicht, deswegen bleibt der Streukern für thermische Neutronen in superkritischem Wasser unbekannt.

Bei Kritikalitätsberechnungen mit superkritischem Wasser kann man auf einen der heutzutage für an das H<sub>2</sub>O-Molekül gebundenes Wasserstoffatom verfügbaren thermischen Streukerne ausweichen: Für flüssiges Wasser, für Dampf oder für ungebundene Wasserstoffatomkerne (wohlgemerkt in einer auch ungebundene Sauerstoffatomkerne enthaltenden Mischung). Das dritte, naivste Modell wird „free gas approximation“ bezeichnet.

Die Ziele dieser Arbeit sind es, die durch das ungeeignete eingesetzte physikalische Modell bedingte Ungenauigkeit der Kritikalitätsberechnungen abzuschätzen und zu bestimmen, welches der vorhandenen Modelle den besten Ersatz darstellt.

Das Problem der Ungenauigkeit von auf den HPLWR beziehenden Kritikalitätsberechnungen wurde schon in der Vergangenheit aufgeworfen. 2006 veröffentlichte Waata in ihrer Doktorarbeit die Ergebnisse einer gekoppelten neutronischen und thermohydraulischen Berechnung eines Brennelementes, die durch die Kopplung von MCNP (Monte Carlo N-Particle Transport Code System) und STAFAS (Sub-channel Thermal-hydraulic Analysis in Fuel Assemblies under Supercritical conditions) durchgeführt wurde, wobei die Konvergenz des axialen Leistungsprofils durch die Iteration wechselseitiger Ausführungen der zwei Programme verfolgt wurde.

Mangels einer Wirkungsquerschnittenbibliothek für thermische Neutronen im superkritischen Wasser setzte Waata die „free gas approximation“ ein. Dadurch nahm Waata implizit die „free gas approximation“ als eine „neutrale“ Wahl an.

In ihrer Dissertation geht Waata die Faktoren durch, die zu der Ungenauigkeit ihrer MCNP-Ausführungen beitragen können, lässt aber die ungeeignete Behandlung der thermischen Neutronen völlig aus.

In dieser Arbeit wurde die Vorgehensweise zur Abschätzung der Ungenauigkeit der Kritikalitätsberechnungen mithilfe einiger Annahmen bestimmt.

Erst einmal wurde angenommen, die durch die Anwendung der verschiedenen verfügbaren thermischen Wirkungsquerschnitten bedingte Streuung der Kritikalitätsberechnungsergebnisse sei ein realistischer Index ihrer Ungenauigkeit aufgrund ungeeigneter angewendeter thermischer Einstellung. Daher die Idee, diese Ungenauigkeit prinzipiell mithilfe der Durchführung dreier Kritikalitätsberechnungen abzuschätzen, die sich voneinander nur in dem angewendeten thermischen Streukern unterscheiden.

Zweitens, wurde angenommen, die Größe der Ungenauigkeit der Ergebnisse (nicht nur die Ergebnisse selbst, welches selbstverständlich ist), werde von der Wasserdichte beeinflusst. Daher der Plan, die obengenannten Simulationen mit jeweils unterschiedlichen Kühlmittel- und Moderatorichte zu wiederholen.

Drittens wurde angenommen, die Ungenauigkeit werde auch von der Brennstoffzusammensetzung beeinflusst. Daher, im Prinzip, die Wiederholung der obengenannten Kritikalitätsberechnungen mit unterschiedlichen Abbrandwerten, das heißt, ihre prinzipielle Ersetzung durch Abbrandrechnungen.

Die Untersuchungsvorgehensweise wurde mit der Vorstellung vollendet, dass die Abbrandsimulationen 2-dimensional sein müssten, um die Wirkung der obengenannten Einstellungen von anderen Störfaktoren zu isolieren.

Die Abbrandsimulationen wurden in Bezug auf Bittermanns sogenannte „square geometry“ angestellt. Im Besonderen wurden die Konfigurationen entsprechend der oberen und unteren Schichten des Brennelementes implementiert.

Die höchsten Diskrepanzen unter den mit unterschiedlichen thermischen Streukernen erhaltenen Ergebnissen wurden bezüglich der unteren Schicht (wo die Mitteldichte des Wassers am höchsten ist) und für frischen Brennstoff festgestellt:  $\Delta\rho \approx -0,64$  \$ zwischen dem Flüssigkeits- und dem Freigasmodell,  $\Delta\rho \approx -0,40$  \$ zwischen dem Dampf- und dem Freigasmodell,  $\Delta\rho \approx -0,25$  \$ zwischen dem Flüssigkeits- und dem Dampfmodell.

Die erheblichen Abstände zwischen dem Freigas- und den anderen zwei Modellen zusammen mit der Tatsache, dass das Freigasmodell die Molekulare Struktur des H<sub>2</sub>O

nicht beachtet, wiesen darauf hin, das Freigasmodell auszuschließen und den Forschungsbereich auf das Dampf- und das Flüssigkeitsmodell einzugrenzen.

Ein Vorzug der auf der generalisierten Frequenzverteilung basierten Methode, ist die Möglichkeit, mit dem Computer die Dynamik einer begrenzten Anzahl Moleküle in einem gewissen thermodynamischen Zustand zu simulieren und dabei die aus der simulierten Bewegung der Moleküle entstehende generalisierte Frequenzverteilung aufzuzeichnen.

Deswegen wurde in dieser Arbeit die Ermittlung der besten thermischen Wirkungsquerschnitte für superkritisches Wasser durch die Recherche von Molekulardynamiksimulationen in der Literatur verfolgt.

Die zweckdienlichsten Daten wurden in einem Artikel von Dr. J. Martí (1999), der Universität Politècnica de Catalunya, Barcelona, Spanien gefunden. Martí hatte die Molekulardynamiksimulationen von 216 H<sub>2</sub>O-Molekülen in 10 superkritischen Zuständen durchgeführt, die jeweils daraus entstehende generalisierte Frequenzverteilung berechnet und die Frequenzen ihrer drei charakteristischen Spitzen für jeden simulierten Zustand in numerischem Format tabellarisch veröffentlicht.

Ein Vergleich mit den entsprechenden Maxima aus Bernnats Frequenzverteilungen für flüssiges Wasser und Dampf zeigte, dass die Spitzen der Frequenzverteilungen für Dampf denjenigen für superkritisches Wasser in fast allen Fällen nächstliegend sind. Daraus die Folgerung, dass thermische Wirkungsquerschnittenbibliotheken für Dampf im Augenblick den besten Ersatz für die fehlenden thermischen Wirkungsquerschnittenbibliotheken für superkritisches Wasser darstellen.

Dieser Schluss darf nicht als endgültig betrachtet werden, denn die Ergebnisse von Molekulardynamiksimulationen sind von den angenommenen Modellierungen der intra- und intermolekularen Wechselwirkungen stark abhängig. Außerdem, muss eine Reihe Parameter sachgemäß abgestimmt werden nachdem ein Model angenommen worden ist und, trotz der Verfügbarkeit manch experimenteller Daten, die als Bezugswerte dienen können, ist gewöhnlich die Einstellung problematisch.

Gleichwohl gibt es ein Vertrauen erweckendes Argument, das diesen Schluss festigt und zwar, dass Kritikalitätsrechnungsergebnisse, die mit unterschiedlichen Molekularmodellen des H<sub>2</sub>O (das heißt, keinem Freigasmodell) erhalten wurden, voneinander nicht sehr abweichen. Deswegen liegt es nahe, dass der Faktor, der weitestgehend die Ergebnisse beeinflusst, eher die Molekularstruktur des H<sub>2</sub>O ist, als die kollektive Verhaltensweise der Moleküle, welche den Unterschied zwischen dem superkritischen Wasser und dem Dampf ausmacht.

## Contents

<b>Acknowledgements</b> .....	<b>5</b>
<b>Abstract</b> .....	<b>6</b>
<b>Kurzfassung</b> .....	<b>11</b>
<b>Contents</b> .....	<b>16</b>
<b>List of Figures</b> .....	<b>18</b>
<b>List of Tables</b> .....	<b>22</b>
<b>Acronyms</b> .....	<b>23</b>
<b>1 Introduction</b> .....	<b>24</b>
1.1 Cross section: phenomenological definition.....	27
1.2 Motivation.....	27
1.3 State of the art.....	28
1.4 Goals of this work.....	38
<b>2 Elements of slow neutrons scattering</b> .....	<b>39</b>
2.1 Basics.....	39
2.1.1 Particle in centrally symmetric potential.....	39
2.1.2 Scattering in centrally symmetric potential.....	41
2.1.3 Scattering by a fixed nucleus with spin.....	45
2.1.4 The Born approximation.....	47
2.2 Literature.....	51
2.2.1 The formalism of Zemach and Glauber.....	51
2.2.2 Scattering by vibrators.....	54
2.2.3 Scattering by rotators.....	57
2.2.4 Scattering by molecules.....	58
2.2.5 Scattering of slow neutrons by liquid water.....	60
2.3 Modern methods.....	64
2.3.1 The Van Hove formalism.....	64
2.3.2 Phonons in solids.....	69
2.3.3 Gaussian approximation and the generalized frequency distribution.....	70
<b>3 Which thermal cross sections for supercritical water ?</b> .....	<b>76</b>
3.1 Molecular Dynamics simulations.....	76
3.2 Concrete recommendation.....	80

---

<b>4</b>	<b>Numerical tools used in the simulations .....</b>	<b>82</b>
4.1	Neutron transport through Monte Carlo (MCNP) .....	82
4.2	Depletion (ORIGEN2).....	83
4.3	Thermo hydraulics (STAFAS) .....	87
4.4	Burn-up simulation of 2D-geometries.....	89
4.4.1	Draft model of the process .....	89
4.4.2	Handling of the implementation's practical difficulties.....	90
4.5	Burn-up simulations of 3D geometries.....	94
4.5.1	Convergence criterion .....	95
4.5.2	BU software's upgrade and fitting for the coupling with STAFAS.....	97
<b>5</b>	<b>Results.....</b>	<b>102</b>
5.1	2D parametrical study of an HPLWR assembly's burn-up.....	102
5.1.1	Conclusions .....	113
5.2	3D burn-up simulation of an HPLWR assembly.....	114
5.2.1	Conclusions .....	123
5.3	2D burn-up simulation of the definitive geometry .....	124
5.3.1	Results .....	125
5.3.2	Conclusions .....	133
	<b>References.....</b>	<b>134</b>
	<b>Erklärung .....</b>	<b>136</b>

## List of Figures

Figure 1-1: HPLWR's flow path.....	30
Figure 1-2: Hexagonal arrangement by Dobashi et al. [1].....	31
Figure 1-3: Hexagonal arrangement by Bittermann [2] (2001). ....	31
Figure 1-4: Square arrangement by Bittermann [2] (2001).....	32
Figure 1-5: Hofmeister's geometry and the subdivision of the coolant section in 9 sub-channels. For reasons of symmetry, the simulation referred to only 1/8 <sup>th</sup> of the section.....	33
Figure 1-6: A schematic representation of the coolant flow according to the last proposed design. ....	34
Figure 1-7: Clusters' arrangement according to the last proposed flow path. ....	35
Figure 1-8: Picture of the definitive geometry obtained with MCNP's plotter. The light blue rings around the fuel rods represent the areas containing the wrapped wire. In the rings the wire's steel and the coolant have been homogenized.....	36
Figure 1-9: In this picture the honeycomb structure and the venting holes are visible. Note that the corners are made of massive steel.....	37
Figure 2-1: The total cross section of water in barns per hydrogen atom as a function of incident neutron energy. ....	63
Figure 2-2: The energy distribution of neutrons of incident energy 0.065 eV after scattering through 90 deg by water. ....	64
Figure 3-1: Radial distribution functions comparison. Experiment [17] (circles), Marti's MD simulation (continuous line). The top figures correspond to 573 °K and 0.72 g/cm <sup>3</sup> and the bottom figures correspond to 673 °K and 0.66 g/cm <sup>3</sup> .....	78
Figure 3-2: The top figures represent the movements associated to each normal mode of vibration of the Hydrogen atoms in the molecule of H <sub>2</sub> O. The bottom figures represent the elementary rotation movements. ....	79
Figure 4-1: Coolant's sub channel 3D volume element. ....	87
Figure 4-2: Heat transfer coefficient according to different correlations (P = 25 MPa, G = 1000 kg/m <sup>2</sup> s, q = 1E+06 W/m <sup>2</sup> ).....	88
Figure 4-3: As ORIGEN is a point-depletion code, it must be run once for each BU zone. ....	90
Figure 4-4: As shown in the example, the actual fuel temperature falls in any case between two available libraries temperatures. The same derived coefficients can be used to weigh the reaction rates tallied with the two libraries in order to estimate the reaction rate for the given fuel temperature. ....	91
Figure 4-5: The multi-group cross sections are calculated on the basis of a preliminary MCNP run carried out for fresh fuel, though the obtained cross sections are used throughout the burn-up simulation. ....	93
Figure 4-6: Complete flow-chart of the first version of the burn-up software.....	93
Figure 4-7: Power distribution profiles obtained through successive iterations for fresh fuel. The linear power is expressed in normalized units. ....	96

Figure 4-8: Flow-chart of the transport-thermo hydraulics convergence process.....	97
Figure 4-9: Flow-chart of the refined power distribution determination system.....	98
Figure 4-10: Flow-chart of the 3D burn-up simulation software.....	101
Figure 5-1: Bittermann's geometry rendered by the MCNP's plotter.....	103
Figure 5-2: Spectra detected by MCNP in fresh fuel using the three different models for hydrogen. Coolant temperature = 297 °C (bottom layer).....	105
Figure 5-3: Detail of Figure 5-2.....	105
Figure 5-4: Difference between the capture rates in the fuel foreseen by the liquid and free gas models, in the bottom layer. ....	106
Figure 5-5: Difference between the capture rates in the fuel foreseen by the vapour and free gas models, in the bottom layer. ....	106
Figure 5-6: Difference between the $K_{inf}$ 's foreseen in the bottom layer by the liquid and free gas models (blue line); by the vapour and free gas models (pink line).....	107
Figure 5-7: Difference between the fission rates foreseen by the liquid and free gas models in the bottom layer. ....	108
Figure 5-8: Difference between the capture rates foreseen by the liquid and free gas models in the bottom layer. ....	108
Figure 5-9: Difference between the major actinides' concentrations foreseen by the liquid and free gas models in the bottom layer. ....	109
Figure 5-10: Spectra in the fuel in the bottom layer tallied at 0, around 20 and 80 MWd/kg HM. The negative peaks at about 1E-06 MeV and 3E-06 MeV correspond to resonances in the capture cross sections. ....	110
Figure 5-11: Capture cross sections resonances that manifestly cause the growing negative peaks in the spectrum shown in Figure 5-10. Also the fission cross section of $U^{235}$ has small peaks in the same energy regions, but they are clearly irrelevant. ....	111
Figure 5-12: Spectra in the fresh fuel in the (~) bottom (black line) and top (blue line) layers.....	111
Figure 5-13: The blue line refers to the bottom layer. The pink one to the top layer. ....	112
Figure 5-14: Concentration of $Pu^{239}$ in the (~) bottom (blue line) and top (pink) layers. ....	112
Figure 5-15: Concentration of $Pu^{241}$ in the (~) bottom (blue line) and top (pink) layers. ....	113
Figure 5-16: Fuel assembly's linear power axial profile at the beginning and at the end of the 1 <sup>st</sup> burn-up step.....	115
Figure 5-17: Fuel assembly's linear power axial profile at the beginning and at the end of the 4 <sup>th</sup> burn-up step. ....	116
Figure 5-18: Fuel assembly's linear power axial profile at the beginning and at the end of the 7 <sup>th</sup> burn-up step. ....	116
Figure 5-19: Fuel assembly's linear power axial profile at the beginning and at the end of the 11 <sup>th</sup> burn-up step. ....	117
Figure 5-20: Fuel assembly's linear power axial profile at the beginning and at the end of the 18 <sup>th</sup> burn-up step. ....	117

Figure 5-21: Fuel assembly's linear power axial profile at the beginning and at the end of the 31 <sup>st</sup> burn-up step. ....	118
Figure 5-22: Fuel assembly's linear power axial profile at the beginning and at the end of the 44 <sup>th</sup> burn-up step. ....	118
Figure 5-23: Fuel assembly's linear power axial profile at the beginning and at the end of the 57 <sup>th</sup> burn-up step. ....	119
Figure 5-24: Fuel assembly's linear power axial profile at the beginning and at the end of the 70 <sup>th</sup> burn-up step. ....	119
Figure 5-25: Fuel assembly's linear power axial profile at the beginning and at the end of the 83 <sup>rd</sup> burn-up step. ....	120
Figure 5-26: Local burn-up in top and bottom layers as a function of the whole assembly's burn-up. ....	120
Figure 5-27: The average includes coolant, moderator in the box and in the gap. 554.5 days correspond to 26.50 MWd/kg HM. ....	121
Figure 5-28: The line in bold refers to the sub-channel where the temperature rose above the 620 °C limit. 35.5 days correspond to 1.70 MWd/kg HM. ....	122
Figure 5-29: The lines in bold refer to the sub-channels where the temperature rose above the 620 °C limit. 239.5 days correspond to 11.45 MWd/kg HM. ....	122
Figure 5-30: Fuel rods linear power in the middle layer of the evaporator. $S(\alpha, \beta)$ used: Liquid for moderator, Vapour for coolant. ....	125
Figure 5-31: Fuel rods linear power in the upper layer of the evaporator. $S(\alpha, \beta)$ used: Liquid for moderator, Vapour for coolant. ....	126
Figure 5-32: Fuel rods linear power in the upper layer of the 2nd superheater. $S(\alpha, \beta)$ used: Liquid for moderator, Vapour for coolant. ....	126
Figure 5-33: Spectra in the fuel at 0 MWd/kg HM. The flux density (per unit of lethargy) is given in normalized unit. ....	127
Figure 5-34: Spectra in the fuel at about 40 MWd/kg HM. The flux density (per unit of lethargy) is given in normalized unit. ....	127
Figure 5-35: Spectra in the fuel at 80 MWd/kg HM. The flux density (per unit of lethargy) is given in normalized unit. ....	128
Figure 5-36: Difference of the most important actinides concentrations between the well moderated rod 6 and a second, arbitrarily chosen rod. For high burn-up, as the power in rod 6 decreases and the consumption of $U^{235}$ as well, the difference tends to ease off. ....	129
Figure 5-37: The negligible differences between two less moderated rods reveal that what happens in rod 6 is not common among the other rods. ....	129
Figure 5-38: Capture rate in $U^{238}$ in the two best moderated rods (6 and 7) and in one of the other rods (in this case rod 3). ....	130
Figure 5-39: Fission rate of $Pu^{239}$ in the two best moderated rods (6 and 7) and in one of the other rods (in this case rod 3). ....	131
Figure 5-40: Fission rate of $Pu^{241}$ in the two best moderated rods (6 and 7) and in one of the other rods (in this case rod 3). ....	131
Figure 5-41: Difference between the concentration of the most important actinides in the best moderated rod and in one of the other rods (in this case rod 3). ....	132

Figure 5-42: Fuel rods linear power in the bottom layer of the evaporator.  $S(\alpha, \beta)$  used: Liquid for moderator, Liquid for coolant. Note that the power excursion in rod 7 is considerably smaller than in the other considered cases. 133

## List of Tables

Table 1-1: De Broglie's wavelength associated to various neutron energies. ....	27
Table 3-1: Marti's simulated thermodynamic states. According to Marti the implemented potentials should imply a critical point close to state 4.....	77
Table 3-2: Intramolecular oscillator frequencies of H bound in H <sub>2</sub> O in meV, according to Bernnat et al. [15]. Frequencies 1 and 3 refer to the stretching modes and are treated as one. Frequency 2 refers to bending.....	79
Table 3-3: The frequencies in the first row are Bernnat's frequencies for liquid. The frequencies in the following rows have been obtained adding the frequency displacements registered by Marti (with respect to Marti's values at room temperature) to the first row's frequencies. The uncertainties of the MD simulation values are about of 1% of each value.....	80
Table 4-1: Actinides for which the reaction rates were tallied at every burn-up step. 99	
Table 4-2: Fission products for which the reaction rates were tallied at every burn-up step.....	100
Table 5-1: Parameter combinations for the 2D burn-up calculations. ....	103
Table 5-2: Time steps applied in the 2D parametric simulations of Bittermann's geometry.....	104
Table 5-3: "L" = S( $\alpha,\beta$ ) for liquid, "V" = S( $\alpha,\beta$ ) for vapour, "FG" = Free Gas approximation. "cold wall" = steel sheets wet by the moderator, "hot wall" = steel sheets wet by the coolant. Note that each of the configurations "Evap. Middle" and "2 <sup>nd</sup> Superheater Top" have been considered twice, using different S( $\alpha,\beta$ ) for the coolant. ....	124

## Acronyms

2D	two-dimensional
3D	three-dimensional
BU	Burn-up
BWR	Boiling Water Reactor
HPLWR	High Performance Light Water Reactor
HPLWR2	High Performance Light Water Reactor Phase 2
IKE	Institut für Kernenergetik und Energiesysteme (University of Stuttgart)
IKET	Institut für Kern- und Energietechnik (Karlsruher Institut für Technologie)
MCNP	Monte Carlo N-Particle Transport Code System
MD	Molecular dynamics
MWd/kg HM	Megawatt day per kilogram of Heavy Metal
STAFAS	Sub-channel Thermal-hydraulic Analysis in Fuel Assemblies under Supercritical conditions
SW	Supercritical Water

# 1 Introduction

The system of one particle subject to a conservative force field derived from a potential  $U$  can be described by the canonical system:

$$\begin{cases} \dot{p}_k = -\frac{\partial H}{\partial q_k} \\ \dot{q}_k = \frac{\partial H}{\partial p_k} \end{cases} \quad 1-1$$

( $k = 1, 2, 3$ ) where  $H$  is the Hamiltonian function.

In classical physics, a system is characterized at every time  $t$  by a state.

In the case of a system made of a single particle the state is defined by the three coordinates  $q_k$  and the corresponding kinetic moments  $p_k \equiv \frac{\partial L}{\partial \dot{q}_k}$ , where  $L$  is the Lagrange function.

It is assumed that the system is in every moment characterized by certain well-defined values of  $q_k$  and  $p_k$ , which represent its position in the Gibbs phase-space independently from the fact that a measurement of them is taking place or not.

In quantum physics the vision is profoundly different.

From a practical point of view, particles are only interaction vehicles between different parts of matter.

There exist only indirect evidences of the particles, that is, the observable (and therefore measurable) events that they bring about in experiments, like e.g. the traces that they leave in a detector.

The results of these experiments can not be forecast deterministically.

The initial state of the system, that is, the preparation of the experiment is represented by an element  $\psi$  from a Hilbert space which, in our case, is chosen to be  $L^2(R^3)$ .

According to the theory, the particle doesn't have a well defined position in space, but experiments executed to detect its position will return values of  $x$  according to the probability distribution  $\langle \psi(x) | \psi(x) \rangle \equiv |\psi(x)|^2$ . Therefore, the mean value will be:

$$\bar{x} \equiv \int x |\psi(x)|^2 dx \equiv \langle \psi(x) | x | \psi(x) \rangle \quad 1-2$$

As far as the linear momentum  $p_x$  is concerned, its probability distribution is given by

$$\left\langle \frac{1}{\sqrt{\hbar}} \mathcal{F}(\psi) \left( \frac{p_x}{\hbar} \right) \middle| \frac{1}{\sqrt{\hbar}} \mathcal{F}(\psi) \left( \frac{p_x}{\hbar} \right) \right\rangle \equiv \left| \frac{1}{\hbar} \tilde{\psi} \left( \frac{p_x}{\hbar} \right) \right|^2, \text{ where with the operator } \mathcal{F} \text{ we indicate}$$

the Fourier transform<sup>1</sup>, so that its mean value will be:

$$\bar{p}_x \equiv \int p_x \left| \frac{1}{\sqrt{\hbar}} \tilde{\psi} \left( \frac{p_x}{\hbar} \right) \right|^2 dp_x \equiv \left\langle \frac{1}{\sqrt{\hbar}} \tilde{\psi} \left( \frac{p_x}{\hbar} \right) \middle| p_x \middle| \frac{1}{\sqrt{\hbar}} \tilde{\psi} \left( \frac{p_x}{\hbar} \right) \right\rangle \quad 1-3$$

More in general, for every physical quantity  $A$  it is possible to introduce a self-adjoint operator  $\hat{A}$  such that the statistical mean value assumed by the physical quantity  $A$  is

$$\langle A \rangle = \langle \psi | \hat{A} | \psi \rangle \quad 1-4$$

Consistently with what said before, the operators associated to the physical quantities “position” and “linear momentum” result to be (see 1-2 and 1-3):

$$\begin{aligned} x_k &\rightarrow \hat{x}_k \equiv x_k \\ p_k &\rightarrow \hat{p}_k \equiv \mathcal{F}^{-1} \hat{x}_k \mathcal{F} \equiv -i\hbar \frac{\partial}{\partial x_k} \end{aligned} \quad 1-5$$

The temporal evolution of the state  $\psi_t$  is a rotation of the initial state given by the Schrödinger equation:

$$i\hbar \frac{d\psi_t}{dt} = \hat{H} \psi_t \quad 1-6$$

where  $\hat{H}$  is a self-adjoint operator that is made up considering the classical Hamiltonian function associated to the system and symbolically replacing  $x_k$  and  $p_k$  with the operators introduced in 1-5.

Correspondingly, it can be shown that<sup>2</sup>

$$\psi(x, t) = e^{-\frac{i\hat{H}t}{\hbar}} \psi(x, 0) \quad 1-7$$

<sup>1</sup> Given a function  $\psi(x)$ , we assume the following definition of Fourier transform:

$$\tilde{\psi}(k) \equiv \mathcal{F}(\psi)(k) \equiv \frac{1}{\sqrt{2\pi}} \int \psi(x) e^{-ikx} dx \quad \text{so that, correspondingly:}$$

$$\psi(x) = \mathcal{F}^{-1}(\tilde{\psi})(x) \equiv \frac{1}{\sqrt{2\pi}} \int \tilde{\psi}(k) e^{ikx} dk$$

<sup>2</sup>  $e^{\hat{K}} \equiv \sum_{n=0}^{\infty} \frac{\hat{K}^n}{n!} = \hat{1} + \hat{K} + \frac{\hat{K}^2}{2!} + \frac{\hat{K}^3}{3!} + \dots$

The temporal evolution of a physical quantity's mean value will be given by (reminding that  $\hat{H} = \hat{H}^\dagger$ ):

$$\begin{aligned} \frac{d\langle A \rangle}{dt} &= \frac{d}{dt} \langle \psi | \hat{A} | \psi \rangle = \left\langle \frac{d\psi}{dt} | \hat{A} | \psi \right\rangle + \langle \psi | \hat{A} | \frac{d\psi}{dt} \rangle = \left\langle \frac{1}{i\hbar} \hat{H} \psi | \hat{A} | \psi \right\rangle + \langle \psi | \hat{A} | \frac{1}{i\hbar} \hat{H} \psi \rangle = \\ &= \frac{1}{i\hbar} \langle \psi | [\hat{A}, \hat{H}] | \psi \rangle \end{aligned} \quad 1-8$$

Let's consider the system of one free particle ( $U=0$ ).

The Schrödinger equation will take on the form:

$$i\hbar \frac{d\psi_t}{dt} = -\frac{\hbar^2}{2m} \nabla^2 \psi_t \quad 1-9$$

whose most general solution is:

$$\psi(\mathbf{x}, t) = \frac{1}{(2\pi\hbar)^{3/2}} \int d^3 p e^{\frac{i}{\hbar}(\mathbf{p}\cdot\mathbf{x} - \frac{p^2}{2m}t)} c(\mathbf{p}) \equiv \frac{1}{(2\pi\hbar)^{3/2}} \int d^3 p e^{\frac{i}{\hbar}\mathbf{p}\cdot\mathbf{x}} c(\mathbf{p}, t) \quad 1-10$$

1-10 is a wave packet, that is, the superposition of plane waves like the following one:

$$u_{\mathbf{p}}(\mathbf{x}) = e^{\frac{i}{\hbar}(\mathbf{p}\cdot\mathbf{x} - \frac{p^2}{2m}t)} \quad 1-11$$

In accordance with what stated above, the particle, in general, doesn't have a well-defined value of linear moment. The only thing that can be said is that measures of linear moment  $\mathbf{p}$  will result in values varying according to the probability distribution:

$$|c(\mathbf{p}, t)|^2 \equiv \left| c(\mathbf{p}) e^{\frac{i}{\hbar}(\mathbf{p}\cdot\mathbf{x} - \frac{p^2}{2m}t)} \right|^2 = \left| \frac{1}{\hbar^{3/2}} \tilde{\psi}\left(\frac{\mathbf{p}}{\hbar}, t\right) \right|^2 = \left| \frac{1}{(2\pi\hbar)^{3/2}} \int d^3 x e^{-\frac{i}{\hbar}\mathbf{p}\cdot\mathbf{x}} \psi(\mathbf{x}, t) \right|^2 \quad 1-12$$

However, if the over-mentioned probability distribution is sharply peaked in correspondence of a certain  $\mathbf{p}_0$ , then the variance of the momentum measurements will be relatively low.

The group velocity will be given by  $\mathbf{v}_g = \frac{\mathbf{p}_0}{m}$ , while  $\lambda = \frac{h}{|\mathbf{p}_0|}$  is the so-called De Broglie

wavelength associated with the wave packet.

Table 1-1 shows the De Broglie wavelengths corresponding to various neutron's energies.

Table 1-1: De Broglie's wavelength associated to various neutron energies.

NEUTRON'S ENERGY	eV	De Broglie wavelength [nm]
Thermal	0,025	1,81E-01
Epithermal	1	2,86E-02
Slow	1,E+03	9,04E-04
Fast	1,00E+05	9,04E-05
Fast	1,0E+07	9,04E-06

Reminding that the interatomic distances in crystals and molecules are of the order of 0,1-1 nm, it's clear that under 1 eV the neutron doesn't interact any more with the single atoms, but with the multi-atomic structure of matter.

From a practical point of view, this means that one can simulate the slowing down of neutrons until a few eV using the classical theory of scattering. But as the neutron's  $\psi$  begins to interact with more than one identical atom at a time, the scattering must be simulated according to quantum physics.

## 1.1 Cross section: phenomenological definition

As already driven at in the previous paragraph, in quantum physics it is only possible to determine the probability that an experiment yields a certain outcome.

Scattering is a very important class of experiments, which consist in preparing a beam of particles having momentum  $\mathbf{p}_0$  and addressing them to a target, consisting of a portion of matter having well-known macroscopic properties. As a consequence of the interaction, the beam is diffused. The rate of particles scattered in a certain small solid angle  $d\Omega(\hat{u})$  centred upon the direction  $\hat{u}$  is measured.

If the target is thin enough to make multiple scattering negligible, under quite general conditions the following phenomenological law applies:

$$dN(\hat{u}) = d\Omega(\hat{u})\sigma(E, \vartheta_{\vec{p}_0, \vec{u}})n_{in}N \quad 1-13$$

where  $dN(\hat{u})$  is the rate of particles outgoing in  $d\Omega(\hat{u})$ ;  $\sigma(E, \vartheta_{\vec{p}_0, \vec{u}})$  is a quantity typical of the interaction of the ingoing particle with one of the target's particles, which is called differential cross-section;  $n_{in}$  is the rate of incoming particles;  $N$  is the total number of target's particles exposed to the incoming beam.

## 1.2 Motivation

The fundamental circumstance that led to this work is the IKE's participation in the HPLWR2 project.

HPLWR2 is a program of European cooperation focused to assess the critical scientific issues and the technical feasibility of a High Performance Light Water Reactor (HPLWR) operating under supercritical pressure.

The project started on September 1<sup>st</sup> 2006 and has its roots in the fact that the HPLWR concept pursues the goals fixed by the Generation IV International Forum for the next generation of nuclear energy systems. These are:

- Sustainability
- Safety & Reliability
- Economics
- Proliferation Resistance & Physical Protection

One of the main reasons why the HPLWR proposal was selected (together with other 5 concepts), is the good perspective of feasibility, because it can be seen as an evolution of the BWR reactor: in a HPLWR, effectively, the coolant leaving the reactor directly heads to the turbine, without steam generators. But, more than this, as the water's pressure is raised to a supercritical pressure of 25 MPa, no phase transition takes place in the vessel, and therefore no recirculation pumps, steam separators or dryers are needed.

The HPLWR would also build on solid experience from the conventional power plant industry: major nuclear vendors are also manufacturers of supercritical turbines and/or boilers.

The connection between the IKE at the University of Stuttgart and the IKET in the FZK, friendly but also competitive at the same time, has also been instrumental to the start and direction of this work, because it spurred our group to find a role for the IKE in the HPLWR2 consortium that could take advantage of the competences and the leading-edge progress of the IKET without being subordinate to it.

If one considers the PhD theses related to the HPLWR2 project published in the last years at the IKET, it's not difficult to find complementary fields of research where the IKE can be competitive. In particular: burn-up simulations and thermal cross sections.

### **1.3 State of the art**

As mentioned before, this work has been accomplished with the constant support of the IKET, which in these years has always been leading-edge in the development of the thermo hydraulics of the fuel assemblies and of the whole of the reactor as well.

In the last years the fuel bundle's design has undergone a number of modifications and improvements, and as this work has been accomplished over the span of about 6 years,

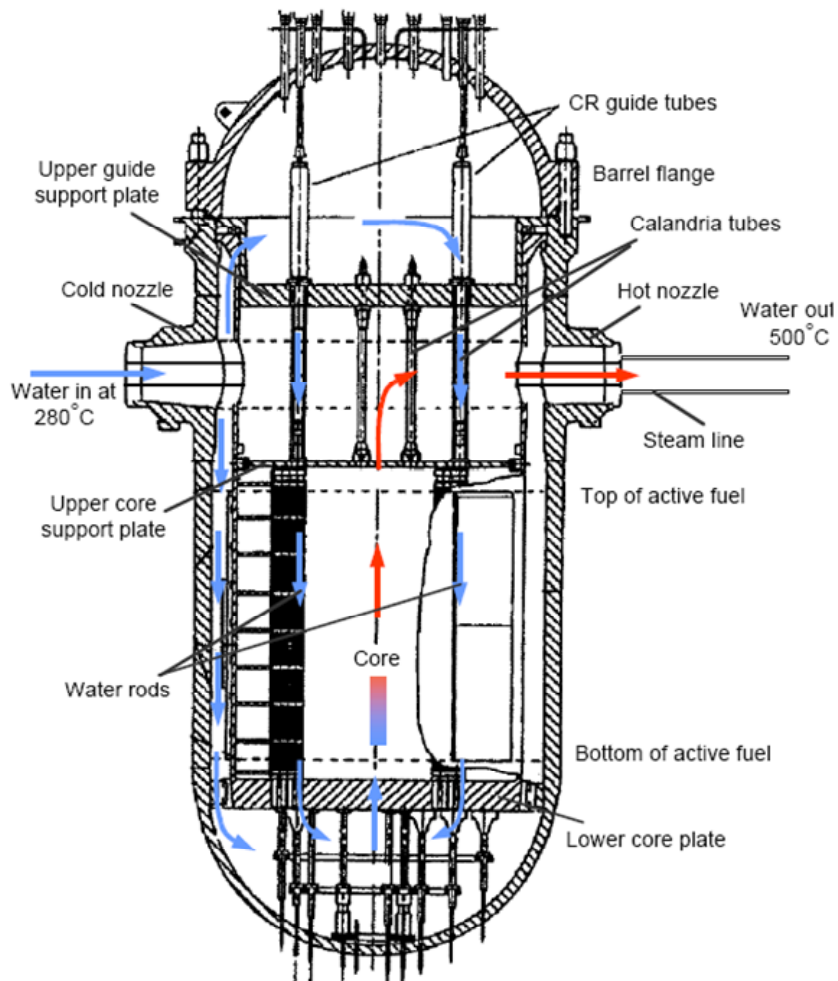
the burn-up simulations were carried out at each time with reference to the respective current state-of-the-art geometry, input from the IKET or other HPLWR2's partners.

Anyway, some basic features were clear since the beginning.

The basic concept of the HPLWR is the cooling by means of water at a supercritical pressure of around 25 MPa, having inlet and outlet temperatures respectively of about 300 °C and about 500 °C.

The high coolant's exit temperature would contribute to high plant efficiency, which is expected to attain about 45 %.

On the other hand, the large temperature increase would imply a water's strong axial density variation. In order to achieve a sufficient high moderation ratio and to flatten the axial power profile, it was proposed since the beginning to introduce water rods, through which part of the feeding water should flow downwards, whereas the rest should descend the downcomer, merge with the water coming out of the moderator channels and then flow upwards around the fuel rods, acting as coolant (Figure 1-1).



Source: J. Buongiorno, INEEL

Figure 1-1: HPLWR's flow path.

## 2004-2005

In 2004 we started with a first set of 2D burn-up simulations. Among the geometries available at that time (see Figure 1-2, Figure 1-3 and Figure 1-4) we chose Bitterman's squared arrangement.

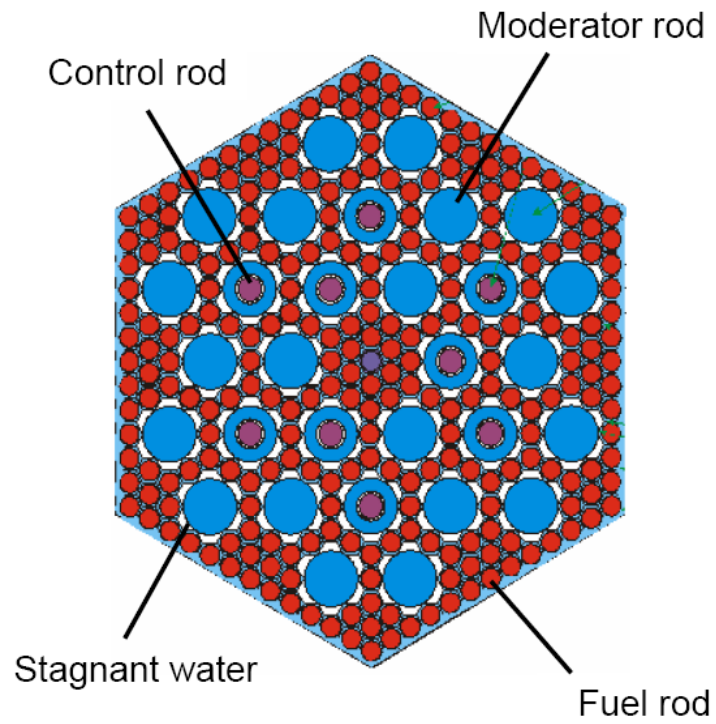


Figure 1-2: Hexagonal arrangement by Dobashi et al. [1]

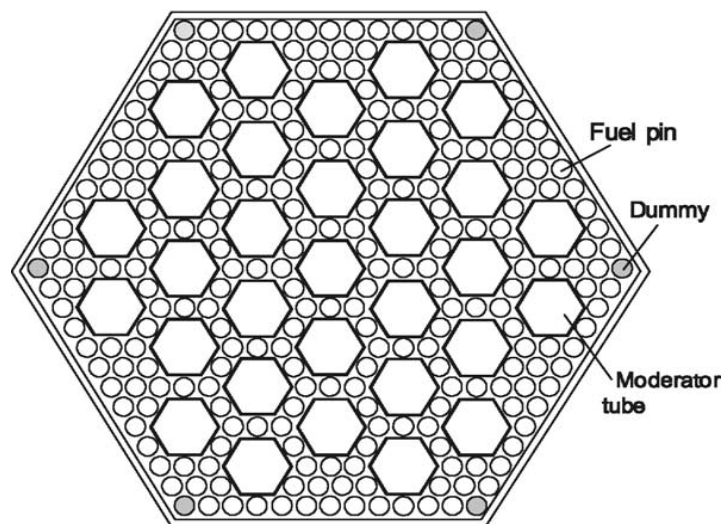


Figure 1-3: Hexagonal arrangement by Bittermann [2] (2001).

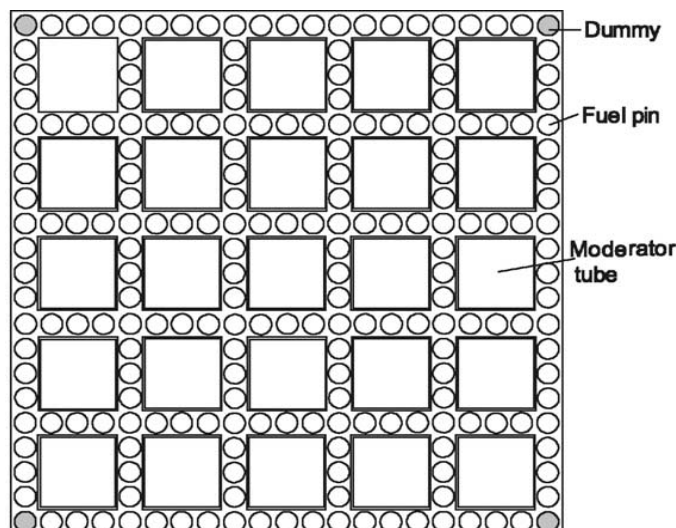


Figure 1-4: Square arrangement by Bittermann [2] (2001).

The reason of this choice lies in the availability of literature regarding the thermal-hydraulic configuration of this design at that time.

Cheng et al. [3] published in 2003 the results of an analysis of the thermal-hydraulic behaviour of this assembly using a newly conceived thermal-hydraulics software specifically conceived to simulate fuel bundles under supercritical conditions (STAFAS, Sub-channel Thermal-hydraulic Analysis in Fuel Assemblies under Supercritical conditions).

The new package could keep in count the downward-flowing moderator and implemented a more precise approach than conventional software offers for computing the thermal-physical properties, in order to exactly represent the large variations affecting the parameters describing the thermodynamic state of the supercritical fluid.

### 2005-2007

In 2006 a new, improved version of STAFAS was issued, featuring a standardised input/output interface that made it possible to input data and get the output from the software in form of tabular text files, fit to be automatically handled.

The updated software referred to a new fuel assembly geometry proposed by J. Hofmeister from FZK [4], depicted in Figure 1-5.

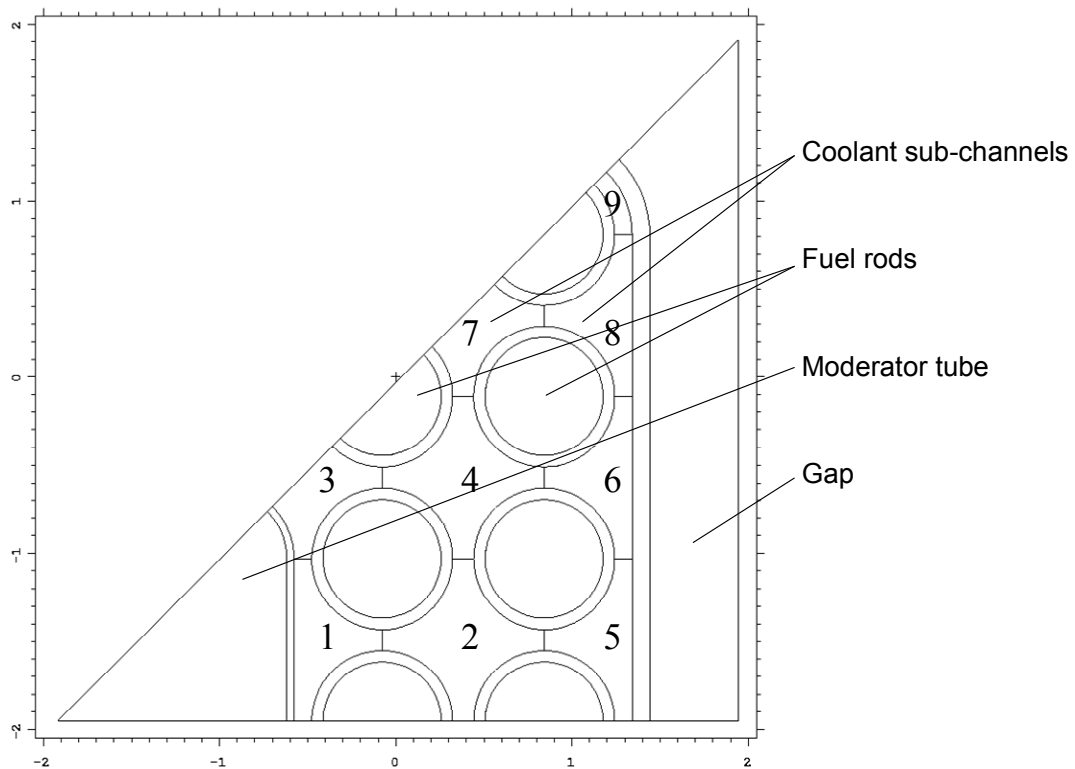


Figure 1-5: Hofmeister's geometry and the subdivision of the coolant section in 9 sub-channels. For reasons of symmetry, the simulation referred to only 1/8<sup>th</sup> of the section.

The new model had been conceived on the basis of thermal-mechanical evaluations and broad neutronics considerations.

The main guidelines had been:

- Minimising the structural material in core
- Optimising the structure-to-fuel and moderator-to-fuel ratios
- Simplifying the sub-channel analysis

### 2008-2009

The 3D simulations carried out during the two previous years put in evidence serious problems of overheating of the cladding at the top of the fuel element. This problem had deep roots and therefore could not be surmounted only trimming some of Hofmeister's geometry parameters.

Effectively, the problem lied in the purpose of combining high coolant's outlet temperature and high power density.

The latter requires, in turn, high fuel temperature, in order to have a respectable heat flux though the hot coolant: the cladding, which is between fuel and coolant, is in this case the weak link in the chain.

As the high thermo dynamical efficiency constitutes the very essential reason at the base of the interest towards this reactor concept, a new flow path was proposed, that lays down the high power density for the benefit of lower cladding temperatures.

The idea is to have high heat flux where the coolant's temperature is still relatively low, and low heat flux where the coolant's temperature is high.

The implementation of this consists in a three pass core in which the coolant is heated up in three distinct phases as shown in Figure 1-6.

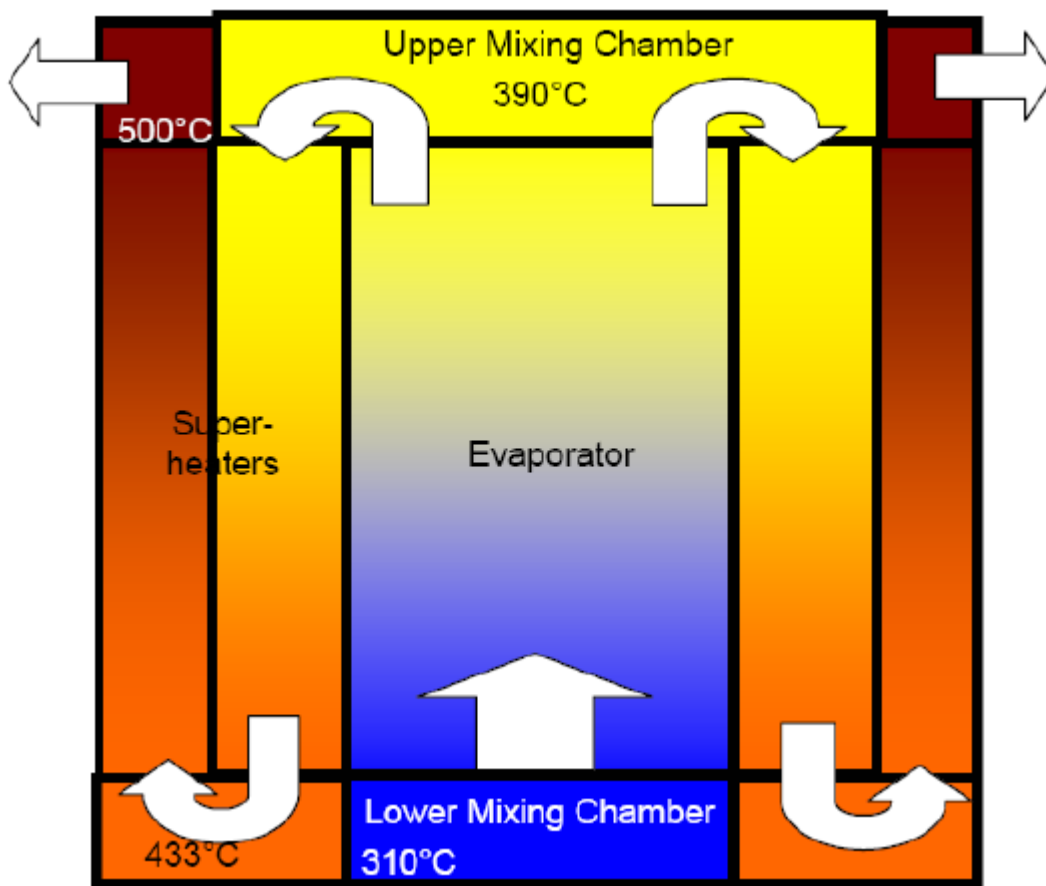


Figure 1-6: A schematic representation of the coolant flow according to the last proposed design.

The new flow path has in common with the old one the fact that the water coming in the vessel from the cold leg flows downwards through the moderator boxes and the gaps acting as moderator, before being mixed with the downcomer water and enter the first pass with a temperature of 310 °C. As the moderator is heated up by the coolant and its

temperature remains under the pseudo critical point, this circumstance is not so detrimental, and the moderator pass can be seen as an “economizer”.

In the first coolant pass, the water flows therefore upwards around the fuel rods of 52 clusters, reaching a temperature of 390 °C at the top. As the temperature rises above the pseudo critical point, this pass is called “evaporator”.

After an adequate mixing, the coolant pursues its heating up flowing downwards through 52 clusters surrounding the evaporator (“first super heater”), reaching a temperature of 433 °C at the bottom.

A third mixing precedes the third, upwards pass through the external 52 clusters (“second super heater”), which brings the water to 500 °C.

Figure 1-7 shows how the clusters are concentrically distributed, with the evaporator in the middle and the first and the second super heaters externally, in sequence.

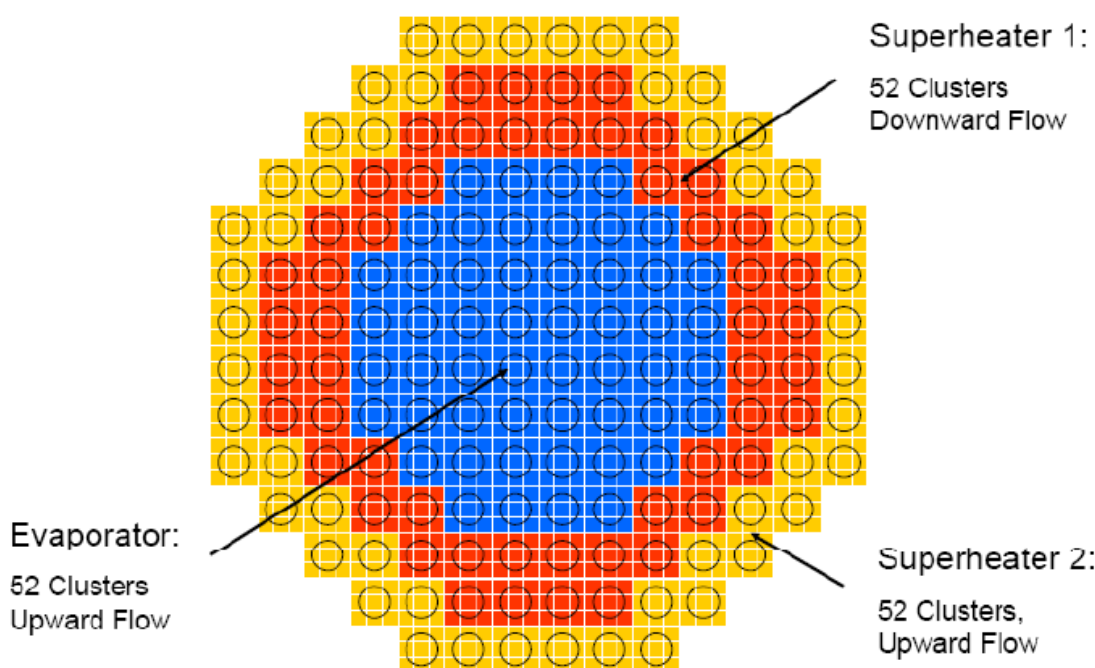


Figure 1-7: Clusters' arrangement according to the last proposed flow path.

This configuration implements the original idea of low heat flux where the temperature is high: the thermal power densities in the evaporator, first and second super heater should be respectively 84.9, 47.7 and 27.5 MW/m<sup>3</sup>.

Remaining loyal to its basic features, some improvements have been introduced in Hofmeister's design (Figure 1-8).

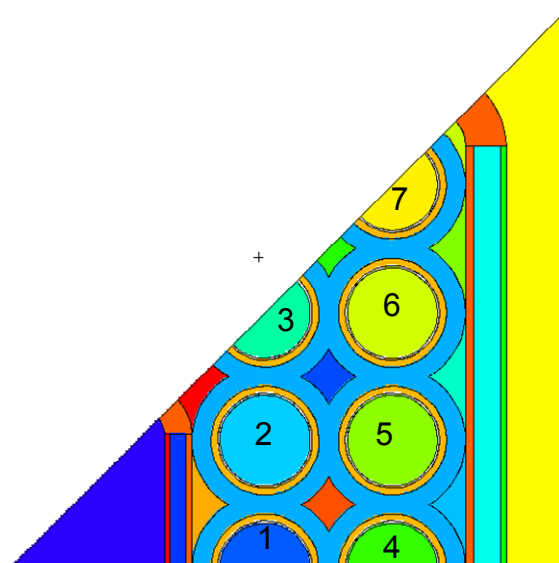


Figure 1-8: Picture of the definitive geometry obtained with MCNP's plotter. The light blue rings around the fuel rods represent the areas containing the wrapped wire. In the rings the wire's steel and the coolant have been homogenized.

The pitch-to-diameter ratio has been increased from 1.15 to 1.18 to limit the pressure drop of the coolant.

The steel massive walls that formed the sidewalls and the moderator box walls were replaced by a steel honeycomb structure filled with bulk alumina fibre and contained as in a sandwich by two external steel sheets.

The alumina fibre assures a better heat insulation between coolant and moderator.

As the steel fraction in the honeycomb structure is only 7 %, the quantity of steel in the sidewalls is reduced, improving the neutronics.

As the honeycomb has a relatively low resistance to compression, the steel sheets wet by the moderator (of the moderator box and of the gap) are perforated with punched venting holes of 0.5 mm diameter for each cell of the honeycomb, so that during operation the alumina fibre, which has a porosity of about 35 %, will be soaked in water.

A stainless steel wire wrapped around each fuel rod has been introduced as spacer and to help mix the coolant well.

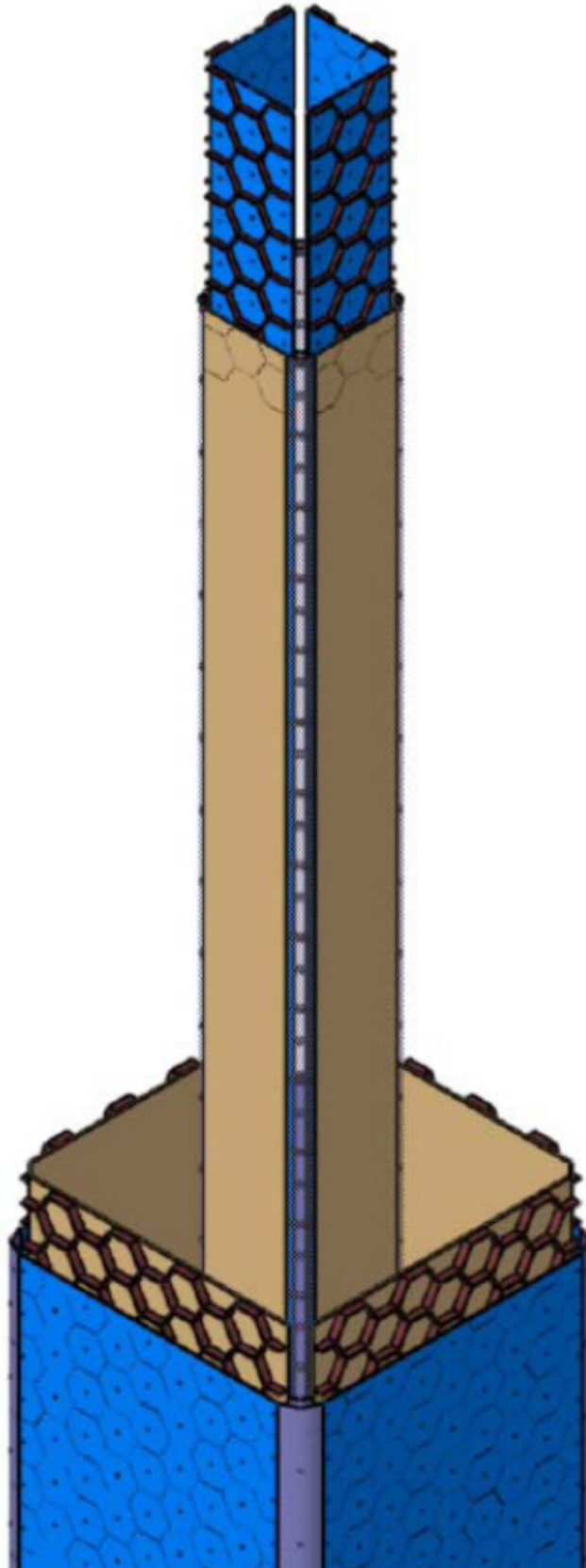


Figure 1-9: In this picture the honeycomb structure and the venting holes are visible. Note that the corners are made of massive steel.

## 1.4 Goals of this work

### Cross sections

In the recent past, a considerable expertise in the field of thermal neutrons scattering dynamics has been achieved at IKE Stuttgart.

In particular, for light water in its states solid, liquid and vapour realistic models have been derived to describe the neutron scattering dynamics as a function of energy transfer, impulse change and moderator temperature.

Thermal neutron cross section sets were generated for a large temperature grid and stored in ENDF-6 format as Scattering Law Data  $S(\alpha, \beta, T)$ .

On the other hand, neutrons' scattering dynamics in supercritical water is not yet well known. Due to the absence of specific test facilities, it is hard to carry out even theoretical works, in that even the progress of theoretical works would need some experimental feedback.

The unavailability of thermal cross section sets specifically prepared for supercritical water leaves no alternatives to carrying out transport simulations using inadequate scattering models, affecting the credibility of the results.

With these premises, the following goals were set down:

1. Assessing the variability of the results in dependence of the physical model adopted for water, as function of the burn-up.

The sense of this is to obtain an index of the error affecting the results of transport and more in general of burn-up simulations carried out with inadequate thermal cross section sets for the moderator and the coolant.

2. Suggesting a compromise solution in order to come to terms with the problem.

### Burn-up

The availability of a software like STAFAS has spurred on the IKET at the FZK to undertake some more ambitious projects, in particular Waata's [5] effort to calculate the power distribution and any other associated parameter of the whole three dimensional fuel element.

The conclusions drawn from this art of works were limited to the fresh fuel.

On this basis, the following goal was set down:

3. Putting Waata's conclusions regarding power, cladding temperature etc. distributions and reactivity to the test of burn-up.

## 2 Elements of slow neutrons scattering

### 2.1 Basics

In reference to 1.1, in order to infer  $\sigma(E, \theta_{\vec{p}_0, \vec{u}})$  from the theory, we consider the idealized case of the system of a particle scattering in a centrally symmetric field, having centre in the origin of the reference frame and potential energy  $U(r)$ .

The typical circumstance of scattering problems is the existence of an asymptotic region ( $|\mathbf{x}|$  large enough) where  $U(r)$  is negligible. Mathematically speaking, it is assumed that  $U(r)$  falls off faster than  $1/r$ . This is a common circumstance in nuclear physics, where the interactions among nuclei, protons and neutrons have a very short range. The case of Coulombian interaction, in principle, should be treated apart.

#### 2.1.1 Particle in centrally symmetric potential

Given the central symmetry of the Hamiltonian  $\hat{H} = \frac{\hat{p}^2}{2m} + U(r)$ ,  $\hat{H}$  commutes with  $\hat{L}^2$  and  $\hat{L}_z$ , therefore one can look for the eigenfunctions of  $\hat{H}$  in the eigenspaces  $S_{lm}$  common to the above mentioned operators, having eigenvalues respectively  $\hbar^2 l(l+1)$  and  $\hbar m$  ( $-l \leq m \leq l$ ). They have the following structure:

$$u_{plm}(r, \theta, \varphi) = \frac{y_{pl}(r)}{r} Y_{lm}(\theta, \varphi) \quad 2-1$$

where  $y_{pl}(r)$  are the solutions of the radial equation:

$$-\frac{\hbar^2}{2m} \frac{d^2 y_{pl}(r)}{dr^2} + \left[ U(r) + \frac{\hbar^2 l(l+1)}{2mr^2} \right] y_{pl}(r) = \frac{p^2}{2m} y_{pl}(r) \quad 2-2$$

fulfilling the condition:

$$y_{pl}(0) = 0 \quad 2-3$$

so that  $u_{plm}(r, \theta, \varphi)$  can be limited in  $r = 0$ .

For  $r \rightarrow \infty$  eq. 2-2 reduces to:

$$-\frac{\hbar^2}{2m} \frac{d^2 \tilde{y}_{pl}(r)}{dr^2} = \frac{p^2}{2m} \tilde{y}_{pl}(r) \quad 2-4$$

whose solution  $\tilde{y}_{pl}(r)$ , representing the asymptotic behaviour of  $y_{pl}(r)$ , has the form:

$$\tilde{y}_{pl}(r) = Ae^{\frac{ipr}{\hbar}} + Be^{-\frac{ipr}{\hbar}} \quad 2-5$$

Through quite an intricate treatment it can be shown that:

$$A_{pl} = \frac{1}{\sqrt{2\pi\hbar}} e^{i\alpha_{1l}(p)}, B_{pl} = \frac{1}{\sqrt{2\pi\hbar}} e^{i\alpha_{2l}(p)} \quad 2-6$$

and replacing  $A_{pl}$  and  $B_{pl}$  in 2-5 one obtains:

$$\begin{aligned} y_{pl}(r) &\xrightarrow{r \rightarrow \infty} \frac{1}{\sqrt{2\pi\hbar}} \left[ e^{i\left(\frac{pr}{\hbar} + \alpha_{1l}(p)\right)} + e^{-i\left(\frac{pr}{\hbar} - \alpha_{2l}(p)\right)} \right] = \\ &= \frac{1}{\sqrt{2\pi\hbar}} e^{\frac{i}{2}(\alpha_{1l}(p) + \alpha_{2l}(p))} \left[ e^{i\left(\frac{pr}{\hbar} + \frac{1}{2}(\alpha_{1l}(p) - \alpha_{2l}(p))\right)} + e^{-i\left(\frac{pr}{\hbar} + \frac{1}{2}(\alpha_{1l}(p) - \alpha_{2l}(p))\right)} \right] \end{aligned} \quad 2-7$$

The phase factor  $e^{\frac{i}{2}(\alpha_{1l}(p) + \alpha_{2l}(p))}$  has no physical relevance and therefore can be neglected. One obtains then:

$$y_{pl}(r) \xrightarrow{r \rightarrow \infty} \sqrt{\frac{2}{\pi\hbar}} \cos\left(\frac{pr}{\hbar} + \alpha_l(p)\right) \quad 2-8$$

where

$$\alpha_l(p) \equiv \frac{1}{2}(\alpha_{1l}(p) - \alpha_{2l}(p)) \quad 2-9$$

### Free particle

In the case that  $U(r) = 0$  then it can be shown that the solution of 2-2 is

$$\Rightarrow y^{(0)}_{lp}(r) = \sqrt{\frac{2}{\pi\hbar}} \frac{rp}{\hbar} j_l\left(\frac{rp}{\hbar}\right) \quad 2-10$$

so that

$$\Rightarrow u_{plm}^{(0)}(r, \theta, \varphi) = \frac{y^{(0)}_{lp}(r)}{r} Y_{lm}(\theta, \varphi) = \sqrt{\frac{2}{\pi\hbar}} \frac{p}{\hbar} j_l\left(\frac{rp}{\hbar}\right) Y_{lm}(\theta, \varphi) \quad 2-11$$

where  $j_l(p)$  are the Bessel's spherical functions. The index (0) reminds that we are referring to the free particle.

Confronting 2-10 with 2-8 one finds that for the free particle:

$$\alpha_l(p) = -\frac{\pi}{2}(l+1) \quad 2-12$$

Consider the Hamiltonian for the free particle  $\hat{H} = \frac{\hat{p}^2}{2m}$ . Alternatively to the set of commuting operators  $|\hat{\mathbf{p}}\rangle, \hat{L}^2, \hat{L}_z$ , one can consider the set of commuting operators  $\hat{p}_x, \hat{p}_y, \hat{p}_z$ . Correspondingly, there exist the following two complete sets of orthonormal eigenfunctions:

$$u_{plm}^{(0)}(\mathbf{x}) = \sqrt{\frac{2}{\pi\hbar}} \frac{p}{\hbar} j_l\left(\frac{rp}{\hbar}\right) Y_{lm}(\theta, \varphi) \quad 2-13$$

and

$$u_{\mathbf{p}}^{(0)} = \frac{1}{(2\pi\hbar)^{3/2}} e^{i\frac{\mathbf{p}\cdot\mathbf{x}}{\hbar}} \quad 2-14$$

As both orthonormal sets are a basis, it must be possible to express each vector belonging to one set as a linear combination of the vectors belonging to the other one according to the scheme:

$$u_{\mathbf{p}}^{(0)}(\vec{x}) = \sum_{l,m} c_{lm}^{(0)}(\mathbf{p}) u_{plm}^{(0)} \quad 2-15$$

Effectively it can be shown that:

$$\frac{1}{(2\pi\hbar)^{3/2}} e^{i\frac{\mathbf{p}\cdot\mathbf{x}}{\hbar}} = \sum_{l=0}^{\infty} \sum_{m=-l}^{+l} \frac{i^l}{p} Y_{lm}^*(\alpha, \beta) u_{plm}^{(0)}(r, \theta, \varphi) \quad 2-16$$

### 2.1.2 Scattering in centrally symmetric potential

It was shown that the eigenfunctions  $u_{plm}$  belonging to the orthonormal basis 2-13 have a radial part  $\frac{y_{pl}^{(0)}(r)}{r}$  (see 2-11), where the  $y_{pl}$  have the asymptotic form:

$$y_{pl}(r) \xrightarrow{r \rightarrow \infty} \sqrt{\frac{2}{\pi\hbar}} \cos\left(\frac{pr}{\hbar} + \alpha_l(p)\right) \quad 2-17$$

with

$$\alpha_l(p) = -\frac{\pi}{2}(l+1) \quad 2-18$$

It is therefore reasonable to assume that  $\alpha_l(p)$  for a non-free particle will look like:

$$\alpha_l(p) = -\frac{\pi}{2}(l+1) + \delta_l(p) \quad 2-19$$

where  $\delta_l(p)$  depends on the interaction.

It is also reasonable to assume that the wave function  $u_{\mathbf{p}}^{(+)}$ , representing a scattering particle, has the asymptotic form:

$$u_{\mathbf{p}}^{(+)}(\mathbf{x}) \xrightarrow{|\mathbf{x}| \rightarrow \infty} u_{\mathbf{p}}^{(0)}(\mathbf{x}) + \frac{1}{(2\pi\hbar)^{3/2}} \frac{e^{i\frac{pr}{\hbar}}}{r} f(\theta, \varphi; \mathbf{p}) \quad 2-20$$

where, on the right side, the first term represents the incoming free particle and the second one the outgoing particle having undergone interaction.

As the  $u_{plm}$  are a basis, then it must be possible to express  $u_{\mathbf{p}}^{(+)}$  as a linear combination of  $u_{plm}$ :

$$u_{\mathbf{p}}^{(+)}(\vec{x}) = \sum_{lm} c_{lm}(\mathbf{p}) u_{plm}(r, \theta, \varphi) \quad 2-21$$

Therefore, one can write:

$$\begin{aligned} u_{\mathbf{p}}^{(+)}(\mathbf{x}) - u_{\mathbf{p}}^{(0)}(\mathbf{x}) &= \sum_{lm} c_{lm}(\mathbf{p}) u_{plm}(r, \theta, \varphi) - c_{lm}^{(0)}(\mathbf{p}) u_{plm}^{(0)} \xrightarrow{r \rightarrow \infty} \\ &\xrightarrow{r \rightarrow \infty} \sqrt{\frac{2}{\pi\hbar}} \frac{1}{r} \sum_{lm} Y_{lm}(\theta, \varphi) \left( c_{lm}(\mathbf{p}) \cos\left(\frac{pr}{\hbar} - \frac{\pi}{2}(l+1) + \delta_l(p)\right) - c_{lm}^{(0)}(\mathbf{p}) \cos\left(\frac{pr}{\hbar} - \frac{\pi}{2}(l+1)\right) \right) = \\ &= \frac{1}{(2\pi\hbar)^{3/2}} \frac{e^{i\frac{pr}{\hbar}}}{r} f(\theta, \varphi; \mathbf{p}) \end{aligned} \quad 2-22$$

Keeping in count that, in general,  $\cos \alpha = \frac{1}{2}(e^{i\alpha} - e^{-i\alpha})$  and that  $e^{i(\alpha+\delta)} = e^{i\alpha} e^{i\delta}$  one finds the following results:

$$f(\theta, \varphi; \mathbf{p}) = \frac{\hbar}{p} \sum_{l=0}^{+\infty} e^{i\delta_l(p)} \sin \delta_l(p) (2l+1) P_l(\cos \theta_{\mathbf{p}\mathbf{x}}) \quad 2-23$$

$$u_{\mathbf{p}}^{(+)}(\mathbf{x}) = \sum_{lm} e^{i\delta_l(p)} \frac{i^l}{p} Y_{lm}^*(\alpha, \beta) u_{plm}(r, \theta, \varphi) \quad 2-24$$

where  $P_l$  is the  $l$ -th degree Legendre polynomial;  $\cos \theta_{\mathbf{p}\mathbf{x}}$  is the cosine of the scattering angle;  $\alpha, \beta$  are the polar and azimuthal angles of the vector  $\mathbf{p}$ .

Note that  $f(\theta, \varphi; \mathbf{p})$  actually depends only on  $p$  and the scattering angle  $\theta_{\mathbf{p}\mathbf{x}}$ : therefore, from now on, we prefer to deal with  $f(p, \theta_{\mathbf{p}\mathbf{x}})$ , or simply  $f(p, \theta)$  (but remember that  $\theta$  now is the scattering angle !).

Therefore the general solution will be:

$$\psi_t(\mathbf{x}) = \int d^3 p c(\mathbf{p}) u_{\mathbf{p}}^{(+)}(\mathbf{x}) e^{-i\frac{p^2 t}{2m\hbar}} \quad 2-25$$

As the intensity of the out coming wave function is essentially controlled by  $|f(p, \theta)|^2$  (see 2-20), it is consequential to assume:

$$\sigma_s(\theta, p) = |f(p, \theta)|^2 = \frac{\hbar^2}{p^2} \left| \sum_{l=0}^{+\infty} e^{i\delta_l(p)} \sin \delta_l(p) (2l+1) P_l(\cos \theta) \right|^2 \quad 2-26$$

$f(p, \theta)$  is called “scattering amplitude”.

The total scattering cross section will be (taking advantage of the orthogonality of the Legendre’s polynomials):

$$\sigma_s(p) \equiv \int d\Omega \sigma_s(\theta, p) = 2\pi \int_0^\pi d\theta \sin \theta \sigma_s(\theta, p) = \frac{\hbar^2}{p^2} 4\pi \sum_{l=0}^{\infty} \sin^2 \delta_l(p) (2l+1) \quad 2-27$$

As a matter of fact, for a short-range potential and at small energies  $\frac{p^2}{2m}$ , only the first few  $\delta_l(p)$  are significantly  $\neq 0$ , so that the sums in 2-26, 2-27 reduce to a very few terms.

This circumstance finds a rough explanation even in classical terms.

Consider a force having a potential whose (very small) range is  $r_0$ . Particles having impact parameter  $b > r_0$  don’t undergo interaction with the force. This is expressed mathematically as follows:

$$b = \frac{|\mathbf{L}|}{p} = \frac{\sqrt{\hbar l(l+1)}}{p} \approx \frac{\hbar l}{p} > r_0 \Rightarrow \delta_l(p) \approx 0 \quad 2-28$$

For very small energies the momentum will be very small and one can expect that  $\frac{\hbar l}{p} > r_0 \forall l \neq 0$ . In this case one has:

$$\sigma_s(\theta, p) = \frac{\hbar^2}{p^2} \sin^2 \delta_0(p) \quad 2-29$$

This is the circumstance that permits to assume the scattering isotropic for small energies.

Therefore, from now on, we can write:

$$\psi(r)|_{r>r_0} = \frac{1}{(2\pi\hbar)^{3/2}} e^{ikr} + \frac{1}{(2\pi\hbar)^{3/2}} \frac{e^{ikr}}{r} f(p) \quad 2-30$$

The total scattering cross section is simply (integrating  $\sigma_s(\theta, p) = |f(p, \theta)|^2 \equiv |f(p)|^2$  over all orientations):

$$\sigma_s(p) = 4\pi |f(p)|^2 \quad 2-31$$

Consider the development of a plane wave in spherical harmonics of 2-16. For simplicity, consider the wave moving parallel to the axis z. Then it will be (the terms with  $l > 0$  in the sum vanish because we refer to small energies):

$$e^{i\frac{pz}{\hbar}} = e^{i\frac{pr\cos\theta}{\hbar}} = \sum_{l=0}^{\infty} i^l (2l+1) P_l(\cos\theta) j_l\left(\frac{pr}{\hbar}\right) = \frac{\sin\frac{pr}{\hbar}}{\frac{pr}{\hbar}} = \frac{1}{2ikr} (e^{ikr} - e^{-ikr}) \quad 2-32$$

Replacing the free particle wave function in 2-30 with the development in 2-32 we obtain:

$$\psi(r)|_{r>r_0} = \frac{1}{(2\pi\hbar)^{3/2}} e^{ikz} + \frac{f(p)}{(2\pi\hbar)^{3/2}} \frac{e^{ikr}}{r} = \frac{1}{(2\pi\hbar)^{3/2}} \frac{i}{2k} \frac{e^{-ikr}}{r} + \frac{1}{(2\pi\hbar)^{3/2}} \left(f - \frac{i}{2k}\right) \frac{e^{ikr}}{r} \quad 2-33$$

where an incoming ( $-ikr$ ) and an out coming ( $ikr$ ) wave functions are recognizable.

The absorption cross section will be given by the difference between the intensities (apart from the normalization constant) of the incoming and out coming wave functions, that is:

$$\sigma_a = 4\pi \left\{ \left| \frac{i}{2k} \right|^2 - \left| f(p) - \frac{i}{2k} \right|^2 \right\} = \frac{4\pi}{k} \text{Im} f(p) - 4\pi |f(p)|^2 \quad 2-34$$

Adding 2-34 to 2-31 we obtain for the total cross section:

$$\sigma_t = \sigma_s + \sigma_a = \frac{4\pi}{k} \text{Im} f(p) \quad 2-35$$

If the neutrons' energy is lower than the energy of the nearest resonance, then the scattering amplitude will be independent of  $E$ , therefore, from now on, we will consider  $f(p) \equiv f$ .

If there is no absorption, then

$$\sigma_t = \sigma_s \Rightarrow \text{Im} f = \frac{\sigma_s}{4\pi} k \quad 2-36$$

Moreover, for very low energies  $E \rightarrow 0 \Rightarrow k \rightarrow 0$  and therefore:

$$r\psi_0(r)|_{r>r_0} \equiv u(r)|_{r>r_0} = \frac{1}{(2\pi\hbar)^{3/2}} r + \frac{1}{(2\pi\hbar)^{3/2}} \lim_{k \rightarrow 0} f \quad 2-37$$

Thus, in the limit,  $u(r)$  forms a straight line. The distance at which this line intersects the abscissa is called the scattering length and is usually denoted by  $a$ :

$$r = - \lim_{k \rightarrow 0} f \equiv a \quad 2-38$$

Therefore, from now on, neglecting the normalization constants to simplify the notation, we can write:

$$\psi(\mathbf{r})\Big|_{r>r_0} = e^{ik_0r} - a \frac{e^{ikr}}{r} \quad 2-39$$

### 2.1.3 Scattering by a fixed nucleus with spin

If the nucleus possesses a spin, then the interaction will depend on the mutual orientation of the neutron's and nucleus's spins. This can be modelled thinking of two different potentials  $V_+(r)$  and  $V_-(r)$  that govern the interaction depending on the occurring mutual spins' orientation.

In order to have a unified description of the phenomenon, we define a single potential operator:

$$\hat{V} = V_+(r)\hat{\eta}_+ + V_-(r)\hat{\eta}_- \quad 2-40$$

where  $\hat{\eta}_+$  and  $\hat{\eta}_-$  are the projection-valued measures relative respectively to the events "parallel mutual orientation of the spins" and "anti-parallel mutual orientation of the spins".

Denoting as  $\hat{\sigma}$  and  $\hat{s}$  respectively the neutron's and the nucleus's spin operator, one can easily show that:

$$\begin{aligned} \hat{\eta}_+ &= \frac{I+1+2\hat{s}\hat{\sigma}}{2I+1} \\ \hat{\eta}_- &= \frac{I-2\hat{s}\hat{\sigma}}{2I+1} \end{aligned} \quad 2-41$$

Let's consider the system of the nucleus and the neutron. Denoting with  $\psi$  the spatial part and with  $\varphi$  the spin part of their (comprehensive) wave function, we'll have, in general:

$$\Psi = \psi_+(r)\varphi_+(\sigma_z, s_z) + \psi_-(r)\varphi_-(\sigma_z, s_z) \quad 2-42$$

Let's replace the asymptotic form of  $\psi_+$  and  $\psi_-$ .

$$\psi_{\pm}(\mathbf{r}) = e^{ik_0r} - a_{\pm} \frac{e^{ikr}}{r} \quad 2-43$$

in 2-42: we obtain the asymptotic form of  $\Psi$ :

$$\Psi \xrightarrow{r \rightarrow \infty} e^{ik_0r} \varphi(\sigma_z, s_z) - (\hat{\eta}_+ a_+ + \hat{\eta}_- a_-) \varphi(\sigma_z, s_z) \frac{e^{ikr}}{r} \quad 2-44$$

and we take act that the scattering length is now an operator:

$$-(\hat{\eta}_+ a_+ + \hat{\eta}_- a_-) \equiv -\hat{a} = -\left[ \left( \frac{I+1}{2I+1} a_+ + \frac{I}{2I+1} a_- \right) + \frac{2(a_+ - a_-)}{(2I+1)} \hat{\mathbf{s}}\hat{\mathbf{G}} \right] \quad 2-45$$

The term in the square brackets not containing the spin operators determines the amplitude of that part of the wave which is scattered coherently by the nucleus. This is because this part of the scattered wave has the same spin function  $\varphi(\sigma_z, s_z)$  as the incident wave, and therefore the scattered and incident waves add (superposition). Thus, the coherent scattering length is

$$a^{coh} = \frac{I+1}{2I+1} a_+ + \frac{I}{2I+1} a_- \quad 2-46$$

The second term contains the scalar product of the nuclear and neutron spin operators:  $\hat{\mathbf{s}}\hat{\mathbf{G}}$ . Under the effect of these operators the spin function  $\varphi(\sigma_z, s_z)$  changes, and consequently, this second part of the scattered wave has a different spin-dependence. In this case superposition of the scattered and incident waves does not occur, i.e., the scattering is incoherent.

The obvious generalization of formula 2-31 to include spin will then be:

$$\sigma_s = 4\pi \left\langle \left( a^{coh} + \frac{2(a_+ - a_-)}{2I+1} \hat{\mathbf{s}}\hat{\mathbf{G}} \right)^2 \right\rangle \quad 2-47$$

The brackets denote quantum mechanical averaging and statistical averaging over the incident neutron spins (we consider a beam of unpolarized neutrons).

Developing the square in 2-47 one obtains:

$$\sigma_s = 4\pi \left\langle \left( (a^{coh})^2 + \frac{4(a_+ - a_-)^2}{(2I+1)^2} (\hat{\mathbf{s}}\hat{\mathbf{G}})^2 + \frac{4(a_+ - a_-)a^{coh}}{(2I+1)} (\hat{\mathbf{s}}\hat{\mathbf{G}}) \right) \right\rangle \quad 2-48$$

The brackets on the right side contain three addends, the third of which contains the factor  $\hat{\mathbf{s}}\hat{\mathbf{G}}$ . As the neutrons are unpolarized the statistical average  $\langle \hat{\mathbf{s}}\hat{\mathbf{G}} \rangle = 0$ , therefore the third addend is eliminated.

Developing the calculations one finds:

$$\sigma_s = 4\pi (a^{coh})^2 + \underbrace{4\pi (a_+ - a_-)^2 \frac{I(I+1)}{(2I+1)^2}}_{(a^{inc})^2} = \sigma_s^{coh} + \sigma_s^{inc} \quad 2-49$$

and the coherent/incoherent labelling is extended to the cross sections.

### 2.1.4 The Born approximation

The problem of the scattering of a neutron by a free nucleus reduces, if we pass to the system of the centre of mass of the two particles, to the problem of the scattering of a neutron with reduced mass

$$m' = \frac{mM}{m + M} \quad 2-50$$

(M is the mass of the nucleus) by a fixed nucleus.

The Schrödinger equation will be:

$$(\nabla^2 + k^2)\psi(\mathbf{r}) = \frac{2m'}{\hbar^2}V(\mathbf{r})\psi(\mathbf{r}) \quad 2-51$$

The Born approximation consists in considering the interaction between the particle and the scattering system as a perturbation, so that one can apply Fermi's Golden Rule.

Actually, the interaction of a slow neutron with a nucleus can not be seen as a perturbation, because the energy of interaction between a neutron and a nucleus is much larger than the neutron's kinetic energy and the wave function in the nucleus is totally different from the incident plane wave.

But when it comes to calculating the cross section for scattering by an atomic system, the total volume of the nuclei where the wave function is appreciably different from the initial plane wave is negligibly small compared with the volume of the entire atomic system.

It is in this context that Fermi proposed to model the interaction potential as a  $\delta$ -function:

$$V(\mathbf{r}) = C\delta(\mathbf{r}) \quad 2-52$$

where C is determined a posteriori through experimental measures.

The Green's function for the left-hand side of 2-51, that is for:

$$(\nabla^2 + k^2)\psi(\mathbf{r}) = \delta(\mathbf{r} - \mathbf{r}') \quad 2-53$$

is:

$$G(\mathbf{r}, \mathbf{r}') = -\frac{1}{4\pi} \frac{\exp\{ik|\mathbf{r} - \mathbf{r}'|\}}{|\mathbf{r} - \mathbf{r}'|} \quad 2-54$$

Consequently, one can write the general solution of the equation 2-51 as:

$$\psi(\mathbf{r}) = \psi_0(\mathbf{r}) + \int G(\mathbf{r}, \mathbf{r}') \frac{2m'}{\hbar^2} V(\mathbf{r}')\psi(\mathbf{r}') d\mathbf{r}' \quad 2-55$$

where  $\psi_0(\mathbf{r})$  is the general solution of the homogeneous equation

$$(\nabla^2 + k^2)\psi_0(\mathbf{r}) = 0 \quad 2-56$$

As the interaction is considered as a perturbation, one can look on the solution of the Schrödinger equation for the free particle 2-56 as a good approximation for the solution of equation 2-51. Therefore  $\psi(\mathbf{r}')$  in the integral in 2-55 is replaced with  $\psi_0(\mathbf{r}')$  (which is the plane wave):

$$\psi(\mathbf{r}) = e^{i\mathbf{k}_0 \cdot \mathbf{r}} - \frac{m'}{2\pi\hbar^2} \int \frac{\exp\{ik|\mathbf{r} - \mathbf{r}'|\}}{|\mathbf{r} - \mathbf{r}'|} V(r') e^{i\mathbf{k}_0 \cdot \mathbf{r}'} d\mathbf{r}' \quad 2-57$$

Through a few steps it's possible to derive the asymptotical behaviour of 2-57:

$$\psi(\mathbf{r}) \Big|_{r \rightarrow \infty} = e^{i\mathbf{k}_0 \cdot \mathbf{r}} - \frac{e^{ikr}}{r} \left[ \frac{m'}{2\pi\hbar^2} \int e^{i(\mathbf{k}_0 - \mathbf{k}) \cdot \mathbf{r}'} V(r') d\mathbf{r}' \right] \quad 2-58$$

Equating 2-58 with 2-39 (and reminding 2-52) we find:

$$-a = \frac{m'}{2\pi\hbar^2} C \quad 2-59$$

It is appropriate now to introduce:

$$a' \equiv \frac{m}{m'} a \quad 2-60$$

As announced before, C can be evaluated a posteriori on the basis of the experimental values measured for  $a'$  and replaced in the expression of  $V(\mathbf{r})$ :

$$V(\mathbf{r}) = \frac{2\pi\hbar^2}{m} a' \delta(\mathbf{r}) \quad 2-61$$

This is the so-called Fermi quasi-potential.

If the nucleus has spin then the scattering length becomes an operator, as seen in 2-45, operating on the spin functions of the nucleus and the neutron:

$$-\hat{a}' = - \left[ (a'_{coh})_+ + \frac{2(a'_+ - a'_-)}{(2I+1)} \hat{\mathbf{s}} \hat{\mathbf{G}} \right] \quad 2-62$$

The interaction of a neutron with a system of atoms is the superposition of the interactions with the individual atoms. Denoting with  $\mathbf{R}_i$  the position of the  $i$ -th atomic nucleus and using the index  $i$  to denote every quantity relative to the  $i$ -th nucleus, we can write:

$$\hat{V}(\mathbf{r}, \mathbf{R}_1, \dots, \mathbf{R}_N) = \frac{2\pi\hbar^2}{m} \sum_{i=1}^N \left[ a'_i{}^{coh} + \frac{2(a'_{i+} - a'_{i-})}{(2I_i + 1)} \hat{\mathbf{s}}_i \hat{\mathbf{G}} \right] \delta(\mathbf{r} - \mathbf{R}_i) \quad 2-63$$

### Fermi's Golden Rule and cross section in Born approximation

Assume a certain unperturbed Hamiltonian  $\hat{H}_0$ , having eigenfunctions  $u_{ns}$ , where  $s$  is a degeneration index referring to the eigenvalues  $a_s$  of an operator  $\hat{A}$  (corresponding to an observable). That is:

$$\hat{H}_0 u_{ns} = E_n u_{ns} \quad 2-64$$

with

$$\begin{aligned} [\hat{H}_0, \hat{A}] &= 0 \\ \hat{A} u_{ns} &= a_s u_{ns} \end{aligned} \quad 2-65$$

Then in presence of a small time-independent perturbation  $\hat{V}$ , so that the new Hamiltonian looks like

$$\hat{H} = \hat{H}_0 + \hat{V} \quad 2-66$$

the Fermi's Golden Rule states that the probability per unit of time to have a transition between an initial state  $\mathbf{v}_0$  and a final state between  $\mathbf{v}$  and  $\mathbf{v}+d\mathbf{v}$  is

$$dw_{\mathbf{v}_0\mathbf{v}} = \frac{2\pi}{\hbar} \left| \langle \psi_{\mathbf{v}} | \hat{V} | \psi_{\mathbf{v}_0} \rangle \right|^2 \delta(E_{\mathbf{v}} - E_{\mathbf{v}_0}) d\mathbf{v} \quad 2-67$$

where  $\psi$  is the wave function of the whole system neutron-scatterer. Both in the initial and in the final state the scatterer and the neutron are independent, therefore  $\psi$  is simply the product of their individual wave functions, respectively  $\Gamma(\mathbf{R}_i)$  and  $\Phi(\mathbf{r})$ :

$$\psi(\mathbf{R}_1, \dots, \mathbf{R}_N, \mathbf{r}) = \Gamma(\mathbf{R}_1, \dots, \mathbf{R}_N) \Phi(\mathbf{r}) \quad 2-68$$

Both in the initial and in the final state the neutron is free, and hence the spectrum of  $\hat{H}_0$  is continuous. Therefore it can be useful to consider  $\hat{H}_0$  as limit of an operator with a discrete spectrum: if we enclose the whole system in a cube of side  $L$  and require that the neutron's wave function is periodic on the box's walls, then its spatial part will be:

$$\Phi(\mathbf{r}) = \frac{1}{(L)^{3/2}} e^{i\mathbf{k}\cdot\mathbf{r}} \quad 2-69$$

where the vector  $\mathbf{k}$  will look like this:

$$\mathbf{k} = \left( n_x \frac{2\pi}{L}, n_y \frac{2\pi}{L}, n_z \frac{2\pi}{L} \right) \quad n_x, n_y, n_z = 0, \pm 1, \pm 2, \dots \quad 2-70$$

The number of final states therefore is  $d\mathbf{v} = \left( \frac{L}{2\pi} \right)^3 d\mathbf{k}$ .

Reminding 2-68, we can split off the integration over  $d\mathbf{r}$ :

$$\begin{aligned} \langle \psi_v | \hat{V} | \psi_{v_0} \rangle &= \\ &= \int d\mathbf{r} L^{-3/2} e^{-i\mathbf{k}\cdot\mathbf{r}} \langle \Gamma_{\tau}(\mathbf{R}_1, \dots, \mathbf{R}_N) | \hat{V}(\mathbf{R}_1, \dots, \mathbf{R}_N, \mathbf{r}) | \Gamma_{\tau_0}(\mathbf{R}_1, \dots, \mathbf{R}_N) \rangle L^{-3/2} e^{i\mathbf{k}_0\cdot\mathbf{r}} \end{aligned} \quad 2-71$$

where  $\tau_0$  and  $\tau$  are respectively the initial and final state of the scatterer.

For the same reason, the energy in the initial and final states is additive:

$$E_{v_0} = E_{\tau_0} + \frac{\hbar^2 k_0^2}{2m}, \quad E_v = E_{\tau} + \frac{\hbar^2 k^2}{2m} \quad 2-72$$

In conclusion, picking up formula 2-67:

$$\begin{aligned} dw &= \frac{L^{-3}}{(2\pi)^2 \hbar} \left| \int d\mathbf{r} e^{-i\mathbf{\kappa}\cdot\mathbf{r}} \langle \Gamma_{\tau}(\mathbf{R}_1, \dots, \mathbf{R}_N) | \hat{V}(\mathbf{R}_1, \dots, \mathbf{R}_N, \mathbf{r}) | \Gamma_{\tau_0}(\mathbf{R}_1, \dots, \mathbf{R}_N) \rangle \right|^2 \\ &\quad \times \delta \left[ E_{\tau} - E_{\tau_0} + \frac{\hbar^2}{2m} (k^2 - k_0^2) \right] d\mathbf{k} \end{aligned} \quad 2-73$$

where  $\mathbf{\kappa} \equiv \mathbf{k} - \mathbf{k}_0$ .

In order to obtain the differential cross section  $d\sigma$ ,  $dw$  must be divided by the flux, which is the product of the density  $L^{-3}$  and the initial velocity  $v_0 = \frac{\hbar k_0}{m}$ .

As in a real scattering experiment the final state of the scatterer can't be ascertained, then in order to have the expression of a quantity that we can really compare to experimental measurements, we sum over all possible scatterer's final states  $\tau$ .

Further, in order to pass to the more common second-order differential cross sections over the angles and energies  $d^2\sigma/d\Omega dE$  we apply the following relations:

$$\begin{aligned} dE &= \frac{\hbar^2 k dk}{m} \\ d\mathbf{k} &= k^2 dk d\Omega = \frac{mk}{\hbar^2} d\Omega dE \end{aligned} \quad 2-74$$

and we obtain:

$$\begin{aligned} \frac{d^2\sigma}{d\Omega dE} &= \frac{m^2}{(2\pi)^2 \hbar^4} \frac{k}{k_0} \\ &\times \sum_{\tau} \left| \int d\mathbf{r} e^{-i\mathbf{\kappa}\cdot\mathbf{r}} \langle \Gamma_{\tau}(\mathbf{R}_1, \dots) | \hat{V}(\mathbf{R}_1, \dots, \mathbf{r}) | \Gamma_{\tau_0}(\mathbf{R}_1, \dots) \rangle \right|^2 \delta \left[ E_{\tau} - E_{\tau_0} + \frac{\hbar^2}{2m} (k^2 - k_0^2) \right] \end{aligned} \quad 2-75$$

Replacing in 2-75 the expression of the potential 2-63, we obtain after some calculation:

$$\frac{d^2\sigma}{d\Omega dE} = \frac{d^2\sigma^{coh}}{d\Omega dE} + \frac{d^2\sigma^{inc}}{d\Omega dE} \quad 2-76$$

with

$$\frac{d^2\sigma^{coh}}{d\Omega dE} = \frac{k}{k_0} \sum_{\tau} \left| \sum_{i=1}^N a_i^{coh} \langle \Gamma_{\tau}(\mathbf{R}_1, \dots) | e^{-i\mathbf{k}\cdot\mathbf{R}_i} | \Gamma_{\tau_0}(\mathbf{R}_1, \dots) \rangle \right|^2 \delta[E_{\tau} - E_{\tau_0} + E - E_0] \quad 2-77$$

$$\frac{d^2\sigma^{inc}}{d\Omega dE} = \frac{k}{k_0} \sum_{\tau} \sum_{i=1}^N (a_i^{inc})^2 \left| \langle \Gamma_{\tau}(\mathbf{R}_1, \dots) | e^{-i\mathbf{k}\cdot\mathbf{R}_i} | \Gamma_{\tau_0}(\mathbf{R}_1, \dots) \rangle \right|^2 \delta[E_{\tau} - E_{\tau_0} + E - E_0] \quad 2-78$$

Note that in the formula for the coherent part of the scattering, the matrix elements corresponding to scattering by various atoms are added, and the sum is then squared. This means that waves scattered by various atoms interfere, and the cross section for scattering by the system as a whole is not equal to the sum of the cross sections for scattering by the individual atoms.

The incoherent cross section, on the contrary, has the form of a sum over the cross sections for scattering by all the atoms, since the matrix elements are first squared, and then summed.

## 2.2 Literature

### 2.2.1 The formalism of Zemach and Glauber

As seen in paragraph 2.1.4, the potential affecting the neutron is the sum of the potentials generated by the nuclei of the scatterer's atoms.

Now let's assume the scattering independent from spin. Denoting by the index  $n$  the neutron and by the index  $\nu$  the nuclei the Fermi pseudo-potential will be<sup>3</sup>:

$$V(\mathbf{r}_n) = \sum_{\nu} V(\mathbf{r}_n, \mathbf{r}_{\nu}) = \frac{2\pi}{m} \sum_{\nu} a_{\nu} \delta(\mathbf{r}_n - \mathbf{r}_{\nu}) \quad 2-79$$

in which  $m$  is the neutron mass and  $a$  the bound scattering length.

Replacing the expression of the potential in formula 2-75 found for the cross section, we have:

$$\begin{aligned} \sigma_{fi}(\theta) &= \left( \frac{m}{2\pi} \right)^2 \left( \frac{k}{k_0} \right) \left| \langle \psi_f | \int e^{-i(\mathbf{k}-\mathbf{k}_0)\cdot\mathbf{r}_n} V(\mathbf{r}_n) d\tau_n | \psi_i \rangle \right|^2 = \\ &= \sum_{\nu, \nu'} a_{\nu} a_{\nu'} \left( \frac{k}{k_0} \right) \langle \psi_i | \int e^{i(\mathbf{k}-\mathbf{k}_0)\cdot\mathbf{r}_{\nu}} | \psi_f \rangle \langle \psi_f | \int e^{-i(\mathbf{k}-\mathbf{k}_0)\cdot\mathbf{r}_{\nu'}} | \psi_i \rangle \end{aligned} \quad 2-80$$

The total cross section for a neutron in the initial state  $i$  is the sum of the cross sections over all possible final states  $f$ :

---

<sup>3</sup> A system of units in which  $\hbar$  has unit magnitude is employed from now on.

$$\sigma_i(\theta) = \sum_f \int_{-\varepsilon_0}^{\infty} d\varepsilon \delta(E_i - E_f - \varepsilon) \sigma_{fi}(\theta) \quad 2-81$$

where we have introduced the notation:

$$\varepsilon = E_i - E_f = \left( \frac{1}{2m} \right) (k^2 - k_0^2) \quad 2-82$$

The integral in 2-81 is carried out starting from  $-\varepsilon_0 = -\frac{k_0^2}{2m}$ , consistently with the fact that the neutron can not lose more than its initial energy  $\varepsilon_0$ .

Then the  $\delta$  in 2-81 is replaced with its integral representation, according to the formula:

$$\delta(x) = \frac{1}{2\pi} \int_{-\infty}^{+\infty} e^{ixt} dt \quad 2-83$$

obtaining

$$\sigma_i(\theta) = \frac{1}{2\pi} \sum_f \int_{-\varepsilon_0}^{\infty} d\varepsilon \int_{-\infty}^{\infty} dt e^{-i\varepsilon t} e^{i(E_i - E_f)t} \sigma_{fi}(\theta) \quad 2-84$$

and  $\exp(-iE_f t) \psi_f$  is replaced by  $\exp(-i\hat{H}t) \psi_f$ , obtaining

$$\begin{aligned} \sigma_i(\theta) &= (2\pi)^{-1} \\ &\times \sum_{v,v',f} a_v a_{v'} \iint (k/k_0) e^{-i\varepsilon t} \langle \psi_i | e^{i\hat{H}t} \exp(i\mathbf{k} \cdot \mathbf{r}_v) e^{-i\hat{H}t} | \psi_f \rangle \langle \psi_f | \exp(-i\mathbf{k} \cdot \mathbf{r}_{v'}) | \psi_i \rangle dt d\varepsilon \end{aligned} \quad 2-85$$

Carrying out the sum over the index f (final state) and differentiating with respect to  $\varepsilon$  we get

$$\sigma_i(\theta, \varepsilon) = (k/2\pi k_0) \sum_{v,v'} a_v a_{v'} \int e^{-i\varepsilon t} \langle \psi_i | e^{i\hat{H}t} \exp(i\mathbf{k} \cdot \mathbf{r}_v) e^{-i\hat{H}t} \exp(-i\mathbf{k} \cdot \mathbf{r}_{v'}) | \psi_i \rangle dt \quad 2-86$$

We define the operator

$$\mathbf{r}(t) \equiv e^{i\hat{H}t} \mathbf{r} e^{-i\hat{H}t} \quad 2-87$$

The definition is justified because effectively:

$$\langle \psi(\mathbf{r}, 0) | e^{i\hat{H}t} \mathbf{r} e^{-i\hat{H}t} | \psi(\mathbf{r}, 0) \rangle = \langle e^{-i\hat{H}t} \psi(\mathbf{r}, 0) | \mathbf{r} | e^{-i\hat{H}t} \psi(\mathbf{r}, 0) \rangle = \langle \psi(\mathbf{r}, t) | \mathbf{r} | \psi(\mathbf{r}, t) \rangle = \langle \mathbf{r}(t) \rangle \quad 2-88$$

Applying this device to the expectation value appearing in 2-86 we obtain a more compact form of it:

$$\begin{aligned} \langle \psi_i | e^{i\hat{H}t} \exp(i\mathbf{k} \cdot \mathbf{r}_v) e^{-i\hat{H}t} \exp(-i\mathbf{k} \cdot \mathbf{r}_{v'}) | \psi_i \rangle &= \langle \psi_i | \exp[i\mathbf{k} \cdot \mathbf{r}_v(t)] \exp[-i\mathbf{k} \cdot \mathbf{r}_{v'}(0)] | \psi_i \rangle \\ &\equiv \chi_{vv'}^i \end{aligned} \quad 2-89$$

Formula 2-86 represents the differential cross section for a molecule in a certain initial state  $i$ .

With the following notation we indicate its average over a distribution of molecular states in thermal equilibrium at temperature  $T$ :

$$\langle \sigma(\theta, \varepsilon) \rangle_T = (k/2\pi k_0) \sum_{v, v'} a_v a_{v'} \int e^{-i\varepsilon t} \langle \chi_{vv'} \rangle_T dt \quad 2-90$$

It is convenient to explode the coordinates of the nuclei into a sum of terms corresponding to the various degrees of freedom.

In general, the position of the  $v$ th nucleus of a molecule in space will be represented by a vector  $\mathbf{r}_v$ , which can be decomposed as follows:

$$\mathbf{r}_v = \mathbf{R} + \mathbf{b}_v + \mathbf{u}_v \quad 2-91$$

where  $\mathbf{R}$  is the position of the molecular centre of mass,  $\mathbf{b}_v$  is the displacement of the equilibrium position of the nucleus from the molecular mass centre,  $\mathbf{u}_v$  the displacement of this nucleus from its equilibrium position due to vibration.

The molecular Hamiltonian is taken as the sum of the Hamiltonians for the translational, rotational and vibrational motions of the molecule. If we neglect rotation-vibration interactions then we can write:

$$\hat{H} = \hat{H}_{vib} + \hat{H}_{rot} + \hat{H}_{trans} \quad 2-92$$

and correspondingly the spatial part of the wave functions will assume the form:

$$\psi = \psi_{vib} \psi_{rot} \psi_{trans} \quad 2-93$$

Considering the oscillations harmonic, we can introduce the set of normal coordinates  $q_\lambda$  and express the displacement from the equilibrium position of each nucleus as the superposition of the displacements due to each normal mode:

$$\mathbf{u}_v(t) = \sum_\lambda \mathbf{c}_v^{(\lambda)}(t) q_\lambda(t) \quad 2-94$$

where  $\mathbf{c}_v^{(\lambda)}(t)$  is the amplitude vector corresponding to the  $v$ th nucleus and the  $\lambda$ th vibrational mode.

Therefore we can write:

$$\mathbf{r}_v(t) = \mathbf{R}(t) + \mathbf{b}_v(t) + \sum_\lambda \mathbf{c}_v^{(\lambda)}(t) q_\lambda(t) \quad 2-95$$

Thanks to 2-91 and 2-93 we have:

$$\begin{aligned}
\chi_{vv'} &\equiv \langle \psi | \exp[i\mathbf{k} \cdot \mathbf{r}_v(t)] \exp[-i\mathbf{k} \cdot \mathbf{r}_v(0)] | \psi \rangle \\
&= \langle \psi_{vib}(\mathbf{u}_v) \psi_{rot}(\mathbf{b}_v) \psi_{trans}(\mathbf{R}) | \exp\{i\mathbf{k} \cdot [\mathbf{R}(t) + \mathbf{b}_v(t) + \mathbf{u}_v(t)]\} \\
&\quad \times \exp[-i\mathbf{k} \cdot [\mathbf{R}(0) + \mathbf{b}_v(0) + \mathbf{u}_v(0)]] | \psi_{vib}(\mathbf{u}_v) \psi_{rot}(\mathbf{b}_v) \psi_{trans}(\mathbf{R}) \rangle \\
&= \langle \psi_{vib}(\mathbf{u}_v) | \exp[i\mathbf{k} \cdot \mathbf{u}_v(t)] \exp[-i\mathbf{k} \cdot \mathbf{u}_v(0)] | \psi_{vib}(\mathbf{u}_v) \rangle \\
&\quad \times \langle \psi_{rot}(\mathbf{b}_v) | \exp[i\mathbf{k} \cdot \mathbf{b}_v(t)] \exp[-i\mathbf{k} \cdot \mathbf{b}_v(0)] | \psi_{rot}(\mathbf{b}_v) \rangle \\
&\quad \times \langle \psi_{trans}(\mathbf{R}) | \exp[i\mathbf{k} \cdot \mathbf{R}(t)] \exp[-i\mathbf{k} \cdot \mathbf{R}(0)] | \psi_{trans}(\mathbf{R}) \rangle \\
&= \chi_{vv'}^v \chi_{vv'}^r \chi_{vv'}^t
\end{aligned} \tag{2-96}$$

that is,  $\chi_{vv'}$  may be split off into factors corresponding to vibration, rotation and translation.

The usual experimental conditions don't consist of one single system prepared in the initial state  $\psi$ , but in a set of systems in thermal equilibrium at a certain temperature  $T$ . Therefore the real quantity of interest is

$$\langle \chi_{vv'} \rangle_T = \frac{[\sum_i \chi_{vv'}^i \exp(-E_i/T)]}{[\sum_i \exp(-E_i/T)]} \tag{2-97}$$

The subscript  $T$  indicates the statistical mean over the states of a thermal distribution of systems at temperature  $T$ .

By consequence of 2-96:

$$\langle \chi_{vv'} \rangle_T = \langle \chi_{vv'}^v \rangle_T \langle \chi_{vv'}^r \rangle_T \langle \chi_{vv'}^t \rangle_T \tag{2-98}$$

The dependence of 2-98 on the molecular orientation  $\Omega$  is contained in the rotational and vibrational factors.

The whole problem of the scattering, hence, comes down to calculating  $\chi_{vv'}^v$ ,  $\chi_{vv'}^r$ ,  $\chi_{vv'}^t$  and their averages.

## 2.2.2 Scattering by vibrators

The problem comes down to the calculation of the expectation value

$$\chi_{vv'}^v \equiv \langle \psi_i | \exp[i\mathbf{k} \cdot \sum_{\lambda} \mathbf{c}_v^{(\lambda)} \hat{q}_{\lambda}(t)] \exp[-i\mathbf{k} \cdot \sum_{\lambda} \mathbf{c}_v^{(\lambda)} \hat{q}_{\lambda}(0)] | \psi_i \rangle \tag{2-99}$$

and its thermal and orientational averages.

As the normal modes are dynamically independent, the normal coordinates of different modes commute with each other and the exponential functions of  $\mathbf{u}_v(t)$  may be factored into products of exponentials as follows

$$\exp[i\mathbf{k} \cdot \sum_{\lambda} \mathbf{c}_v^{(\lambda)} \hat{q}_{\lambda}(t)] = \prod_{\lambda} \exp[i\mathbf{k} \cdot \mathbf{c}_v^{(\lambda)} \hat{q}_{\lambda}(t)] \tag{2-100}$$

Thanks to the Equipartition Theorem, the Maxwell-Boltzmann thermal distribution function for the molecule as a whole may also be expressed as a product of factors, one for each mode. Therefore:

$$\langle \mathcal{X}_{vv'} \rangle_T = \prod_{\lambda} \langle \mathcal{X}_{vv'}^{(\lambda)} \rangle_T = \prod_{\lambda} \langle \exp[i\mathbf{k} \cdot \mathbf{c}_v^{(\lambda)} \hat{q}_{\lambda}(t)] \exp[-i\mathbf{k} \cdot \mathbf{c}_{v'}^{(\lambda)} \hat{q}_{\lambda}(0)] \rangle_T \quad 2-101$$

The Baker-Campbell-Hausdorff formula<sup>4</sup>, for two operators  $\hat{A}$  and  $\hat{B}$  that commute with their commutator  $[\hat{A}, \hat{B}]$  reduces to:

$$e^{\hat{A}} e^{\hat{B}} = e^{\hat{A} + \hat{B} + \frac{1}{2}[\hat{A}, \hat{B}]} \quad 2-102$$

Applying it to each factor  $\langle \mathcal{X}_{vv'}^{(\lambda)} \rangle_T$  in 2-101 yields:

$$\begin{aligned} \langle \mathcal{X}_{vv'}^{(\lambda)} \rangle_T &= \langle \exp[i\mathbf{k} \cdot \mathbf{c}_v^{(\lambda)} \hat{q}_{\lambda}(t)] \exp[-i\mathbf{k} \cdot \mathbf{c}_{v'}^{(\lambda)} \hat{q}_{\lambda}(0)] \rangle_T = \\ &= \left\langle \exp[i[\mathbf{k} \cdot \mathbf{c}_v \hat{q}_{\lambda}(t) - \mathbf{k} \cdot \mathbf{c}_{v'} \hat{q}_{\lambda}(0)]] \exp\left\{\frac{1}{2}(\mathbf{k} \cdot \mathbf{c}_v)(\mathbf{k} \cdot \mathbf{c}_{v'})[\hat{q}_{\lambda}(t)\hat{q}_{\lambda}(0)]\right\} \right\rangle_T \end{aligned} \quad 2-103$$

According to a corollary of Bloch's theorem on the distribution function of an oscillator coordinate, if we let  $Q$  be any multiple of an oscillator coordinate or linear combination of them, we have

$$\langle \exp Q \rangle_T = \exp\left\{\frac{1}{2}\langle Q^2 \rangle_T\right\} \quad 2-104$$

Applying it to 2-103 and noting that expectation values of  $\hat{q}_{\lambda}^2(t)$  are the same as those of  $\hat{q}_{\lambda}^2(0)$  we find

$$\langle \mathcal{X}_{vv'}^{(\lambda)} \rangle_T = \exp\left\{-\frac{1}{2}\left[(\mathbf{k} \cdot \mathbf{c}_v^{(\lambda)})^2 + (\mathbf{k} \cdot \mathbf{c}_{v'}^{(\lambda)})^2\right]\langle \hat{q}_{\lambda}^2(0) \rangle_T + (\mathbf{k} \cdot \mathbf{c}_v^{(\lambda)})(\mathbf{k} \cdot \mathbf{c}_{v'}^{(\lambda)})\langle \hat{q}_{\lambda}(t)\hat{q}_{\lambda}(0) \rangle_T\right\} \quad 2-105$$

In order to find the time-dependence of  $\hat{q}_{\lambda}(t)$ , as we are referring to a harmonic oscillator, we first calculate the time dependence of the creation and annihilation operators in general (we omit the index  $\lambda$ ):

$$\left. \begin{aligned} \frac{d}{dt}\langle \hat{a} \rangle_t &= \langle \psi_t | \frac{1}{i\hbar} [\hat{a}, \hat{H}] | \psi_t \rangle \\ \hat{H} &= \hbar\omega \left( \hat{a}^+ \hat{a} + \frac{1}{2} \right) \\ [\hat{a}, \hat{a}^+] &= 1 \end{aligned} \right\} \Rightarrow i\hbar \frac{d}{dt}\langle \hat{a} \rangle_t = \hbar\omega \langle \hat{a} \rangle_t \Rightarrow \hat{a}(t) = \hat{a} e^{-i\omega t} \quad 2-106$$

---

<sup>4</sup>  $e^{\hat{A}} e^{\hat{B}} = e^{\hat{A} + \hat{B} + \frac{1}{2}[\hat{A}, \hat{B}] + \frac{1}{12}([\hat{A}, [\hat{A}, \hat{B}]] + [\hat{B}, [\hat{B}, \hat{A}]] + \dots)}$

The same way one finds that:

$$\hat{a}^+(t) = \hat{a}^+ e^{i\omega t} \quad 2-107$$

Reminding that for a harmonic oscillator of unit mass:

$$\hat{a} \equiv \frac{1}{\sqrt{2}} \left( \sqrt{\omega} \hat{q} + \frac{i}{\sqrt{\omega}} \hat{p} \right) \quad 2-108$$

it follows that:

$$\hat{q} = \sqrt{\frac{1}{2\omega}} (\hat{a} + \hat{a}^+) \quad 2-109$$

and therefore

$$\hat{q}(t) = \sqrt{\frac{1}{2\omega}} (\hat{a} e^{-i\omega t} + \hat{a}^+ e^{i\omega t}) \quad 2-110$$

Now we can calculate  $\langle \hat{q}_\lambda(t) \hat{q}_\lambda(0) \rangle_T$ :

$$\left. \begin{aligned} \hat{q}_\lambda(t) &= \sqrt{\frac{1}{2\omega}} (\hat{a}_\lambda e^{-i\omega_\lambda t} + \hat{a}_\lambda^+ e^{i\omega_\lambda t}) \\ [\hat{a}_\lambda, \hat{a}_\lambda^+] &= 1 \\ \hat{n}_\lambda &\equiv \hat{a}_\lambda^+ \hat{a}_\lambda \end{aligned} \right\} \Rightarrow \quad 2-111$$

$$\Rightarrow \langle \hat{q}_\lambda(t) \hat{q}_\lambda(0) \rangle_T = \frac{1}{2\omega_\lambda} \{ (\langle \hat{n}_\lambda \rangle_T + 1) e^{-i\omega_\lambda t} + \langle \hat{n}_\lambda \rangle_T e^{i\omega_\lambda t} \}$$

Replacing  $\langle \hat{q}_\lambda(t) \hat{q}_\lambda(0) \rangle_T$  and  $\langle \hat{q}_\lambda^2(0) \rangle$  in 2-105 and performing the thermal average we obtain:

$$\begin{aligned} \langle \chi_{vv'}^{(\lambda)} \rangle_T &= \exp \left\{ -\frac{1}{2} \left[ (\mathbf{k} \cdot \mathbf{c}_v^{(\lambda)})^2 + (\mathbf{k} \cdot \mathbf{c}_{v'}^{(\lambda)})^2 \right] \frac{(z_\lambda + 1)}{2\omega_\lambda (z_\lambda - 1)} \right\} \\ &\times \exp \left\{ (\mathbf{k} \cdot \mathbf{c}_v^{(\lambda)}) (\mathbf{k} \cdot \mathbf{c}_{v'}^{(\lambda)}) z_\lambda \frac{1}{2} \frac{(z_\lambda^{1/2} e^{-i\omega_\lambda t} + z_\lambda^{-1/2} e^{i\omega_\lambda t})}{2\omega_\lambda (z_\lambda - 1)} \right\} \end{aligned} \quad 2-112$$

where

$$z_\lambda = \exp \left( \frac{\omega_\lambda}{T} \right) \quad 2-113$$

In 2-111, 2-112 and 2-113  $\omega_\lambda$  is the angular frequency of the one-dimensional harmonic oscillator of unit mass whose normal coordinate is  $q_\lambda(t)$ .

Considering formula 2-112 with attention, one can notice that  $\langle \chi_{vv'}^{(\lambda)} \rangle_T$  depends on time through the terms  $e^{-i\omega_\lambda t}$  and  $e^{i\omega_\lambda t}$ . Therefore  $\langle \chi_{vv'}^{(\lambda)} \rangle_T$  is periodic in time and can be expanded in Fourier series, obtaining

$$\begin{aligned} \langle \chi_{vv'}^{(\lambda)} \rangle_T &= \exp\left\{-\left[\left(\mathbf{\kappa} \cdot \mathbf{c}_v^{(\lambda)}\right)^2 + \left(\mathbf{\kappa} \cdot \mathbf{c}_{v'}^{(\lambda)}\right)^2\right] \frac{1}{4\omega_\lambda} \coth\left(\frac{\omega_\lambda}{2T}\right)\right\} \\ &\times \sum_{n=-\infty}^{\infty} e^{in\omega_\lambda t} e^{-(n\omega_\lambda/2T)} I_n\left(\frac{\left(\mathbf{\kappa} \cdot \mathbf{c}_v^{(\lambda)}\right)\left(\mathbf{\kappa} \cdot \mathbf{c}_{v'}^{(\lambda)}\right)}{2\omega_\lambda \sinh(\omega_\lambda/2T)}\right) \end{aligned} \quad 2-114$$

where  $I_n$  is the modified Bessel function.

### 2.2.3 Scattering by rotators

We remind the expression of a particle's (probability-) distribution of momentum (in one spatial dimension for simplicity):

$$|c(p_x, t)|^2 \equiv \left| \frac{1}{\hbar^{1/2}} \mathcal{F}(\psi) \left( \frac{p_x}{\hbar} \right) \right|^2 = \left| \frac{1}{(2\pi\hbar)^{1/2}} \int d^3x e^{-i\frac{p_x x}{\hbar}} \psi(x, t) \right|^2 \quad 2-115$$

The Fourier transform is a unitary operator, therefore:

$$\begin{aligned} \langle \hat{p}_x \rangle &= \langle \psi(x, t) | -i\hbar \frac{\partial}{\partial x} | \psi(x, t) \rangle = \langle \psi(x, t) | \mathcal{F}^{-1} x \mathcal{F} | \psi(x, t) \rangle = \langle \mathcal{F}[\psi(x, t)] | p_x | \mathcal{F}[\psi(x, t)] \rangle \\ &= \langle \hbar^{1/2} c(p_x, t) | p_x | \hbar^{1/2} c(p_x, t) \rangle = \hbar \langle c(p_x, t) | p_x | c(p_x, t) \rangle \end{aligned} \quad 2-116$$

and hence:

$$\begin{aligned} \langle \hat{p}_x - \hat{\kappa} \rangle &\equiv \hbar \langle c(p_x) | p_x - \kappa | c(p_x) \rangle = \hbar \langle c(p_x + \kappa) | p_x | c(p_x + \kappa) \rangle \\ &= \hbar \left\langle \frac{1}{\hbar^{1/2}} \mathcal{F}[e^{-i\kappa x} \psi(x, t)] \middle| \mathcal{F} \hat{p}_x \mathcal{F}^{-1} \middle| \frac{1}{\hbar^{1/2}} \mathcal{F}[e^{-i\kappa x} \psi(x, t)] \right\rangle \\ &= \langle e^{-i\kappa x} \psi(x, t) | \hat{p}_x | e^{-i\kappa x} \psi(x, t) \rangle \\ &= \langle \psi(x, t) | e^{i\kappa x} \hat{p}_x e^{-i\kappa x} | \psi(x, t) \rangle \end{aligned} \quad 2-117$$

In conclusion:

$$\hat{p}_x - \hat{\kappa} = e^{i\kappa x} \hat{p}_x e^{-i\kappa x} \quad 2-118$$

and therefore, in general:

$$e^{i\mathbf{\kappa} \cdot \mathbf{r}_v} \hat{H}(\mathbf{p}_v, \mathbf{r}_v) e^{-i\mathbf{\kappa} \cdot \mathbf{r}_v} = \hat{H}(\mathbf{p}_v - \mathbf{\kappa}, \mathbf{r}_v) \equiv \hat{H}'_v \quad 2-119$$

Using the operator of time-evolution we can expand  $\chi'_{vv'}$  as follows:

$$\begin{aligned}\langle \chi_{vv'}^r \rangle &= \langle \psi^r | \exp[i\boldsymbol{\kappa} \cdot \mathbf{b}_v(t)] \exp[-i\boldsymbol{\kappa} \cdot \mathbf{b}_{v'}(0)] | \psi^r \rangle = \\ &= \langle \psi^r | \exp(i\hat{H}_{rot}t) \exp[i\boldsymbol{\kappa} \cdot \mathbf{b}_v(0)] \exp(-i\hat{H}_{rot}t) \exp[-i\boldsymbol{\kappa} \cdot \mathbf{b}_{v'}(0)] | \psi^r \rangle\end{aligned}\quad 2-120$$

We introduce the innocuous factor  $\exp[-i\boldsymbol{\kappa} \cdot \mathbf{b}_v(0)] \exp[i\boldsymbol{\kappa} \cdot \mathbf{b}_v(0)]$ :

$$\begin{aligned}\langle \chi_{vv'}^r \rangle &= \langle \psi^r | \exp(i\hat{H}_{rot}t) \exp[i\boldsymbol{\kappa} \cdot \mathbf{b}_v(0)] \exp(-i\hat{H}_{rot}t) \\ &\times \exp[-i\boldsymbol{\kappa} \cdot \mathbf{b}_v(0)] \exp[i\boldsymbol{\kappa} \cdot \mathbf{b}_v(0)] \exp[-i\boldsymbol{\kappa} \cdot \mathbf{b}_{v'}(0)] | \psi^r \rangle\end{aligned}\quad 2-121$$

In agreement with 2-119 we write:

$$\exp(i\boldsymbol{\kappa} \cdot \mathbf{b}_v) \hat{H}_{rot}(\hat{\mathbf{p}}_v, \mathbf{b}_v) \exp(-i\boldsymbol{\kappa} \cdot \mathbf{b}_v) = \hat{H}_{rot}(\hat{\mathbf{p}}_v - \boldsymbol{\kappa}, \mathbf{b}_v) \equiv \hat{H}'_{rot(v)} \quad 2-122$$

and it follows immediately that

$$\exp(i\boldsymbol{\kappa} \cdot \mathbf{b}_v) e^{-i\hat{H}_{rot}(\mathbf{b}_v, \hat{\mathbf{p}}_v)t} \exp(-i\boldsymbol{\kappa} \cdot \mathbf{b}_{v'}) = e^{-i\hat{H}'_{rot}(\mathbf{b}_v, \hat{\mathbf{p}}_v - \boldsymbol{\kappa})t} = e^{-i\hat{H}'_{rot(v)}t} \quad 2-123$$

so that 2-120 can be rewritten as follows:

$$\langle \chi_{vv'}^r \rangle = \langle \psi^r | \exp(i\hat{H}_{rot}t) \exp(-i\hat{H}'_{rot(v)}t) \exp[i\boldsymbol{\kappa} \cdot \mathbf{b}_v(0)] \exp[-i\boldsymbol{\kappa} \cdot \mathbf{b}_{v'}(0)] | \psi^r \rangle \quad 2-124$$

with

$$\hat{H}_{rot} = \frac{1}{2} \hat{\mathbf{L}} \cdot \mathfrak{S}^{-1} \cdot \hat{\mathbf{L}} = \frac{1}{2} \left( \sum_i \mathbf{b}_i \times \hat{\mathbf{p}}_i \right) \cdot \mathfrak{S}^{-1} \cdot \left( \sum_j \mathbf{b}_j \times \hat{\mathbf{p}}_j \right) \equiv \frac{1}{2} \sum_{i,j} \hat{\mathbf{p}}_i \cdot \mathfrak{R}_{ij} \cdot \hat{\mathbf{p}}_j \quad 2-125$$

where  $\mathfrak{S}$  is the moment of inertia tensor.

Replacing 2-125 in 2-124, with the help of some simplifying approximation and carrying out the thermal average one obtains:

$$\langle \chi_{vv'}^r \rangle_T = \exp\{i\boldsymbol{\kappa} \cdot [\mathbf{b}_v(0) - \mathbf{b}_{v'}(0)]\} \exp\left\{-\frac{1}{2} (\boldsymbol{\kappa} \cdot \mathfrak{R}_{vv'} \cdot \boldsymbol{\kappa}) (it + Tt^2)\right\} \quad 2-126$$

## 2.2.4 Scattering by molecules

As far as the translational part  $\langle \chi_{vv'}^r \rangle_T$  is concerned, calculations can be simplified considering wave functions  $\psi$  which are eigenfunctions of momentum and energy. Then we have:

$$\langle \psi | e^{i\hat{H}t} e^{-i\hat{H}t} | \psi \rangle = \exp[it(2\mathbf{p} \cdot \boldsymbol{\kappa} - \kappa^2)/2M] \quad 2-127$$

where  $\mathbf{p}$  now specifies a momentum eigenvalue;  $M$  is the molecular mass. It follows that

$$\langle \chi_{vv'}^r \rangle_T = \langle \psi | e^{i\hat{H}t} e^{-i\hat{H}t} | \psi \rangle_T = \int \langle \psi | e^{i\hat{H}t} e^{-i\hat{H}t} | \psi \rangle f_T(\mathbf{p}) d\mathbf{p} = \exp\left[\frac{-it\kappa^2}{2M} - \frac{t^2 T \kappa^2}{2M}\right] \quad 2-128$$

where  $f_T(\mathbf{p})$  is the Boltzmann weighting factor:

$$f_T(\mathbf{p}) = (2\pi MT)^{-\frac{3}{2}} \exp(-p^2 / 2MT) \quad 2-129$$

Combining 2-126 and 2-128 gives:

$$\langle \chi_{vv'}^t \rangle_T \langle \chi_{vv'}^r \rangle_T = \exp\{i\mathbf{\kappa} \cdot [\mathbf{b}_v(0) - \mathbf{b}_{v'}(0)]\} \exp\left\{-\frac{1}{2}(\mathbf{\kappa} \cdot \mathbf{M}_v^{-1} \cdot \mathbf{\kappa})(it + Tt^2)\right\} \quad 2-130$$

with

$$\mathbf{M}_v^{-1} \equiv \mathbf{R}_{vv} + M^{-1}\mathbf{1} \quad 2-131$$

where  $\mathbf{1}$  is the unit tensor.

It is interesting to notice that, apart from the factor  $\exp\{i\mathbf{\kappa} \cdot [\mathbf{b}_v(0) - \mathbf{b}_{v'}(0)]\}$ , the structure of the expression of  $\langle \chi_{vv'}^t \rangle \langle \chi_{vv'}^r \rangle$  is formally identical to the one of  $\langle \chi_{vv'}^t \rangle$ , with the mass  $M$  replaced by the tensor  $\mathbf{M}_v$  (compare 2-128 and 2-130). This means that, applying some approximation, the problem of neutron scattering with a roto-translating molecule (no vibrations) can be simplified as the scattering with a hypothetical single mass point, as long as one replaces its scalar mass with an appropriate mass tensor, which accounts for the different hypothetical mass point's inertia as a function of the direction with which it is struck.

Although the present treatment of scattering by molecules is mainly due to T. J. Krieger and M. S. Nelkin [6], who worked upon foundations cast by A. C. Zemach and R. J. Glauber ([7] and [8]), the idea of simplifying the neutron's scattering against a roto-translating molecule through the introduction of the mass tensor was first introduced in an article by R. G. Sachs and E. Teller [9]. Therefore  $\mathbf{M}_v$  is usually called the "Sachs and Teller mass tensor".

Under assumption of neutron energies below the vibrational threshold and molecules initially in their ground vibrational states (that is,  $T=0$  for vibrations) the expression 2-112 for  $\langle \chi_{vv'}^v \rangle$  reduces to:

$$\langle \chi_{vv'}^v \rangle_{T=0} = \prod_{\lambda} \exp\left\{-\frac{1}{4\omega_{\lambda}} \left[ (\mathbf{\kappa} \cdot \mathbf{c}_v^{(\lambda)})^2 + (\mathbf{\kappa} \cdot \mathbf{c}_{v'}^{(\lambda)})^2 \right]\right\} \quad 2-132$$

At this point  $\langle \chi_{vv'} \rangle_T$  is obtained replacing 2-130 and 2-132 in 2-98, so that it yields the following product of three factors:

$$\begin{aligned}
\langle \chi_{vv'} \rangle_T &= \exp\{i\mathbf{k} \cdot [\mathbf{b}_v(0) - \mathbf{b}_{v'}(0)]\} \\
&\times \exp\left\{-\frac{1}{2}(\mathbf{k} \cdot \mathbf{M}_v^{-1} \cdot \mathbf{k})(it + Tt^2)\right\} \\
&\times \prod_{\lambda} \exp\left\{-\frac{1}{4\omega_{\lambda}} \left[ (\mathbf{k} \cdot \mathbf{c}_v^{(\lambda)})^2 + (\mathbf{k} \cdot \mathbf{c}_{v'}^{(\lambda)})^2 \right]\right\}
\end{aligned} \tag{2-133}$$

In order to simplify the averaging over molecular orientations, Krieger and Nelkin propose to approximate the average of the product as the product of the averages [6].

The result is:

$$\langle \chi_{vv'} \rangle_{T,\Omega} = j_0(\kappa b_{vv'}) \exp(-\kappa^2 \gamma_{vv'}) \exp\left\{-\kappa^2 (2M_v^{(0)})^{-1} (it + Tt^2)\right\} \tag{2-134}$$

where

$$\gamma_{vv'} = \sum_{\lambda} \frac{1}{12\omega_{\lambda}} \left[ (c_v^{(\lambda)})^2 + (c_{v'}^{(\lambda)})^2 \right] \tag{2-135}$$

and

$$[M_v^{(0)}]^{-1} = \frac{1}{3} \text{Spur}[\mathbf{M}_v^{-1}] \tag{2-136}$$

### 2.2.5 Scattering of slow neutrons by liquid water

Nelkin's treatment of neutrons' scattering in water [10] is based on neglecting the interference scattering involving correlations in position among pairs of protons in the scattering system. This is justified by the predominantly incoherent nature of the scattering by hydrogen atoms and by the assumption that the temperature is not so low that nuclear spin correlations become important.

Apart from this, from a conceptual point of view, Nelkin mainly relies on the theory developed for free molecules, with the three degrees of freedom still considered independent from each other, so that the  $\chi$  can still be expressed as the product of  $\chi^t$ ,  $\chi^r$ ,  $\chi^v$ , introducing some refinement with respect to the molecular gas model only in  $\chi^r$ .

The molecule is considered free to translate as in gases, so that:

$$\langle \chi^t \rangle_T \approx e^{-(\kappa^2/2M)(it+Tt^2)} \tag{2-137}$$

as seen in the previous paragraph. The constant M takes on the value of 18: atomic weight of the molecule of water.

The treatment of the vibrational motions of the atoms of hydrogen in the molecule of water is kept as is, passing from the free molecule to liquid water.

We report the vibrational component of  $\langle \chi_{\nu\nu'} \rangle_T$ , found in 2.2.2:

$$\begin{aligned} \langle \chi_{\nu\nu'} \rangle_T &= \prod_{\lambda} \langle \chi_{\nu\nu'}^{(\lambda)} \rangle_T = \\ &= \prod_{\lambda} \exp \left\{ -\frac{1}{2} \left[ (\mathbf{k} \cdot \mathbf{c}_{\nu}^{(\lambda)})^2 + (\mathbf{k} \cdot \mathbf{c}_{\nu'}^{(\lambda)})^2 \right] \langle \hat{q}_{\lambda}^2(0) \rangle_T + (\mathbf{k} \cdot \mathbf{c}_{\nu}^{(\lambda)}) (\mathbf{k} \cdot \mathbf{c}_{\nu'}^{(\lambda)}) \langle \hat{q}_{\lambda}(t) \hat{q}_{\lambda}(0) \rangle_T \right\} \end{aligned} \quad 2-138$$

Neglecting the interference scattering between the two hydrogen atoms in the molecule of water means that in 2-138 we consider only  $\nu = \nu'$  so that we have:

$$\langle \chi_{\nu\nu} \rangle_T = \prod_{\lambda} \exp \left\{ -(\mathbf{k} \cdot \mathbf{c}_{\nu}^{(\lambda)})^2 \langle \hat{q}_{\lambda}^2(0) \rangle_T + (\mathbf{k} \cdot \mathbf{c}_{\nu}^{(\lambda)})^2 \langle \hat{q}_{\lambda}(t) \hat{q}_{\lambda}(0) \rangle_T \right\} \quad 2-139$$

We replace  $\langle \hat{q}_{\lambda}^2(0) \rangle_T$  and  $\langle \hat{q}_{\lambda}(t) \hat{q}_{\lambda}(0) \rangle_T$  using formula 2-111 and we obtain:

$$\langle \chi^{\nu}(\mathbf{k}, T, t) \rangle_T = e^{\left[ \sum_{\lambda=1}^N (\mathbf{k} \cdot \mathbf{c}^{(\lambda)})^2 f(\omega_{\lambda}, T, t) \right]} \quad 2-140$$

where

$$f(\omega_{\lambda}, T, t) = \frac{1}{2\omega_{\lambda}} \left[ \langle \hat{n}_{\lambda} \rangle_T + 1 \right] (e^{-i\omega_{\lambda}t} - 1) + \langle \hat{n}_{\lambda} \rangle_T (e^{i\omega_{\lambda}t} - 1) \quad 2-141$$

and

$$\langle \hat{n}_{\lambda} \rangle_T = [\exp(\omega_{\lambda}/T) - 1]^{-1} \quad 2-142$$

The energies of the molecular vibrations are assumed to be the same in liquid water as in water vapour (that is, the free molecule). These have been measured through spectrometry experiments to be 0.205 eV, 0.474 eV and 0.488 eV.

Nelkin proposes to assume that the two higher-frequency vibrational modes are degenerate so that they are blended in a unique intermediate energy of 0.481 eV.

Therefore, after averaging over orientations one obtains:

$$\langle \chi^{\nu} \rangle_{T, \Omega} = \exp \left[ \frac{K^2}{6m_{\nu}\omega_1} (e^{-i\omega_1 t} - 1) \right] \exp \left[ \frac{K^2}{3m_{\nu}\omega_2} (e^{-i\omega_2 t} - 1) \right] \quad 2-143$$

with  $\hbar\omega_1 = 0.205$  eV,  $\hbar\omega_2 = 0.481$  eV and  $m_{\nu} = 1.95$ .

The hindered rotations of a molecule in a liquid are modelled through a torsional harmonic oscillator with a single frequency  $\omega_r$ . The expression for  $\langle \chi^r \rangle_T$  describing the neutron scattering from such a torsional oscillator has been shown by Krieger to be [10]:

$$\langle \chi^r \rangle_T = \exp[(\mathbf{K} \cdot \mathbf{R} \cdot \mathbf{K}) f(\omega_r, T, t)] \quad 2-144$$

with

$$\mathbf{R} = \mathbf{M}^{-1} - M^{-1}\mathbf{1} \quad 2-145$$

where  $\mathbf{M}$  is the Sachs and Teller mass tensor (and  $M = 18$ ).

On the basis of experiments of neutronic spectrometry,  $\hbar\omega_r$  is set to a value of 0.06 eV.

Averaging over molecular orientations gives

$$\langle \chi^r \rangle_{T,\Omega} \approx \exp\left[\left(K^2/m_r\right)f(\omega_r, T, t)\right] \quad 2-146$$

We report the expression of the differential energy-transfer cross-section from 2.2.1:

$$\langle \sigma(\theta, \varepsilon) \rangle_T = (k/2\pi k_0) \sum_{v'} a_v a_{v'} \int e^{-i\varepsilon t} \langle \chi_{vv'} \rangle_T dt \quad 2-147$$

In the case of an atom of hydrogen in the molecule of water, neglecting interference and reminding that  $\sigma_b = 4\pi a^2$ , it takes on the form:

$$\langle \sigma(E_0, E, \theta) \rangle_{T,\Omega} = \left( \frac{\sigma_b}{8\pi^2} \right) \left( \frac{E}{E_0} \right)^{\frac{1}{2}} \int_{-\infty}^{\infty} dt e^{-i\varepsilon t} \langle \chi_{vv'} \rangle_{T,\Omega} \quad 2-148$$

where  $\sigma_b = 81.2$  barns is the bound-hydrogen cross-section and  $\chi = \chi^t \chi^r \chi^y$ .

Figure 2-1 shows a comparison between theoretical and experimental values of the total cross section as a function of energy.

The theoretical total cross section has been obtained integrating 2-148 numerically over final energy and scattering angle.

The experimental points are those of Melkonian [11], as read from the cross-section compilation BNL-325 [12].

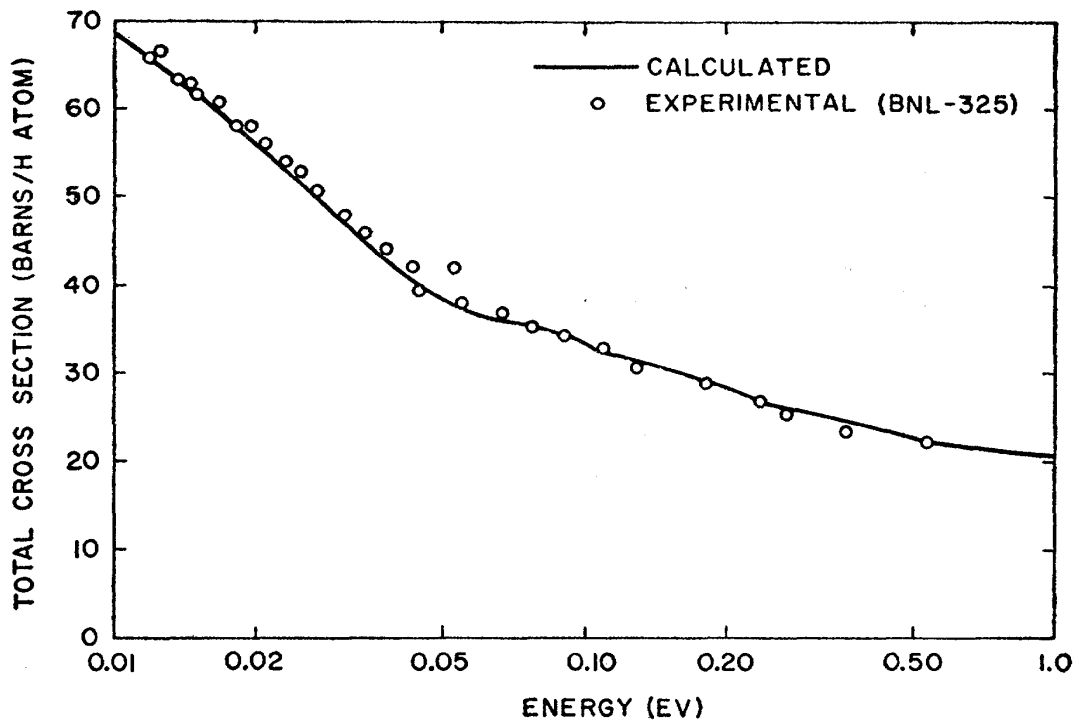


Figure 2-1: The total cross section of water in barns per hydrogen atom as a function of incident neutron energy.

The agreement between theory and experiment in the range from 0.01 eV to 1.0 eV is good. According to Nelkin, the deviation in the neighbourhood of 0.05 eV is probably due to the assumption of a single torsional frequency in the calculation.

Nelkin also proposes a direct comparison of theory and experiment for  $\sigma(E_0, E, \theta)$ : he considers the measurement of Brockhouse [13] for  $E_0 = 0.065$  eV and  $\theta = 90$  deg. The comparison is shown in Figure 2-2.

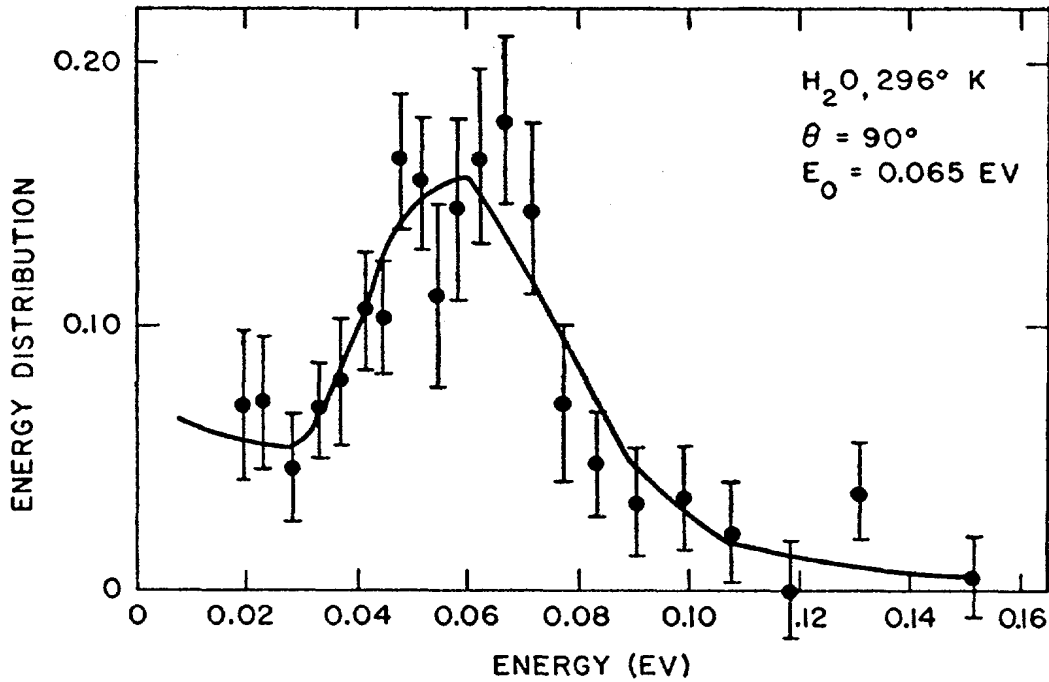


Figure 2-2: The energy distribution of neutrons of incident energy 0.065 eV after scattering through 90 deg by water.

The agreement is well within the large experimental error.

Though the encouraging results shown in Figure 2-1 and Figure 2-2, Nelkin reminds that a number of experimental measurements are available that show direct evidence, in their structure for small energy transfer, for the hindrance of the translational motions in the liquid. This model can't represent these features, because we assumed free translations.

## 2.3 Modern methods

### 2.3.1 The Van Hove formalism

Let us consider the scattering of slow neutrons by a system of  $N$  identical atoms.

The initial state of the scatterer is usually indefinite, therefore the cross sections described by 2-77 and 2-78 must be averaged over its possible initial states. For a system in thermodynamic equilibrium at a temperature  $T$ , the probabilities for different states are given by Gibbs' distribution:

$$p_{\tau_0} = \frac{e^{-E_{\tau_0}/T}}{\sum_{\tau_0} e^{-E_{\tau_0}/T}} \quad 2-149$$

We also divide 2-77 and 2-78 by  $N$ , in order to obtain the scattering cross sections per atom<sup>5</sup>:

$$\left\langle \frac{d^2 \sigma^{coh}}{d\Omega dE} \right\rangle_T = \frac{1}{N} \frac{k}{k_0} \sum_{\tau_0} p_{\tau_0} \sum_{\tau} (a'^{coh})^2 \left| \sum_{i=1}^N [e^{-i\mathbf{k} \cdot \mathbf{R}_i}]_{\tau_0}^{\tau} \right|^2 \frac{1}{\hbar} \delta \left[ \frac{E_{\tau} - E_{\tau_0}}{\hbar} - \omega \right] \quad 2-150$$

$$\left\langle \frac{d^2 \sigma^{inc}}{d\Omega dE} \right\rangle_T = \frac{1}{N} \frac{k}{k_0} \sum_{\tau_0} p_{\tau_0} \sum_{\tau} (a'^{inc})^2 \sum_{i=1}^N \left| [e^{-i\mathbf{k} \cdot \mathbf{R}_i}]_{\tau_0}^{\tau} \right|^2 \frac{1}{\hbar} \delta \left[ \frac{E_{\tau} - E_{\tau_0}}{\hbar} - \omega \right] \quad 2-151$$

2-150 and 2-151 are usually written in the form:

$$\left\langle \frac{d^2 \sigma^{coh}}{d\Omega dE} \right\rangle_T = \frac{k}{k_0} (a'^{coh})^2 \hbar^{-1} S^{coh}(\mathbf{k}, \omega) \quad 2-152$$

$$\left\langle \frac{d^2 \sigma^{inc}}{d\Omega dE} \right\rangle_T = \frac{k}{k_0} (a'^{inc})^2 \hbar^{-1} S^{inc}(\mathbf{k}, \omega) \quad 2-153$$

The functions  $S^{coh}(\mathbf{k}, \omega)$  and  $S^{inc}(\mathbf{k}, \omega)$  are called the coherent and incoherent *scattering laws*.

Reminding the integral representation of the delta function

$$\delta(x) = \frac{1}{2\pi} \int_{-\infty}^{\infty} dt \exp(itx) \quad 2-154$$

we can rewrite the expression of  $S^{coh}(\mathbf{k}, \omega)$ :

$$\begin{aligned} S^{coh}(\mathbf{k}, \omega) &= \\ &= \sum_{\tau_0} p_{\tau_0} \sum_{\tau} \frac{1}{N} \left| \sum_{i=1}^N [e^{-i\mathbf{k} \cdot \mathbf{R}_i}]_{\tau_0}^{\tau} \right|^2 \frac{1}{2\pi} \int_{-\infty}^{\infty} dt \exp\left(i \frac{E_{\tau}}{\hbar} t\right) \exp\left(-i \frac{E_{\tau_0}}{\hbar} t\right) \exp(-i\omega t) = \\ &= \frac{1}{2\pi N} \sum_{\tau_0} p_{\tau_0} \int_{-\infty}^{\infty} dt \exp(-i\omega t) \sum_{\tau} \sum_{i,j=1}^N [e^{-i\mathbf{k} \cdot \mathbf{R}_j}]_{\tau_0}^{\tau} [e^{i\mathbf{k} \cdot \mathbf{R}_i}]_{\tau}^{\tau_0} \exp\left(i \frac{E_{\tau}}{\hbar} t\right) \exp\left(-i \frac{E_{\tau_0}}{\hbar} t\right) \end{aligned} \quad 2-155$$

If we apply the following device:

---

<sup>5</sup> We adopt the following notation:  $[\hat{A}]_{\tau_0}^{\tau} \equiv \langle \Gamma_{\tau}(\mathbf{R}_1, \mathbf{R}_2, \dots, \mathbf{R}_N) | \hat{A} | \Gamma_{\tau_0}(\mathbf{R}_1, \mathbf{R}_2, \dots, \mathbf{R}_N) \rangle$

$$\begin{aligned}
& \left[ e^{-i\mathbf{k}\cdot\mathbf{R}_j} \right]_{\tau_0}^{\tau} \exp\left(i\frac{E_{\tau}}{\hbar}t\right) \exp\left(-i\frac{E_{\tau_0}}{\hbar}t\right) = \\
& = \langle \Gamma_{\tau}(\mathbf{R}_1, \mathbf{R}_2, \dots, \mathbf{R}_N) | e^{-i\mathbf{k}\cdot\mathbf{R}_j} | \Gamma_{\tau_0}(\mathbf{R}_1, \mathbf{R}_2, \dots, \mathbf{R}_N) \rangle \exp\left(i\frac{E_{\tau}}{\hbar}t\right) \exp\left(-i\frac{E_{\tau_0}}{\hbar}t\right) = \\
& = \left\langle \exp\left(-i\frac{E_{\tau}}{\hbar}t\right) \Gamma_{\tau}(\mathbf{R}_1, \mathbf{R}_2, \dots, \mathbf{R}_N) \middle| e^{-i\mathbf{k}\cdot\mathbf{R}_j} \middle| \exp\left(-i\frac{E_{\tau_0}}{\hbar}t\right) \Gamma_{\tau_0}(\mathbf{R}_1, \mathbf{R}_2, \dots, \mathbf{R}_N) \right\rangle = \\
& = \left\langle \exp\left(-i\frac{\hat{H}}{\hbar}t\right) \Gamma_{\tau}(\mathbf{R}_1, \mathbf{R}_2, \dots, \mathbf{R}_N) \middle| e^{-i\mathbf{k}\cdot\mathbf{R}_j} \middle| \exp\left(-i\frac{\hat{H}}{\hbar}t\right) \Gamma_{\tau_0}(\mathbf{R}_1, \mathbf{R}_2, \dots, \mathbf{R}_N) \right\rangle = \\
& = \langle \Gamma_{\tau}(\mathbf{R}_1, \mathbf{R}_2, \dots, \mathbf{R}_N) | \exp\left(i\frac{\hat{H}}{\hbar}t\right) e^{-i\mathbf{k}\cdot\mathbf{R}_j} \exp\left(-i\frac{\hat{H}}{\hbar}t\right) | \Gamma_{\tau_0}(\mathbf{R}_1, \mathbf{R}_2, \dots, \mathbf{R}_N) \rangle = \\
& = \langle \Gamma_{\tau}(\mathbf{R}_1, \mathbf{R}_2, \dots, \mathbf{R}_N) | e^{-i\mathbf{k}\cdot\mathbf{R}_j(t)} | \Gamma_{\tau_0}(\mathbf{R}_1, \mathbf{R}_2, \dots, \mathbf{R}_N) \rangle
\end{aligned} \tag{2-156}$$

then the expression of  $S^{\text{coh}}(\mathbf{k}, \omega)$  becomes:

$$\begin{aligned}
S^{\text{coh}}(\mathbf{k}, \omega) &= \frac{1}{2\pi N} \sum_{i,j=1}^N \sum_{\tau_0} p_{\tau_0} \int_{-\infty}^{\infty} dt \exp(-i\omega t) \sum_{\tau} \langle \Gamma_{\tau_0}(\mathbf{R}_1, \dots, \mathbf{R}_N) | e^{i\mathbf{k}\cdot\mathbf{R}_i} | \Gamma_{\tau}(\mathbf{R}_1, \dots, \mathbf{R}_N) \rangle \\
&\quad \times \langle \Gamma_{\tau}(\mathbf{R}_1, \dots, \mathbf{R}_N) | e^{-i\mathbf{k}\cdot\mathbf{R}_j(t)} | \Gamma_{\tau_0}(\mathbf{R}_1, \dots, \mathbf{R}_N) \rangle \\
&= \frac{1}{2\pi} \int_{-\infty}^{\infty} dt \exp(-i\omega t) \frac{1}{N} \sum_{i,j=1}^N \sum_{\tau_0} p_{\tau_0} \left[ e^{i\mathbf{k}\cdot\mathbf{R}_i} e^{-i\mathbf{k}\cdot\mathbf{R}_j(t)} \right]_{\tau_0}^{\tau_0} \equiv \\
&\equiv \frac{1}{2\pi} \int_{-\infty}^{\infty} dt \exp(-i\omega t) \frac{1}{N} \sum_{i,j=1}^N \left\langle e^{i\mathbf{k}\cdot\mathbf{R}_i} e^{-i\mathbf{k}\cdot\mathbf{R}_j(t)} \right\rangle_T \equiv \\
&\equiv \frac{1}{2\pi} \int_{-\infty}^{\infty} dt \exp(-i\omega t) \frac{1}{N} \sum_{i,j=1}^N \langle \chi_{ij}(\mathbf{k}, t) \rangle_T \equiv \frac{1}{2\pi} \int_{-\infty}^{\infty} dt \exp(-i\omega t) \langle \chi(\mathbf{k}, t) \rangle_T
\end{aligned} \tag{2-157}$$

where we consistently find again the intermediate scattering function  $\chi(\mathbf{k}, t)$ .

In a similar way, one can prove that:

$$S^{\text{inc}}(\mathbf{k}, \omega) = \frac{1}{2\pi} \int_{-\infty}^{\infty} dt \exp(-i\omega t) \langle \chi_s(\mathbf{k}, t) \rangle_T \equiv \frac{1}{2\pi} \int_{-\infty}^{\infty} dt \exp(-i\omega t) \frac{1}{N} \sum_{i=1}^N \langle \chi_{ii}(\mathbf{k}, t) \rangle_T \tag{2-158}$$

In the notation of  $\chi_s(\mathbf{k}, t)$ , the subscript ‘‘s’’ stands for ‘‘self’’.

Notice that the effects of the scatterer dynamics are entirely contained in the intermediate scattering functions.

In conclusion, we can write:

$$S(\mathbf{k}, \omega) = \frac{1}{2\pi} \int_{-\infty}^{\infty} dt \exp(-i\omega t) \left[ \langle \chi(\mathbf{k}, t) \rangle_T + \langle \chi_s(\mathbf{k}, t) \rangle_T \right] \tag{2-159}$$

where

$$S(\mathbf{k}, \omega) = S^{\text{coh}}(\mathbf{k}, \omega) + S^{\text{inc}}(\mathbf{k}, \omega) \tag{2-160}$$

We can now introduce the correlation function  $G(\mathbf{r},t)$ :

$$\begin{aligned} G(\mathbf{r},t) &\equiv \frac{1}{(2\pi)^3} \int d^3\kappa d\omega e^{i\kappa\cdot\mathbf{r}} e^{i\omega t} S^{coh}(\boldsymbol{\kappa},\omega) = \frac{1}{(2\pi)^3} \int d^3\kappa e^{i\kappa\cdot\mathbf{r}} \langle \chi(\boldsymbol{\kappa},t) \rangle_T = \\ &= \frac{1}{(2\pi)^3} \frac{1}{N} \sum_{i,j=1}^N \left\langle \int d^3\kappa e^{i\kappa\cdot\mathbf{r}} e^{i\kappa\cdot\mathbf{R}_i} e^{-i\kappa\cdot\mathbf{R}_j(t)} \right\rangle_T \end{aligned} \quad 2-161$$

Applying the integral representation of the three-dimensional  $\delta$ :

$$\delta(\boldsymbol{\kappa}' - \boldsymbol{\kappa}) = \frac{1}{(2\pi)^3} \int d^3r' e^{i(\boldsymbol{\kappa}' - \boldsymbol{\kappa})\cdot\mathbf{r}'} \quad 2-162$$

one can show that:

$$G(\mathbf{r},t) = \frac{1}{N} \left\langle \sum_{i,j=1}^N \int d\mathbf{r}' \delta(\mathbf{r} + \mathbf{R}_i - \mathbf{r}') \delta(\mathbf{r}' - \mathbf{R}_j(t)) \right\rangle_T \quad 2-163$$

Note that  $\mathbf{R}_i$  and  $\mathbf{R}_j(t)$  in quantum-mechanical calculations don't commute. But if we consider 2-163 from a classical point of view then we can write:

$$G^c(\mathbf{r},t) = \frac{1}{(2\pi)^3} \frac{1}{N} \sum_{i,j=1}^N \left\langle \int d^3\kappa e^{i\kappa\cdot(\mathbf{r} + \mathbf{R}_i - \mathbf{R}_j(t))} \right\rangle_T = \frac{1}{N} \sum_{i,j=1}^N \left\langle \delta(\mathbf{r} + \mathbf{R}_i - \mathbf{R}_j(t)) \right\rangle_T \quad 2-164$$

where the superscript ‘‘c’’ stands for ‘‘classical’’.

The average of the  $\delta$ -function involved in 2-164 is therefore the probability that at time  $t$  the  $j$ -th atom will be at the point  $\mathbf{r}$  with respect to the position of the  $i$ -th atom at the time  $t = 0$ .  $G^c(\mathbf{r},t)$  is obtained by summing this probability over  $j$  and averaging over  $i$ . Thus,  $G^c(\mathbf{r},t)$  gives the average density of atoms at the point  $\mathbf{r}$  at the time  $t$ , if some atom was at the origin of the coordinates  $\mathbf{r} = 0$ , at  $t = 0$  i.e., it gives the correlation in the positions of two atoms (which could also coincide) at different instants. The function  $G^c(\mathbf{r},t)$  may be called the space-time pair correlation function.

The function  $G(\mathbf{r},t)$  determined by formula 2-163 is the quantum-mechanical equivalent of the space-time pair correlation function  $G^c(\mathbf{r},t)$ .

If we decompose  $G(\mathbf{r},t)$  as follows:

$$\begin{aligned} G(\mathbf{r},t) &= \frac{1}{N} \left\langle \sum_{i=1}^N \int d\mathbf{r}' \delta(\mathbf{r} + \mathbf{R}_i - \mathbf{r}') \delta(\mathbf{r}' - \mathbf{R}_i(t)) \right\rangle_T + \\ &\quad + \frac{1}{N} \left\langle \sum_{i \neq j=1}^N \int d\mathbf{r}' \delta(\mathbf{r} + \mathbf{R}_i - \mathbf{r}') \delta(\mathbf{r}' - \mathbf{R}_j(t)) \right\rangle_T \\ &\equiv G_s(\mathbf{r},t) + G_d(\mathbf{r},t) \end{aligned} \quad 2-165$$

then correspondingly we have:

$$\begin{aligned}
G^c(\mathbf{r}, t) &= G_s^c(\mathbf{r}, t) + G_d^c(\mathbf{r}, t) = \\
&= \frac{1}{N} \sum_{i=1}^N \langle \delta(\mathbf{r} + \mathbf{R}_i - \mathbf{R}_i(t)) \rangle_T + \frac{1}{N} \sum_{i \neq j=1}^N \langle \delta(\mathbf{r} + \mathbf{R}_i - \mathbf{R}_j(t)) \rangle_T
\end{aligned} \tag{2-166}$$

If the system can be considered as consisting of distinguishable particles (Boltzmann statistics), then this separation takes on a physical meaning: the function  $G_s(\mathbf{r}, t)$  is the space-time self-correlation function, i.e., its classical limit  $G_s^c(\mathbf{r}, t)$  is the probability of a particle that was at the origin at time  $t = 0$  being at the point  $\mathbf{r}$  at time  $t$ . The function  $G_d(\mathbf{r}, t)$  has the same meaning as  $G(\mathbf{r}, t)$  except that the density considered at time  $t$  consists of all the particles except the one which was situated at the origin at  $t = 0$ , i.e. all “different” particles.

According to 2-152 and 2-153 we can express the second-order differential cross section in the form:

$$\left\langle \frac{d^2\sigma}{d\Omega dE} \right\rangle_T = \left( \frac{E_f}{E_i} \right)^{1/2} \hbar^{-1} \left[ (a'^{coh})^2 S^{coh}(\mathbf{k}, \omega) + (a'^{inc})^2 S^{inc}(\mathbf{k}, \omega) \right] \tag{2-167}$$

It results that for hydrogen, the “free atom” coherent and incoherent scattering lengths are:

$$\begin{aligned}
a_{inc}^2 &= 1.586 \cdot 10^{-24} \text{ cm}^2 \\
a_{coh}^2 &= 0.0357 \cdot 10^{-24} \text{ cm}^2
\end{aligned}$$

Therefore from now on we can focus only on the incoherent contribution to the cross section:

$$\left\langle \frac{d^2\sigma}{d\Omega dE} \right\rangle_T \approx \left( \frac{E_f}{E_i} \right)^{1/2} \hbar^{-1} (a'^{inc})^2 S^{inc}(\mathbf{k}, \omega) \tag{2-168}$$

We remind that, according to 2-159:

$$S^{inc}(\mathbf{k}, \omega) = \frac{1}{2\pi} \int_{-\infty}^{\infty} dt \exp(-i\omega t) \chi_s(\mathbf{k}, t) \tag{2-169}$$

Therefore:

$$\begin{aligned}
G_s(\mathbf{r}, t) &\equiv \frac{1}{(2\pi)^3} \frac{1}{N} \sum_{i=1}^N \left\langle \int d^3\mathbf{k} e^{i\mathbf{k}\cdot\mathbf{r}} e^{i\mathbf{k}\cdot\mathbf{R}_i} e^{-i\mathbf{k}\cdot\mathbf{R}_i(t)} \right\rangle_T = \\
&= \frac{1}{(2\pi)^3} \int d^3\mathbf{k} e^{i\mathbf{k}\cdot\mathbf{r}} \frac{1}{N} \sum_{i=1}^N \left\langle e^{i\mathbf{k}\cdot\mathbf{R}_i} e^{-i\mathbf{k}\cdot\mathbf{R}_i(t)} \right\rangle_T \equiv \\
&\equiv \frac{1}{(2\pi)^3} \int d^3\mathbf{k} e^{i\mathbf{k}\cdot\mathbf{r}} \langle \chi_s(\mathbf{k}, t) \rangle_T = \frac{1}{(2\pi)^3} \int d^3\mathbf{k} d\omega e^{i\mathbf{k}\cdot\mathbf{r}} e^{i\omega t} S^{inc}(\mathbf{k}, \omega)
\end{aligned} \tag{2-170}$$

In conclusion, from now on we can write:

$$\begin{aligned} \left\langle \frac{d^2 \sigma}{d\Omega dE} \right\rangle_T &\approx \left( \frac{E_f}{E_i} \right)^{1/2} \hbar^{-1} (a'^{inc})^2 S^{inc}(\mathbf{\kappa}, \omega) = \\ &= \left( \frac{E_f}{E_i} \right)^{1/2} \hbar^{-1} (a'^{inc})^2 \frac{1}{2\pi} \int d^3 r dt \exp(-i\mathbf{\kappa} \cdot \mathbf{r}) \exp(-i\omega t) G_s(\mathbf{r}, t) \end{aligned} \quad 2-171$$

and therefore our attention will be directed only at incoherent scattering.

$G_s(\mathbf{r}, t)$  strictly depends on the dynamics of the particles that compose the scatterer. This means that the scattering of slow neutrons depends on the dynamics of the particles composing the scatterer: if we know the Hamiltonian of the scatterer then, in principle, we can infer the second-order differential cross section.

### 2.3.2 Phonons in solids

We consider a harmonic crystal, so that the interaction potential of the system is assumed to be a sum of pair potentials, each having a quadratic dependence on the atomic displacements. In order to reduce the number of force constants we restrict our attention to only nearest neighbour interactions.

With these premises, the crystal can be modelled as a set of  $N$  harmonic oscillators (each atom in its quadratic potential hole) that are interdependent. But through the introduction of normal coordinates, the Hamiltonian is diagonalized and the problem reduces to  $N$  independent harmonic oscillators.

We calculated in paragraph 2.2.2 the intermediate scattering function for such a system. We found:

$$\begin{aligned} \langle \chi_{vv'}^{(\lambda)} \rangle_T &= \exp \left\{ -\frac{1}{2} \left[ (\mathbf{\kappa} \cdot \mathbf{c}_v^{(\lambda)})^2 + (\mathbf{\kappa} \cdot \mathbf{c}_{v'}^{(\lambda)})^2 \right] \frac{(z_\lambda + 1)}{2\omega_\lambda(z_\lambda - 1)} \right\} \\ &\times \exp \left\{ (\mathbf{\kappa} \cdot \mathbf{c}_v^{(\lambda)}) (\mathbf{\kappa} \cdot \mathbf{c}_{v'}^{(\lambda)}) z_\lambda^{-1/2} \frac{(z_\lambda^{1/2} e^{-i\omega_\lambda t} + z_\lambda^{-1/2} e^{i\omega_\lambda t})}{2\omega_\lambda(z_\lambda - 1)} \right\} \end{aligned} \quad 2-172$$

where

$$z_\lambda = \exp \left( \frac{\omega_\lambda}{T} \right) \quad 2-173$$

We consider the incoherent part (so  $v = v'$ ), and we suppose that the solid under consideration is a simple Bravais lattice (one atom per unit cell, therefore the index  $v$  can only be equal to 1 and can be eliminated):

$$\begin{aligned}
\langle \chi_s \rangle_T &\equiv \sum_{\nu=1}^1 \prod_{\lambda} \langle \chi_{\nu\nu}^{(\lambda)} \rangle_T = \\
&= \prod_{\lambda} \exp \left\{ - \left( \mathbf{k} \cdot \mathbf{c}^{(\lambda)} \right)^2 \frac{(z_{\lambda} + 1)}{2\omega_{\lambda}(z_{\lambda} - 1)} \right\} \exp \left\{ \left( \mathbf{k} \cdot \mathbf{c}^{(\lambda)} \right)^2 z_{\lambda}^{\frac{1}{2}} \frac{(z_{\lambda}^{1/2} e^{-i\omega_{\lambda}t} + z_{\lambda}^{-1/2} e^{i\omega_{\lambda}t})}{2\omega_{\lambda}(z_{\lambda} - 1)} \right\} = \\
&= \prod_{\lambda} \exp \left\{ - \frac{(\mathbf{k} \cdot \mathbf{c}^{(\lambda)})^2}{2\omega_{\lambda}} \coth \left( \frac{\omega_{\lambda}}{2T} \right) \right\} \exp \left\{ \frac{(\mathbf{k} \cdot \mathbf{c}^{(\lambda)})^2}{2\omega_{\lambda}} \frac{\cosh(\omega_{\lambda}/2T - i\omega_{\lambda}t)}{\sinh(\omega_{\lambda}/2T)} \right\} = \\
&= \exp \left\{ \sum_{j,\mathbf{q}} \frac{(\mathbf{k} \cdot \mathbf{c}^{(j,\mathbf{q})})^2}{2\omega_{j,\mathbf{q}}} \left[ \coth \left( \frac{\omega_{j,\mathbf{q}}}{2T} \right) (\cos \omega_{j,\mathbf{q}}t - 1) - i \sin \omega_{j,\mathbf{q}}t \right] \right\}
\end{aligned} \tag{2-174}$$

In 2-174  $\mathbf{q}$  is the propagation wave vector and  $j$  the branch index.

The distribution of  $\mathbf{q}$  values in the Brillouin zone is always sufficiently dense that the summation over  $\mathbf{q}$  can be replaced by an integral as follows:

$$\sum_{j,\mathbf{q}} \frac{(\mathbf{k} \cdot \mathbf{c}^{(j,\mathbf{q})})^2}{2\omega_{j,\mathbf{q}}} \dots \rightarrow \sum_{j=1}^3 \frac{1}{2} \int_0^{\infty} \frac{d\omega}{\omega} \overline{(\mathbf{k} \cdot \mathbf{c}^{(j)})^2} g_j(\omega) \dots \tag{2-175}$$

where it's clear that  $g_j(\omega) \equiv \int d^3q \delta[\omega - \omega_j(\mathbf{q})]$  and where  $\overline{(\mathbf{k} \cdot \mathbf{c}^{(j)})^2}$  is the average of  $(\mathbf{k} \cdot \mathbf{c}^{(j,\mathbf{q})})^2$  over a surface in  $\mathbf{q}$  space such that  $\omega$  is constant.

Rigorously for a cubic lattice and to a fair approximation for other lattices:

$$\overline{(\mathbf{k} \cdot \mathbf{c}^{(j)})^2} = \frac{1}{3} \kappa^2 \tag{2-176}$$

If we define  $g(\omega) \equiv \frac{1}{3} \sum_{j=1}^3 g_j(\omega)$  then we can write:

$$\begin{aligned}
\langle \chi_s \rangle_T &= \exp \left\{ - \frac{\kappa^2}{2} \int_0^{\infty} d\omega \frac{g(\omega)}{\omega} \left[ \coth \left( \frac{\omega}{2T} \right) (1 - \cos \omega t) + i \sin \omega t \right] \right\} \equiv \\
&\equiv \exp \left[ - \kappa^2 \gamma(t) / 2 \right]
\end{aligned} \tag{2-177}$$

### 2.3.3 Gaussian approximation and the generalized frequency distribution

A simple approach to practically calculate  $G_s(\mathbf{r},t)$  is to approximate it with  $G_s^c(\mathbf{r},t)$ .

Effectively, for some important (classical) dynamics models like the **free gas**, the **harmonic oscillator** and the **diffusion** an analytic expression may be found for  $G_s^c(\mathbf{r},t)$  and  $S^{\text{inc},c}(\mathbf{k},\omega)$ .

Moreover, the  $G_s^c(\mathbf{r},t)$  and  $\chi_s^c(\mathbf{k},t)$  functions of these systems turn out to have the same formal structure:

$$G_s^c(\mathbf{r}, t) = [2\pi W(t)]^{-3/2} \exp[-r^2/2W(t)] \quad 2-178$$

$$\langle \chi_s^c(\boldsymbol{\kappa}, t) \rangle_T = \exp[-\boldsymbol{\kappa}^2 W(t)/2] \quad 2-179$$

where  $W(t)$  is called “width” function and depends on the model<sup>6</sup>.

One finds that  $W(t)$  is simply the mean-square displacement of the particle during a time interval  $t$ , that is,

$$W(t) = \frac{1}{3} \langle [\mathbf{R}(t) - \mathbf{R}(0)]^2 \rangle \quad 2-180$$

Notice the Gaussian dependence on  $\mathbf{r}$  of  $G_s^c$ .

The Gaussian representation of  $G_s^c(\mathbf{r}, t)$  is particularly well suited to the discussion of neutron scattering by liquids. Although in general there is no reason to believe that  $G_s^c$  always has a Gaussian spatial distribution, the fact that models describing very different types of motion all show this behaviour strongly suggests that such an assumption should be a very good approximation even for liquids. Non-Gaussian corrections in liquids and gases have been studied: the effects are generally quite small. In practice, formula 2-178 is widely used in the analysis of all incoherent spectra. Once the Gaussian assumption is made, the problem reduces to the determination of an appropriate  $W(t)$ .

Suppose we apply the Gaussian approximation to the quantum-mechanical incoherent-scattering law

$$S_s(\boldsymbol{\kappa}, \omega) = \frac{1}{2\pi} \int_{-\infty}^{\infty} dt \exp(-i\omega t) \exp\left[-\frac{1}{2} \boldsymbol{\kappa}^2 \gamma(t)\right] \quad 2-181$$

where  $\gamma(t)$  is a complex width function yet to be specified.

We define  $S^2(\boldsymbol{\kappa}, \omega)$ :

$$S'(\boldsymbol{\kappa}, \omega) \equiv \exp(-\hbar\omega/2k_b T) S_s(\boldsymbol{\kappa}, \omega) \quad 2-182$$

If we put:

$$S'(\boldsymbol{\kappa}, \omega) = \frac{1}{2\pi} \int_{-\infty}^{\infty} dt \exp(-i\omega t) \exp\left[-\frac{1}{2} \boldsymbol{\kappa}^2 \gamma'(t)\right] \quad 2-183$$

then according to the properties of the Fourier transform it must be:

$$\gamma'(t) = \gamma(t + i\hbar/2k_b T) \quad 2-184$$

---

<sup>6</sup> In particular, it results:  $W(t) = 1/2(v_0 t)^2$  for gas,  $W(t) = (v_0/\omega_0)^2(1 - \cos\omega_0 t)$  for the oscillator,  $W(t) = 2Dt$  for the diffusing atom.

with  $\gamma'(t)$  a real and even function.

Through some mathematical steps it can be proven that  $\gamma'(t)$  is bound to the velocity autocorrelation function by the differential relation:

$$\frac{d^2 \gamma'(t)}{dt^2} = 8 \langle v(t)v(0) \rangle \quad 2-185$$

We define a function  $p(\omega)$  as follows:

$$\frac{d^2 \gamma'(t)}{dt^2} \equiv \int_{-\infty}^{\infty} dt \exp(i\omega t) p(\omega) = 2 \int_0^{\infty} dt \cos \omega t p(\omega) \quad 2-186$$

Integrating<sup>7</sup> 2-186 one obtains the relationship between  $\gamma'(t)$  and  $p(\omega)$ :

$$\gamma'(t) = 2 \int_0^{\infty} dt \frac{p(\omega)}{\omega^2} [\cosh(\hbar\omega/2k_b T) - \cos \omega t] \quad 2-187$$

Reminding 2-184 we obtain the relationship between  $\gamma(t)$  and  $p(\omega)$ :

$$\gamma(t) = 2 \int_0^{\infty} dt \frac{p(\omega)}{\omega^2} \left[ \cosh\left(\frac{\hbar\omega}{2k_b T}\right) - \cos \omega t \cosh\left(\frac{\hbar\omega}{2k_b T}\right) + i \sin \omega t \sinh\left(\frac{\hbar\omega}{2k_b T}\right) \right] \quad 2-188$$

If we introduce a function  $g(\omega)$  such that

$$g(\omega) \equiv \frac{2M}{\hbar\omega} \sinh\left(\frac{\hbar\omega}{2k_b T}\right) p(\omega) \quad 2-189$$

then

$$\gamma(t) = \frac{\hbar}{M} \int_0^{\infty} d\omega \frac{g(\omega)}{\omega} \left[ \coth\left(\frac{\hbar\omega}{2k_b T}\right) (1 - \cos \omega t) + i \sin \omega t \right] \quad 2-190$$

In conclusion we can say that in the Gaussian approximation the incoherent scattering law is 2-181, with  $\gamma(t)$  given by 2-190. The intermediate scattering function therefore is:

$$\langle \chi_s \rangle_T = \exp[-\kappa^2 \gamma(t)/2] \quad 2-191$$

2-181 and 2-190 have been obtained under very general assumptions, and apply for a monatomic system.

It can be proven [14] that

$$\frac{2M}{\hbar} \int_0^{\infty} d\omega \frac{p(\omega)}{\omega} \sinh\left(\frac{\hbar\omega}{2k_b T}\right) = 1 \quad 2-192$$

---

<sup>7</sup> The boundary conditions  $\gamma'(i\hbar/2k_b T) = 0$  and  $(d\gamma'/dt)(i\hbar/2k_b T) = i\hbar/M$  are applied. See [16], pag.34.

which implies that  $g(\omega)$  has a unit normalization.

2-177 has been obtained for a solid, and coincides with 2-190 and 2-191, with the distribution of lattice vibrational frequencies in 2-177 playing the same role as the homonymous  $g(\omega)$  in 2-190.

The function  $p(\omega)$ , whose relationship with  $g(\omega)$  is detailed in 2-189, is called “generalized frequency distribution”.

Conceptually, we infer that we can talk about phonons in any monatomic system for which we can apply the Gaussian approximation, even if the system is not a harmonic solid (for example a liquid). Actually we can say that the spectrum of lattice vibrational frequencies in harmonic solids is a particular case of the  $g(\omega)$  that can be introduced for any monatomic system, not only for crystals.

We remind that formula 2-176 applies rigorously only in case of cubic symmetry. Otherwise it can be shown that 2-176 still holds, provided that  $g(\omega)$  is replaced by a  $G(\omega)$ :

$$G(\omega) \equiv \frac{1}{3} \sum_{j=1}^3 \int d^3 q \left| \mathbf{c}^{(j,q)} \right|^2 \delta[\omega - \omega_j(\mathbf{q})] \quad 2-193$$

We now focus our attention on the atoms of hydrogen in the molecule of water, in the context of the Gaussian approximation.

We retain Nelkin’s assumption of dynamical independency of the 3 degrees of freedom: translation, rotation and vibration. So we can keep writing:

$$\langle \chi \rangle_T = \langle \chi^t \rangle_T \langle \chi^r \rangle_T \langle \chi^v \rangle_T \quad 2-194$$

As far as **liquid water** is concerned:

- **TRANSLATION:** Since there is at present no satisfactory theory of liquids, there is no definitive expression of  $\langle \chi^t \rangle_T$ . If we impose the Gaussian approximation then we need an appropriate mean-square displacement function  $W_T(t)$  or the velocity correlation function  $\langle v(t)v(0) \rangle$ . From measurements of the incoherent cross section and also from molecular-dynamics computer experiments, it’s been ascertained that at short times ( $t \leq 5 \times 10^{-13}$  sec) the motion of a liquid atom is oscillatory like that of a solid, while at long times ( $t \geq 2 \times 10^{-12}$  sec) the motion becomes diffusive. In order to represent these asymptotic behaviours an “artificial”  $W_T(t)$  can be:

$$\frac{1}{W_{T,liq}(t)} = \frac{1}{W_{cry}(t)} - \frac{1}{W_{cry}(\infty)} + \frac{1}{W_{cry}(\infty) + 2D \left[ t \left( t - \frac{i\hbar}{T} \right) \right]^{1/2}} \quad 2-195$$

So, for short times, we have  $W_{T,liq}(t)|_{t \rightarrow 0} \approx W_{cry}(t)$  and for large times we have  $W_{T,liq}(t)|_{t \rightarrow \infty} \approx W_{cry}(\infty) + 2D|t|$ , that is the desired asymptotic behaviours.

- **ROTATION:** Nelkin modelled the hindered rotations of the molecule in a liquid through a torsional harmonic oscillator, which automatically led to a Gaussian  $\langle \chi^r \rangle_{T,\Omega}$  (see 2.2.5). We found:

$$\begin{aligned}
 \langle \chi^r \rangle_{T,\Omega} &\approx \exp\left[\left(\frac{K^2}{m_r}\right)f(\omega_r, T, t)\right] = \\
 &= \exp\left\{\left(\frac{K^2}{2m_r}\right)\frac{1}{\omega_r}\left[\left(\frac{1}{e^{\omega_r/T}-1}+1\right)(e^{-i\omega_r t}-1)+\frac{1}{e^{\omega_r/T}-1}(e^{i\omega_r t}-1)\right]\right\} = \\
 &= \exp\left\{-\left(\frac{K^2}{2m_r}\right)\frac{1}{\omega_r}\left[\coth\left(\frac{\omega_r}{2T}\right)(1-\cos\omega_r t)+i\sin\omega_r t\right]\right\}
 \end{aligned} \tag{2-196}$$

which corresponds to the general expression of  $\gamma(t)$  seen in 2-190, with  $g_R(\omega) = \delta(\omega-\omega_r)$ , where  $\omega_r$  is the frequency of Nelkins's torsional oscillator.

- **VIBRATION:** The dynamics of the vibrations of the atoms in the molecule can be approximated as independent from the intermolecular interactions. The theory shown for solids in 2.3.2 applies exactly also for the hydrogen atoms in the molecule of water. Of course, in this case, the number of normal modes is only 3 and  $g_V(\omega) = \sum_{i=1}^3 \delta(\omega-\omega_i)$ . So we have a Gaussian  $\chi^v$ .

As far as **vapour** is concerned:

- **TRANSLATION:** It is free. As already seen in 2.2.4 and again mentioned in 2.2.5,  $\langle \chi^t \rangle_T$  for a free gas can be calculated without approximation and is Gaussian.
- **ROTATION:** It is free. It can be calculated without approximation and it is not Gaussian. Nevertheless: we impose the Gaussian approximation. In [14] Boutin and Yip show the analytical expressions of various rotational correlation functions (depending on the molecule's geometry) and comparisons between experimental results, theoretical predictions using exact quantum mechanical calculations and theoretical predictions imposing the Gaussian approximation: the three curves are always very close.
- **VIBRATION:** the same applies as for liquid water.

If  $\langle \chi^t \rangle_T$ ,  $\langle \chi^r \rangle_T$ ,  $\langle \chi^v \rangle_T$  are Gaussian then  $\langle \chi \rangle_T$ , which according to 2-194 is the product of them, will be Gaussian as well:

$$\begin{aligned}
 \langle \chi(\kappa, t) \rangle_T &= \langle \chi^t(\kappa, t) \rangle_T \langle \chi^r(\kappa, t) \rangle_T \langle \chi^v(\kappa, t) \rangle_T = \\
 &= \exp\left[-\frac{1}{2}\kappa^2\gamma_T(t)\right] \exp\left[-\frac{1}{2}\kappa^2\gamma_R(t)\right] \exp\left[-\frac{1}{2}\kappa^2\gamma_V(t)\right] = \\
 &= \exp\left[-\frac{1}{2}\kappa^2\gamma(t)\right]
 \end{aligned} \tag{2-197}$$

where

$$\begin{aligned}
\gamma(t) &= \gamma_T(t) + \gamma_R(t) + \gamma_V(t) = \\
&= \frac{\hbar}{m} \int_0^\infty d\omega \frac{g_T(\omega) + \frac{m}{m_R} g_R(\omega) + \frac{m}{m_V} g_V(\omega)}{\omega} \left[ \coth\left(\frac{\hbar\omega}{2k_b T}\right) (1 - \cos \omega t) + i \sin \omega t \right]
\end{aligned} \tag{2-198}$$

given that  $m$  is the mass of the whole molecule,  $m/m_R$  and  $m/m_V$  are constants that can be adjusted.

Therefore we can say that a molecular system like liquid water or vapour is characterized by a  $G(\omega)$ :

$$G(\omega) \equiv g_T(\omega) + \frac{m}{m_R} g_R(\omega) + \frac{m}{m_V} g_V(\omega) \tag{2-199}$$

Nelkin uses  $m=18$ ,  $m_R=2.32$ ,  $m_V=1.95$ .

The thermal cross sections sets used for the simulations mentioned in this work were produced at the IKE (University of Stuttgart) according to the guidelines described by Bernnat et al. [15], who adopted the following values respectively for water as ice, liquid and vapour:  $m = 18$ ,  $m_R = 2.25$ ,  $m_V = 2$ .

Usually, the most relevant parts of the various  $g_x(\omega)$  lay in different ranges of the spectrum and don't overlap very much. Therefore, applying the Gaussian approximation and Nelkin's assumption it's possible to separately consider the three parts of  $G(\omega)$  and make comparisons between different fluids or between different sources of information for the same fluid confronting one "piece" (translation, rotation, vibration) of the  $G(\omega)$  at a time.

### **3 Which thermal cross sections for supercritical water ?**

As far as supercritical water is concerned, only very little experimental results are available, and their reliability is discussions worthy.

Nevertheless, in recent years, the attention for supercritical water has grown in the scientific community, thanks also to SW's properties that make it interesting for certain chemical processes.

It's in this context that some resources have been allocated to Molecular dynamics simulations of SW.

#### **3.1 Molecular Dynamics simulations**

A MD simulation consists in assuming appropriate potentials governing the single molecule's intramolecular forces and the intermolecular interactions and then simulating the dynamics of a certain number of molecules according to the forces generated by the proposed potentials.

Actually, fine MD simulations allow for the trimming of a number of parameters that can influence to a certain degree the results.

Not only is it well known that the intra- and intermolecular potentials are parameterized and the parameters trimmed in order to tie in with some reference experimental results, but also the atoms' effective charges and consequently the molecules' dipole moment can be subject to adjustment.

A work of this kind has been performed and the results published in 1999 by J. Martí [16], from the Universitat Politècnica de Catalunya, Barcelona, Spain.

Martí simulated the dynamics of 216 molecules of water in a reference state at room temperature and in 8 supercritical states at different temperatures and densities.

For the technical details of the work we refer the reader to Martí's original article.

In Table 3-1 the simulated thermodynamic states are reported.

Table 3-1: Marti's simulated thermodynamic states. According to Marti the implemented potentials should imply a critical point close to state 4.

State	Temperature [°K]	Density [g/cm3]
1	298	1,00
2	573	0,72
3	573	0,83
4	587	0,27
5	673	0,49
6	673	0,66
7	673	0,83
8	723	0,35
9	773	0,26
10	773	0,83
11	873	0,10

Although the simulation was governed by the laws of classical mechanics, a steady confirmation of the results' credibility came from the confrontation of some crucial physical quantities characterizing the fluid's structure with the corresponding quantities measured experimentally. For example, the radial distribution function gives the particle density at a point at distance  $r$  from an arbitrarily chosen particle.

Recalling the expression of the correlation function  $G(\mathbf{r},t)$ :

$$G(\mathbf{r},t) = \frac{1}{N} \left\langle \sum_{i,j=1}^N \int d\mathbf{r}' \delta(\mathbf{r} + \mathbf{R}_i - \mathbf{r}') \delta(\mathbf{r}' - \mathbf{R}_j(t)) \right\rangle_T \quad 3-1$$

for  $t = 0$   $\mathbf{R}_i$  (that is  $\mathbf{R}_i(0)$ ) and  $\mathbf{R}_j(0)$  commute, therefore we have:

$$G(\mathbf{r},0) = \frac{1}{N} \left\langle \sum_{i,j=1}^N \delta(\mathbf{r} + \mathbf{R}_i(0) - \mathbf{R}_j(0)) \right\rangle \quad 3-2$$

Separating out the diagonal terms of the sum, we obtain:

$$\begin{aligned} G_s(\mathbf{r},0) &= \delta(\mathbf{r}) \\ G(\mathbf{r},0) &= \delta(\mathbf{r}) + g(\mathbf{r}) \end{aligned} \quad 3-3$$

where

$$g(\mathbf{r}) = \frac{1}{N} \sum_{i \neq j=1}^N \langle \delta(\mathbf{r} + \mathbf{R}_i - \mathbf{R}_j) \rangle \quad 3-4$$

Therefore, for an isotropic medium:

$$g(r) = 4\pi r^2 g(\mathbf{r}) \quad 3-5$$

Figure 3-1 gives evidence of a good agreement.

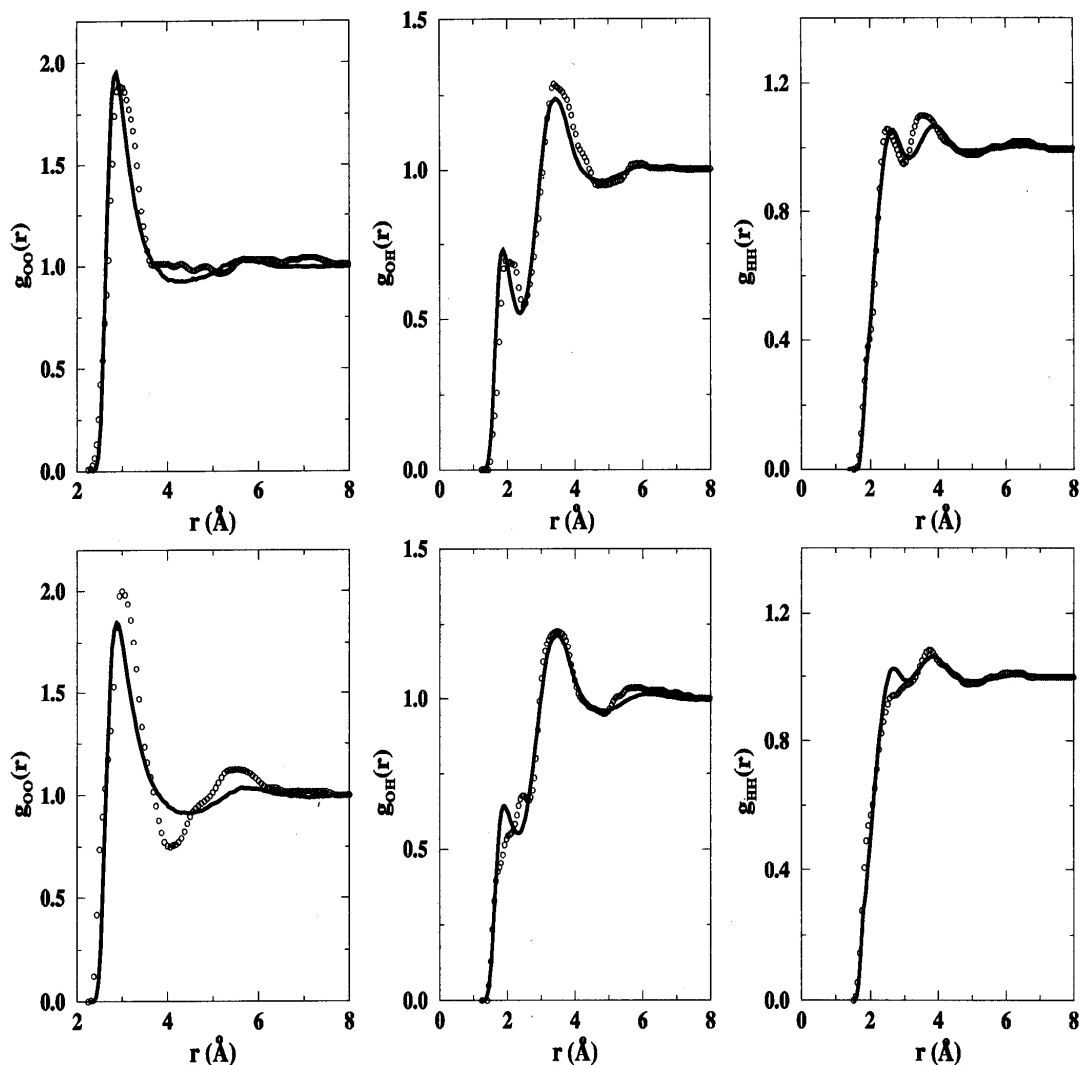


Figure 3-1: Radial distribution functions comparison. Experiment [17] (circles), Marti's MD simulation (continuous line). The top figures correspond to 573 °K and 0.72 g/cm<sup>3</sup> and the bottom figures correspond to 673 °K and 0.66 g/cm<sup>3</sup>.

Marti recorded the spectral density  $S_H$ , that is, the frequency distribution:

$$S_H(\omega) = \int_0^{\infty} dt \langle \mathbf{v}_H(t) \mathbf{v}_H(0) \rangle \cos \omega t$$

concerning libration (that is rotation), bending and stretching (see Figure 3-2) for every investigated thermodynamic state.

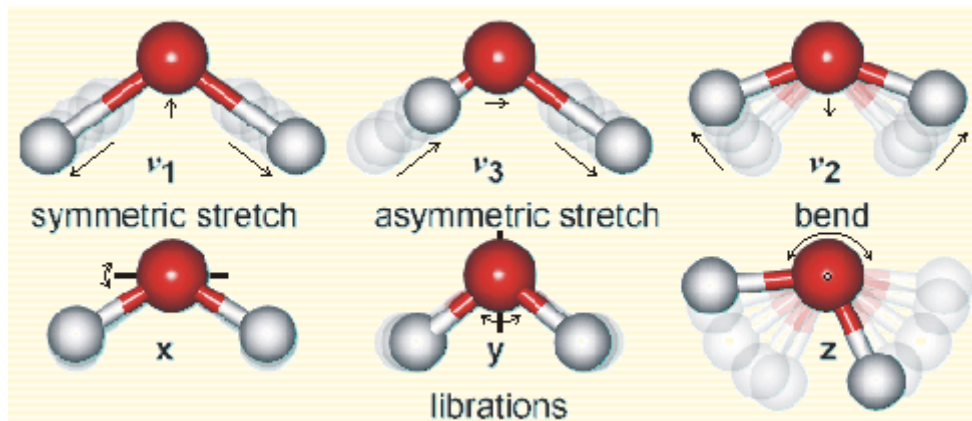


Figure 3-2: The top figures represent the movements associated to each normal mode of vibration of the Hydrogen atoms in the molecule of  $\text{H}_2\text{O}$ . The bottom figures represent the elementary rotation movements.

In particular, the frequency values of the peaks related to the above mentioned modes were reported in numerical format, so that it has been possible to confront them with the values assumed by Bernnat et al.[15] at IKE, who modelled the intramolecular oscillator spectrum as two temperature-independent harmonic Einstein  $\delta$ -oscillators, whose frequencies are reported in Table 3-2.

Table 3-2: Intramolecular oscillator frequencies of H bound in  $\text{H}_2\text{O}$  in meV, according to Bernnat et al.

[15]. Frequencies 1 and 3 refer to the stretching modes and are treated as one. Frequency 2 refers to bending.

oscillation	ice	liquid	vapor
$\omega_{1,3}$	409	436	460
$\omega_2$	203	205	198

In his article Martì stresses the point that the MD simulations' results are extremely sensible to the parameterization of the implemented potentials. In particular, he trimmed the parameters in order to make the stretching frequency of liquid water at ambient conditions (which, therefore, is assumed as reference state) tie in with the corresponding frequency obtained experimentally by Bertie et al. [18] through infrared experiences.

Therefore Martì states that it makes little sense to *directly* compare his simulations' results with other experimental results. One had better compare the libration, bending and stretching frequency peaks' **shifts from their position at the reference** (in this case, ambient) **thermodynamic state** obtained in his simulations with those obtained from other sources.

This is suggested as the best way to make comparisons independently from the parameterization (which, in turn, depends on the data available for the reference state).

As Marti chose liquid water at ambient condition as reference state to parameterize his potentials, it's clear that the peaks' frequency displacements (with respect to their positions at the reference state) registered by Marti must be applied to Bernnat's liquid water frequencies.

Table 3-3: The frequencies in the first row are Bernnat's frequencies for liquid. The frequencies in the following rows have been obtained adding the frequency displacements registered by Marti (with respect to Marti's values at room temperature) to the first row's frequencies. The uncertainties of the MD simulation values are about of 1% of each value.

State	~ Temperature [°C]	Density [g/cm3]	Libration [meV]	Bending [meV]	Stretching [meV]
1	25	1,00	70,0	205,0	436,0
2	300	0,72	45,2	193,2	452,1
3	300	0,83	48,9	194,5	447,2
4	314	0,27	34,0	189,5	457,7
5	400	0,49	35,9	188,9	454,6
6	400	0,66	41,5	192,6	452,1
7	400	0,83	40,9	191,4	450,3
8	450	0,35	35,3	188,3	457,7
9	500	0,26	35,3	185,8	456,5
10	500	0,83	40,9	192,0	449,0
11	600	0,10	36,5	174,6	467,0

### 3.2 Concrete recommendation

Bringing water to the supercritical state dramatically shifts the frequency peaks. The spectra available at IKE for liquid water (liquid water at ambient condition is the reference state upon which Table 3-3 has been compiled) can not be considered representative for water in super critical state, even allowing generous approximation margins.

Moreover, Table 3-3 shows evidence that the frequencies are extremely variable over the range of temperatures and densities typical of a HPLWR and therefore any **single** set of frequencies wouldn't suffice, as it was instead the case for normal water (Table 3-2).

All in all, considering the actual state of the art in this domain, the best thing to do is to use the thermal cross sections for vapour.

If anything, the IKE's vapour stretching frequency (460 meV, see Table 3-2) is much closer to the corresponding supercritical values than IKE's stretching frequency for liquid (436 meV), especially for intermediate and low densities.

IKE's vapour bending frequency seems not far from the supercritical values, at least as long as the densities are not too low, and in any case is closer than IKE's bending frequency for liquid.

If we consider Marti's states 2-7, which have values of temperature and density typical of the moderator in a HPLWR, then only the libration frequencies are definitely in disagreement with vapour's.

State 11's very low density is typical of a HPLWR's coolant in the superheaters. The bending frequency is far from IKE vapour's. On the other hand just because state 11's density is extremely low, the coolant shouldn't play a very important role as moderator there. Therefore, there exists the comfortable circumstance that where the vapour model is farthest from the reality of supercritical water, there is also its importance for the reactivity lower.

It also must be kept in count that certain thermo hydraulic parameters that influence the coolant's behaviour like, for example, the Nusselt number, are at present still subject to relevant uncertainties, which probably even outbalance those affecting supercritical water's thermalization properties.

More than this, according to the experience of the 2D simulations carried out on the old HPLWR's one-way design (with Bittermann's geometry, see 5.1), compensation phenomena that reduce the discrepancies arising from different thermal cross section sets arise along the burn-up.

## 4 Numerical tools used in the simulations

### 4.1 Neutron transport through Monte Carlo (MCNP)

The neutronic gas in the core can be effectively modelled as made of a large number of particles (neutrons) that do not interact with each other, travelling in the void according to classical mechanics laws and interacting with the nuclei according to probabilistic laws derived from the scattering theory of quantum physics.

The large number of particles, on the one hand, makes the system too complex to be modelled microscopically.

On the other hand, it constitutes the fundamental circumstance that holds up the introduction of models and techniques that make a macroscopic description of the core's behaviour possible.

In this context, one approach consists in following the philosophy of thermodynamics, defining a few directly measurable meaningful quantities (e.g. the flux), whose macroscopic measurement is not subject to statistical fluctuation, due to the slowness of the macroscopic measurements compared to the rapidity of the microscopic phenomena on atomic scale, so that one can always only gauge an „averaged“ (over time) value through the instruments.

It turns out that the behaviour of these quantities is governed by deterministic laws, and the diffusion theory is an example.

The second approach is sampling.

Sampling is an inference technique based on the Central Limit Theorem, which states that the expected value  $X_n$  of a random sample of  $n$  values extracted from a distribution having expected value  $\mu$  and finite variance  $\sigma^2$  is approximately distributed as a gaussian distribution having expected value  $\mu$  and variance  $\sigma^2/n$ .

The quantities of interest (flux, reaction rates) are inferred on the basis of the average behaviour of only a limited number of neutrons' stories, which are simulated one by one according to the above-mentioned physical laws.

The sampling of a limited number of stories makes the results subject to sensible statistical fluctuations, so that they can not be approximated as fully deterministic as in reality. Nevertheless, it's possible to fulfil any quality requirement as long as a sufficient number  $n$  of stories is simulated.

The simulation of a neutron's interactions with matter for the purposes of nuclear reactor physics is conceptually easy. The extension of the free path and the nature of every interaction are modelled through the extraction of random variables from appropriate probabilistic distributions (which are derived from the available cross sections).

Technically, given an algorithm that produces numbers in the interval (0,1) with uniform probabilistic distribution  $U$ , it's possible to sample from any continuous distribution  $F_x$ , in that the variable  $X = F_x^{-1}(U)$  has repartition function  $F_x()$ .

The Monte Carlo method consists in the implementation of such an algorithm and possibly the tallying of the simulated microscopic events corresponding to the macroscopic quantities of interest.

The limit of the first approach is that the deterministic laws governing the transport are described by differential equations. It's well known that the main difficulty in the solution of differential equations is the respect of the border conditions.

Modern engineering solutions employ heterogeneous systems having usually very limited symmetry properties, so that even the numerical solution of the 3D-problem results to be viable only upon some simplification of the geometry.

As long as strict statistical quality requirements are fulfilled, the Monte Carlo provides more precise and realistic solutions, without any or only with some minor geometry simplifications.

On the other hand, if the geometry is large (and this applies especially to 3D models), a large number of stories can be required in order the variances to be acceptably small. Algorithms that extract random numbers are usually not elaborate, but tracking every story and storing the outcome of every interaction can require relevant resources in terms of computational facilities and calculation time.

As resources are the main problem associated with this method, the approach to the investigations reported in this work and even the goals themselves have consciously been set down in order to be compatible with the available resources.

## 4.2 Depletion (ORIGEN2)

A general expression for the formation and disappearance of a nuclide by nuclear transmutation and radioactive decay may be written as follows:

$$\frac{dX_i}{dt} = \sum_{j=1}^N \ell_{ij} \lambda_j X_j + \bar{\Phi} \sum_{k=1}^N f_{ik} \sigma_k X_k - (\lambda_i + \bar{\Phi} \sigma_i) X_i \quad (i = 1, \dots, N) \quad 4-1$$

where  $X_i$  is the atom density of nuclide  $i$ ,  $\lambda_i$  is the radioactive disintegration constant for nuclide  $i$ ,  $\sigma_i$  is the spectrum-averaged neutron absorption cross section of nuclide  $i$ , and  $\ell_{ij}$  and  $f_{ik}$  are the fractions of radioactive disintegration and neutron absorption by other nuclides which lead to the formation of species  $i$ .  $\bar{\Phi}$  is the position- and energy-averaged neutron flux.

Rigorously, the system of equations described by 4-1 is nonlinear since the neutron flux and cross sections will vary with changes in the composition of the fuel. However, these variations with time are slow and, if they are considered to be constant over short time intervals, 4-1 is a homogeneous set of simultaneous first-order ordinary differential equations with constant coefficients, which may be written in matrix notation as

$$\dot{\mathbf{X}} = \mathbf{A}\mathbf{X} \quad 4-2$$

where  $\mathbf{A}$  is called “transition matrix”. 4-2 has the known solution:

$$\mathbf{X}(t) = \exp(\mathbf{A}t)\mathbf{X}(0) \quad 4-3$$

where  $\mathbf{X}(0)$  is a vector of initial atom densities and  $\exp(\mathbf{A}t)$  is called “matrix exponential function”.

From the computational point of view, the storage of the transition matrix and of the matrix exponential function and the computation of the matrix exponential method can be problematic.

ORIGEN2’s developers have facilitated the computation and storage of the matrix exponential function by developing a recursion relation for this function which doesn’t require storage of the entire matrix. For the  $i$ -th nuclide the evolution of its atom density will be given by:

$$x_i(t) = \sum_{n=0}^{\infty} C_i^n \quad 4-4$$

where  $C_i^n$  is generated by use of a recursion relation:

$$\begin{aligned} C_i^0 &= x_i(0) \\ C_i^{n+1} &= \frac{t}{n+1} \sum_{j=1}^N a_{ij} C_j^n \end{aligned} \quad 4-5$$

Here,  $a_{ij}$  is an element in the transition matrix that is the first-order rate constant for the formation of species  $i$  from species  $j$ . This algorithm requires storage of only one vector  $\mathbf{C}$  in addition to the current value of the solution.

As the transition matrix is typically very sparse, in ORIGEN2 only the  $a_{ij} \neq 0$  are stored in a linear vector.

Three additional vectors are employed to:

- locate the elements  $a_{ij}$
- store the identity of the  $i$ -th element (daughter)
- store the identity of the  $j$ -th element (parent)

These few vectors don't contain any "empty" cell (that is,  $a_{ij} = 0$  and similar), and so the usage of the computer's storage capacity is optimised.

In order to fill some of these vectors, two data matrices are used, which for every couple [parent, reaction] contain respectively:

- the reference to the daughter's identity
- the first-order rate constant for the corresponding transition

Although the possible parents are many, the number of possible reactions leading to any daughter are not, therefore the storage of these matrices is not very expensive. It must be kept in count that ORIGEN2 can compute the concentrations of as many as 1700 nuclides. A whole transition matrix would contain 1700 x 1700 elements!

In performing the summation indicated by 4-5, it is necessary to ensure that precision in the answer will not be lost due to the addition and subtraction of nearly equal large numbers.

Thus in the computations performed by ORIGEN2, only the compositions of those nuclides whose diagonal matrix elements are less than a predetermined value are computed by the matrix exponential method.

If  $A \rightarrow B \rightarrow C$  and if the decay constant for B is large, the matrix is reformulated as if C were formed from A directly, so that the concentration of A is calculated through the matrix exponential method, whereas the concentration of B, assumed to be in secular equilibrium with its parent at the end of any time interval, is obtained solving the following set of linear algebraic equations:

$$\dot{\mathbf{X}} = \mathbf{A}\mathbf{X} = 0 \quad 4-6$$

that is

$$\dot{x}_i = 0 = \sum_{j=1}^N a_{ij} x_j \quad 4-7$$

whose solution doesn't involve particular computational problems.

Similarly, if the decay constant for A is very large, the transition matrix is rewritten as if the amount of isotope B initially present were equal to A+B, and only the transition

B→C is obtained applying the matrix exponential technique, whereas the quantity of A that remains at the end of the interval is computed analytically.

At the start of the computation, the known parameters are the initial fuel composition, the constant specific power that the fuel must produce during a time interval and the length of the time interval.

The instantaneous neutron flux is related to the constant specific power at a fixed time by the formula

$$P = 1.602 \times 10^{-19} \Phi(t) \sum_i x_i(t) \sigma_i^f R_i \equiv 1.602 \times 10^{-19} \Phi(t) S(t) \quad 4-8$$

where P is the specific power, in MW per unit of fuel;  $x_i$  is the amount of fissile nuclide i present in the fuel in g-atoms per unit of fuel;  $\sigma_i^f$  is the microscopic fission cross section for nuclide i;  $\Phi$  is the instantaneous neutron flux, in neutrons  $\text{cm}^{-2} \text{s}^{-1}$ ;  $R_i$  is the recoverable energy per fission for nuclide i, in MeV/fission. The constant in 4-8 converts MeV/sec into megawatts.

Therefore:

$$\Phi(t) = \frac{P}{1.602 \times 10^{-19} S(t)} = 6.242 \times 10^{18} P \frac{1}{S(t)} \quad 4-9$$

$S(0)$  at the start of the interval is known. Moreover:

$$\begin{aligned} \dot{\mathbf{X}}(0) &= A\mathbf{X}(0) \\ \ddot{\mathbf{X}}(0) &= A\dot{\mathbf{X}}(0) \end{aligned} \quad 4-10$$

and so on. That is  $\dot{x}_i(0)$ ,  $\ddot{x}_i(0)$ ... and therefore  $\dot{S}(0)$ ,  $\ddot{S}(0)$ ... are known.

So it is possible to find an approximate expression for  $1/S(t)$  for small t, and hence for  $\Phi(t)$ :

$$\begin{aligned} \Phi(t) &= 6.242 \times 10^{18} P \left[ \frac{1}{S(0)} - t \frac{\dot{S}(0)}{S^2(0)} + \frac{t^2}{2} \frac{2\dot{S}(0)\dot{S}(0) - \ddot{S}(0)S(0)}{S^3(0)} + \dots \right] = \\ &= \Phi(0) \left[ 1 - t \frac{\dot{S}(0)}{S(0)} + \frac{t^2}{2} \frac{2\dot{S}(0)\dot{S}(0) - \ddot{S}(0)S(0)}{S^2(0)} + \dots \right] \end{aligned} \quad 4-11$$

The average neutron flux during the interval is obtained by integrating over the interval and dividing by the length of the interval t:

$$\bar{\Phi} = \Phi(0) \left[ 1 - \frac{t}{2} \frac{\dot{S}(0)}{S(0)} + \frac{t^2}{6} \frac{2\dot{S}(0)\dot{S}(0) - \ddot{S}(0)S(0)}{S^2(0)} + \dots \right] \quad 4-12$$

Analogously, the average power produced during a time interval for the fuel in a fixed neutron flux can be estimated from the initial composition:

$$\bar{P} = 1.602 \times 10^{-19} \Phi S(0) \left[ 1 + \frac{t}{2} \dot{S}(0) + \frac{t^2}{6} \ddot{S}(0) + \dots \right] \quad 4-13$$

### 4.3 Thermo hydraulics (STAFAS)

The geometrical arrangement of the fuel rods in heterogeneous fuel elements usually doesn't enjoy a fully translational symmetry, because the neighbourhood of each fuel rod is geometrically different. Therefore, in general, the coolant's temperature and density distributions don't enjoy translational symmetry either and one must expect exchanges of heat and mass between different areas of the coolant's conduit.

Modern thermo hydraulic software packages address this point modelling the coolant's conduit not only as subdivided in transversal slices, but also in axial sub channels, so that a 3D mesh is applied, generating a net of small 3D volumes, as depicted in Figure 4-1.

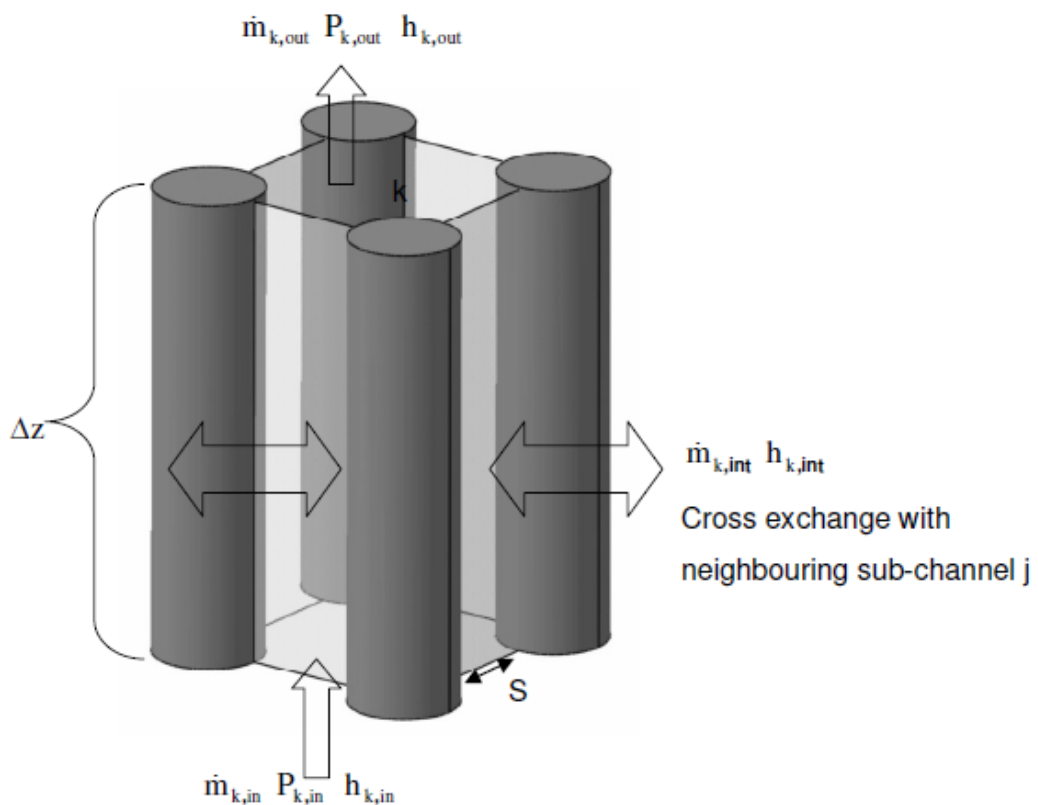


Figure 4-1: Coolant's sub channel 3D volume element.

The continuity, axial momentum and energy equations are applied to each generated 3D element.

The continuity equation foresees transverse mass flow entering the volume cell through the interfaces to adjacent sub-channels due to turbulent mass interchange and transverse pressure gradients.

The axial momentum equation foresees inter-channel momentum exchange due to the same two above-mentioned phenomena, and the same applies for the energy equation.

An essential issue in the context of the fuel element design is the localization of possible hot spots arising in the cladding. A precise and reliable prediction of the cladding temperature distribution requires an as good knowledge of the heat transfer coefficient.

A thorough literature review on heat transfer under supercritical conditions has been carried out by Cheng and Schulenberg [3]. It has been pointed out that the experimental works available in the open literature are mainly restricted to a circular tube geometry.

In any case, large deviations were obtained between the Dittus-Boelter equation, using the bulk temperature and the wall temperature, and the test data near the pseudo-critical temperature. Figure 4-2 compares the heat transfer coefficients calculated using different correlations revealing these large discrepancies.

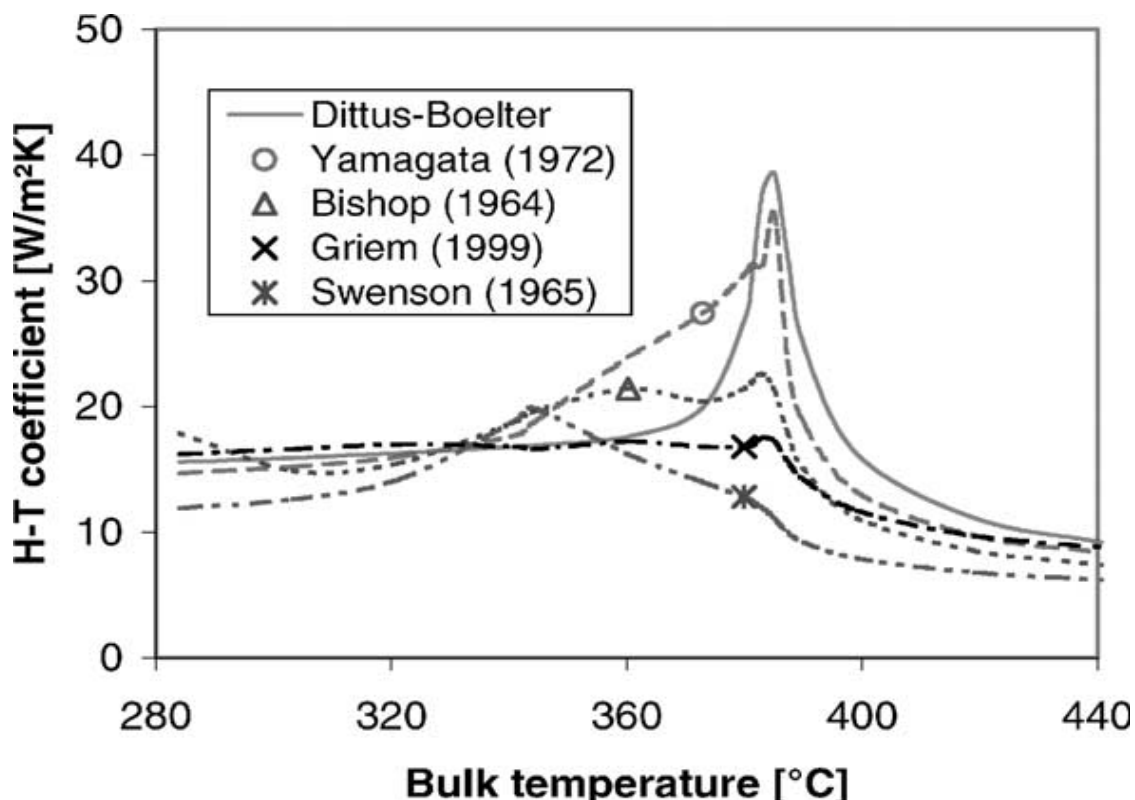


Figure 4-2: Heat transfer coefficient according to different correlations ( $P = 25$  MPa,  $G = 1000$  kg/m<sup>2</sup> s,  $q = 1E+06$  W/m<sup>2</sup>).

The Bishop correlation:

$$Nu_B = 0.0069 Re_B^{0.90} \cdot Pr_B^{0.66} \cdot \left( \frac{\rho_{wall}}{\rho_B} \right)^{0.43} \cdot \left( 1 + \frac{2.4D_h}{z} \right) \quad 4-14$$

was implemented in STAFAS [5] upon recommendation in Cheng and Schulenberg's above mentioned report.

In 4-14  $Re_B$  and  $Pr_B$  refer to the bulk dynamic viscosity and bulk thermal conductivity.

$Pr_B$  refers to the average specific heat  $\bar{C}_p$ , defined as:

$$\bar{C}_p \equiv \frac{h_{wall} - h_B}{T_{wall} - T_B} \quad 4-15$$

where  $h_{wall}$  and  $h_B$  are the wall and bulk enthalpies;  $T_{wall}$  and  $T_B$  are the wall and bulk temperatures.

The other parameters featured in 4-14 are:

$\rho_{wall} / \rho_B$  = fluid density at the wall / bulk

$D_h$  = hydraulic diameter

$z$  = axial height

## 4.4 Burn-up simulation of 2D-geometries

### 4.4.1 Draft model of the process

The problem of burn-up simulations is that depletion programs usually work on the basis of multi- or one-group cross sections. These depend on the spectrum and the spectrum, in turn, on the fuel composition, which undergoes gradual change along the burn-up.

The irradiation time must therefore be subdivided in smaller periods, during which the spectrum is assumed to be constant and the depletion be simulated through a succession of runs, each using updated cross-sections.

The spectrum can be obtained only by a transport code: at every step, the transport code determines the power, the relevant reaction rates and the flux for each energy interval of the spectrum featured by the depletion software, according to the present fuel composition. The power and the derived cross sections must be input in the depletion code. The updated composition at the end of the burn-up period must be input in the transport code and so on.

Therefore the burn-up simulation is a cyclical process: a transport and a depletion codes must be coupled.

The software of choice to simulate the fuel's irradiation and depletion is ORIGEN.

ORIGEN is a point-depletion code disposing of one-group cross-sections libraries.

The geometrical representation of the fuel in MCNP must therefore be subdivided in burn-up zones, in which the fuel composition and the flux's spectrum and magnitude are considered approximately constant.

Flux and reaction rates are therefore separately tallied in each zone, and the corresponding cross sections are calculated.

At every burn-up step ORIGEN must be run once for each fuel zone, using the corresponding cross sections in order to update its composition.

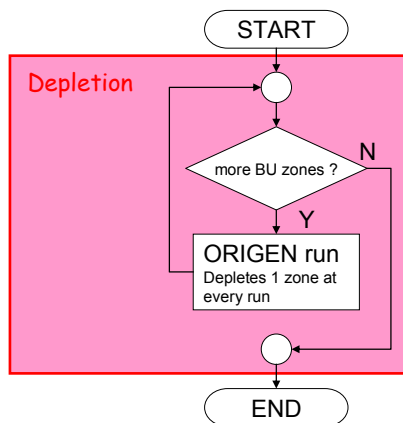


Figure 4-3: As ORIGEN is a point-depletion code, it must be run once for each BU zone.

#### 4.4.2 Handling of the implementation's practical difficulties

The coupling software features some simplifications with respect to the general scheme presented in the previous paragraph, in order to cope with two fundamental problems:

- 1) MCNP and ORIGEN were not developed to be compatible with each other
- 2) The Monte Carlo is high resource-consuming

ORIGEN can be input either with the zone's flux or with the zone's power.

In a first version of the coupling software, ORIGEN has been fed with the thermal power, because during the burn-up interval ORIGEN adjusts the irradiating flux according to the evolving fuel's composition, remaining loyal to the set thermal power.

On the other hand, MCNP doesn't feature any tally recording the developed thermal power. The best choice appeared at that time to use the tally F7.

The tally F7 registers the power (averaged over the cell) coming only from fission, considering the fission's photons deposited locally.

This means that beta decay, delayed gamma and gamma from capture are not included.

Although the missing energy is relevant, the F7 tally just returns a normalized power value for each burn-up zone, which is not directly used as thermal power.

The coupling software renormalizes the F7 values' distribution to the given total thermal power of the system before feeding ORIGEN with it. This means that, although the total power considered for the burn-up is the right, given (fixed a priori) thermal power, its geometrical distribution used in the simulation is not the real geometrical distribution of the thermal power. Actually, ORIGEN is fed with the right total thermal power, but distributed as (that is, having the shape of) the prompt fission power.

The system later has been improved (see 4.5.2).

In order to appropriately keep in count the Doppler Effect it is crucial, for a same nuclide, to use a cross section set suitably prepared for the given fuel temperature.

Actually, data sets are usually available only for a discrete set of fixed temperatures distributed all over the foreseen fuel temperature range (Figure 4-4).

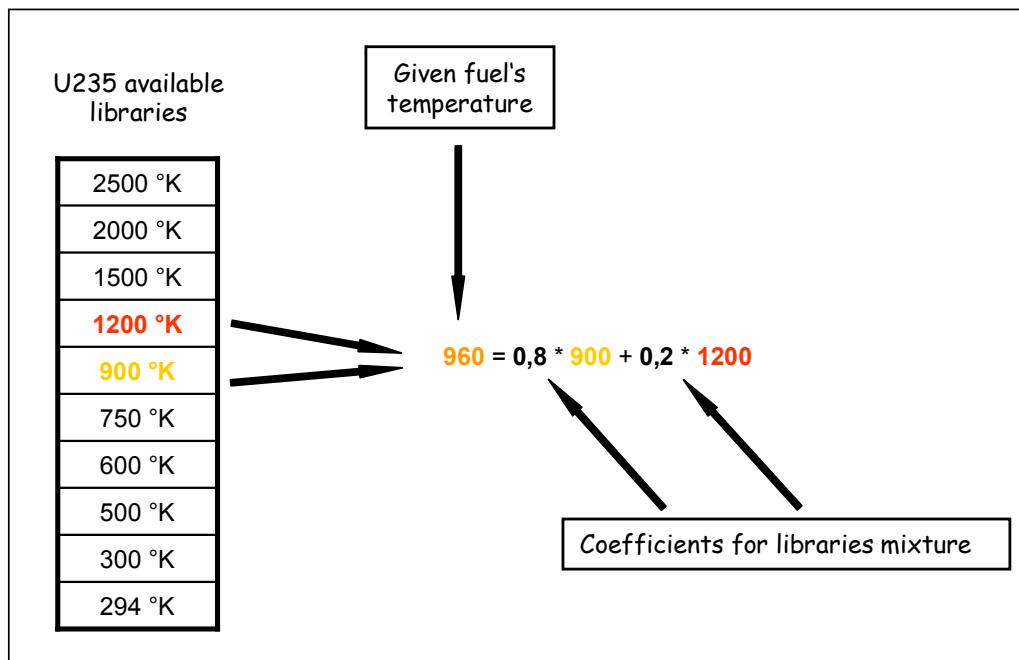


Figure 4-4: As shown in the example, the actual fuel temperature falls in any case between two available libraries temperatures. The same derived coefficients can be used to weigh the reaction rates tallied with the two libraries in order to estimate the reaction rate for the given fuel temperature.

In order to realistically sample the neutrons' lethargy step by a collision, a ruse was applied to effectively represent and update each fuel zone's composition: in the material card corresponding to a certain fuel zone, each nuclide's atomic fraction is split up into two components, referring to the available libraries having temperature closest (higher and lower) to the fuel zone's.

The total atomic fraction is partitioned among the two components according to the proximity of their temperature to the fuel zone's as schematised in Figure 4-4.

ORIGEN disposes of a cross section library for numerous reactions referring to 130 actinides, 850 fission products (+720 activation products, not relevant for our purposes).

For the sake of resources only the fission and capture rates of 21 actinides and the capture rates of 78 fission products are tallied with MCNP in each burn-up zone.

These nuclides are selected on the basis of their relevant cross section's sensibility to the spectrum (actinides) and expected abundance in the burnt fuel (actinides and fission products).

Additional 26 actinides and 115 fission products, seen as less important, are taken into consideration, but in another, less expensive way: the fuel zones are subdivided in a few fuel zones groups, so that in the zones belonging to a same group the spectrum is assumed to be very similar.

Then a preliminary MCNP run is executed for fresh fuel, tallying the reaction rates of these "minor" nuclides and the flux in every zones group (averaged over the whole of the group) and in every one of  $\sim 70$  energy bins covering the energy range from 0 to 19.64 MeV.

Dividing every reaction rate by the corresponding flux (same zones group and same energy bin), multi-group cross sections sets are obtained for every zone group.

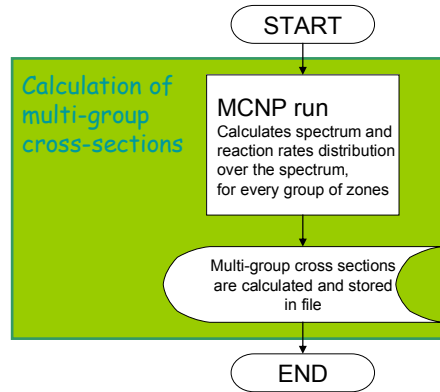


Figure 4-5: The multi-group cross sections are calculated on the basis of a preliminary MCNP run carried out for fresh fuel, though the obtained cross sections are used throughout the burn-up simulation.

Later, at every burn-up step of the actual burn-up simulation, the updated flux spectrum was gauged in each fuel zone according to the same 70-group scheme. Weighing the multi-group cross sections obtained for fresh fuel (applying to every cell of a zones group) with the updated spectrum (zone by zone), one-group cross sections (zone by zone) were derived, to be replaced in ORIGEN's library.

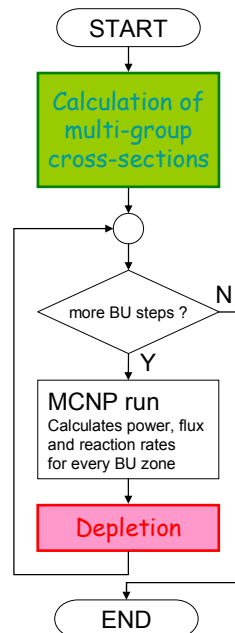


Figure 4-6: Complete flow-chart of the first version of the burn-up software.

## 4.5 Burn-up simulations of 3D geometries

The main virtue of a 3D simulation compared with a 2D one is the possibility to determine the correct axial power distribution, and therefore the corresponding moderator and coolant axial configurations.

But in order the results to be realistic, the thermal interaction between fuel and coolant should be taken into account, and this implies the coupling of a transport and a thermal-hydraulics codes.

STAFAS's developers subdivided the assembly in 21 axial layers and partitioned the coolant's cross section in 9 subchannels, as depicted in Figure 1-5.

As this model is hard-coded in STAFAS, Hofmeister's geometry was implemented in MCNP's input according to the same scheme.

The fuel and the coolant subchannels' thermodynamic states exert a mutual influence, partly directly (heat exchange) and partly indirectly (coolant's moderating role). Therefore, given the fuel's composition, the corresponding fuel's, coolant's and moderator's thermodynamic states must be found through a series of iterations, whereby MCNP and STAFAS are run alternatively, updating every time one's input with the other's output, until the convergence is achieved.

STAFAS's output data, which are all input into MCNP are:

- Temperature in everyone of 21 x 7 fuel zones
- Temperature, density in everyone of 21 x 9 coolant zones
- Temperature, density in everyone of 21 x 2 moderator zones

The MCNP's output data that are input into STAFAS are:

- Power (from tally F6) deposited in everyone of the 21 x 7 fuel zones

One-group cross sections are then calculated keeping in count the assembly's converged thermodynamic configuration.

As far as the preparation of multi-group cross sections for the minor nuclides is concerned, each of the 21 horizontal layers (each containing 7 fuel zones) has been considered as a zones group.

Therefore, the multi-group cross sections were prepared for every single layer through a specific, preliminary MCNP run for fresh fuel, only after having reached the convergence of the whole assembly's thermal-hydraulic state.

The multi-group cross sections relative to a certain layer were used for every fuel zone belonging to that layer, the same way as described in 4.4.2.

#### **4.5.1 Convergence criterion**

The iteration process's convergence can punctually be assessed selecting a subset of STAFAS's and MCNP's output data and verifying that the relative variation of every one of them between two successive iterations be smaller than a predefined margin.

Alternatively, a looser criterion can be followed, whereby only some aggregate quantities are monitored.

In view of the difficulties already experienced by Waata [5], 21 integral tests of the power collectively deposited in the fuel zones belonging to the same axial layer were initially adopted, setting the margin at 5 %.

In a first convergence test carried out for fresh fuel, starting from uniform moderator's and coolant's properties, the satisfaction of this condition required 13 iterations. Figure 4-7 shows that the profile obtained after 6 iterations is already extremely close to the 13<sup>th</sup> one, and that the profile never punctually converges; it actually is always subject to small oscillations.

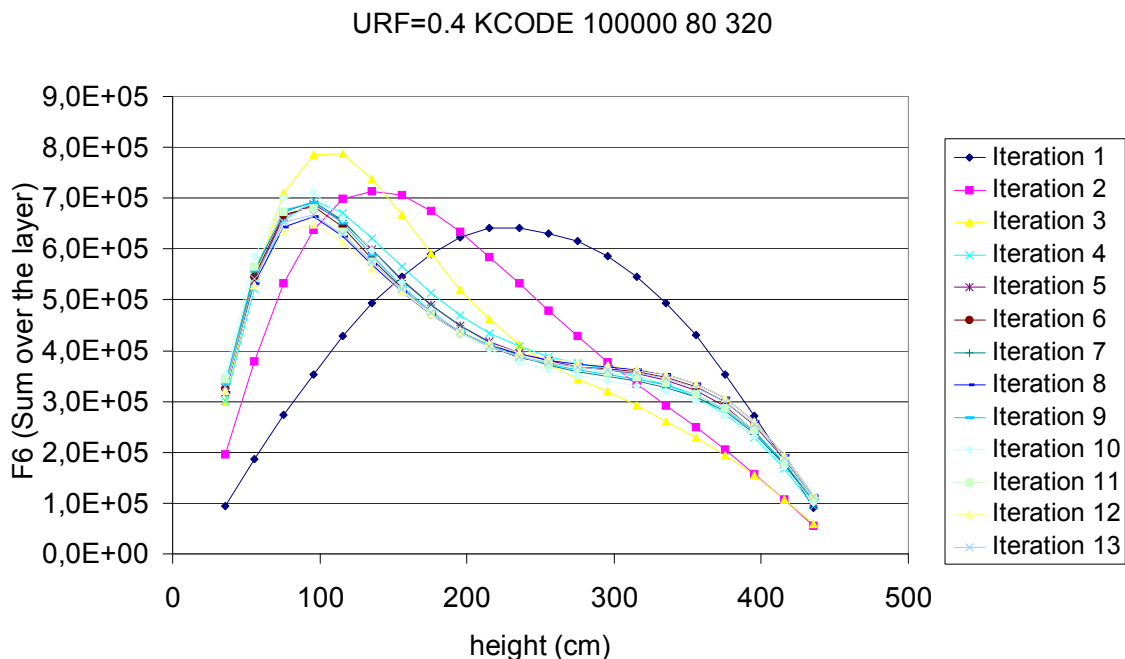


Figure 4-7: Power distribution profiles obtained through successive iterations for fresh fuel. The linear power is expressed in normalized units.

An analysis of the results in numerical form confirmed that these small oscillations delay the achievement of the convergence especially in the upper part of the assembly, where the power density is relatively small.

This raised some concern about the feasibility of the whole burn-up in reasonable time, and induced to set a weaker convergence criterion, so that the monitored quantities are the total power deposited respectively in the lower, in the middle and in the upper assembly's 7 layers. The margin was left at 5 %.

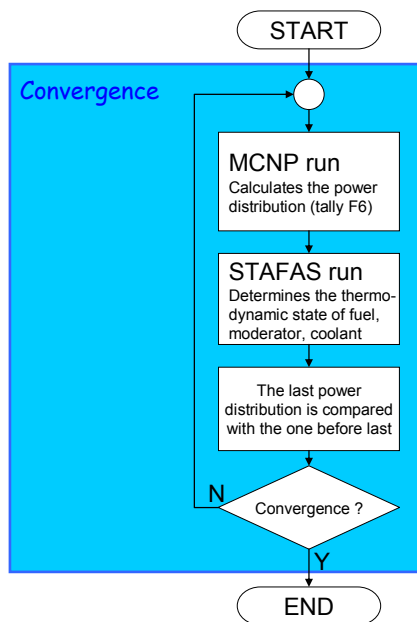


Figure 4-8: Flow-chart of the transport-thermo hydraulics convergence process.

#### 4.5.2 BU software's upgrade and fitting for the coupling with STAFAS

The MCNP-ORIGEN coupling software has been updated with two goals in mind:

1. Enhancing the quality of the existing software
2. Making the existing software suitable to be coupled with STAFAS

##### Quality enhancement of the existing burn-up software

It will be recalled that the system used to execute the first simulations, worked imposing the thermal power to each fuel zone according to a distribution that actually is the distribution of the prompt recoverable power (found using the tally F7).

As the main virtue of a 3D simulation compared with a 2D one is the possibility to determine the correct axial power repartition (and therefore the corresponding moderator and coolant axial configurations), the spur was felt to perfect the method that detects the thermal power distribution.

The new procedure works as follows:

1. The MCNP reaction rates' run at the beginning of the burn-up step provides the geometrical (normalised) flux distribution all over the fuel zones.
2. ORIGEN is run once for every fuel zone with MCNP's tallied flux as input, simulating a negligible time interval (1 sec.). As the input is the fuel zone's tallied normalized flux, ORIGEN's output is the corresponding normalized thermal power. At the

end of this first round of ORIGEN runs, a normalized distribution of the thermal power is obtained.

3. The thermal power distribution is estimated fitting (that is, renormalizing) the normalised thermal power distribution to the real assigned assembly's thermal power.

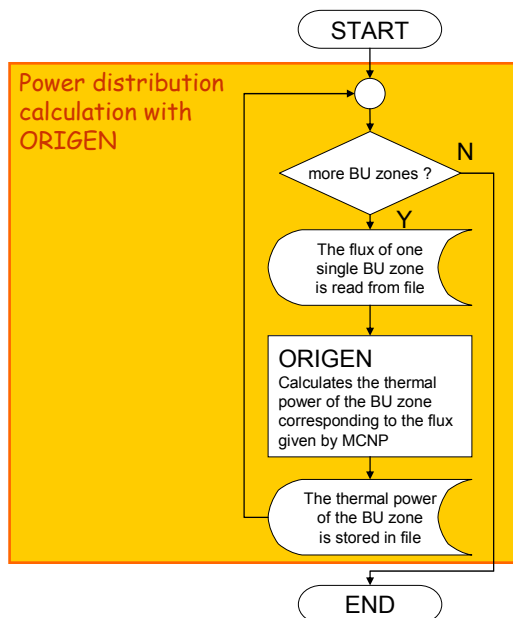


Figure 4-9: Flow-chart of the refined power distribution determination system.

A second round of ORIGEN runs simulates the burn-up of every fuel zone (as usual) on the basis of the real thermal power distribution.

### Fitting of the burn-up software for temperatures management

The coupling of MCNP with STAFAS could in principle be considered independent from the existing coupling with ORIGEN.

But it will be recalled from 4.4.2 that the presence of a nuclide in a fuel zone is represented as an appropriate mixture of two libraries referring to the same nuclide, having different temperatures. As the fuel zones' temperatures must be updated at every iteration with STAFAS, a software module was worked into the system in order to automatically update the mixture proportions after every iteration.

Moreover, the reaction rates must be tallied using data sets referring to the temperature of the fuel zones where the reactions take place.

As the fuel zones' temperatures are updated at every iteration with STAFAS, the used cross sections should accordingly be updated as well. It is for this reason that the reaction rates according to each of the available temperatures were systematically tallied in

every fuel zone, for every nuclide, so that the temperature of each fuel zone always fell between two available data sets' temperatures (the same way as described for the representation of the fuel composition in 4.4.2).

The software coupling MCNP with ORIGEN was updated so that a particular reaction rate in a certain fuel zone was calculated as the average of the reaction rates corresponding to the two closest available data sets' temperatures, weighed accordingly to their proximity to the fuel's.

For many of the 240 nuclides employed (especially the most irrelevant fission products) only one library was available.

Nonetheless, the representation of many nuclides in MCNP's input through 2 libraries has further fragmented the formal composition of the fuel zones contributing to longer execution times.

The necessity to tally the reaction rates of the most relevant nuclides for every available temperature (usually ~10), forced a reduction of the tallied nuclides to the only 10 shown in Table 4-1 and Table 4-2.

Table 4-1: Actinides for which the reaction rates were tallied at every burn-up step.

<b>Nuclide (Actinides)</b>	<b>N. of available (li- braries') temp.</b>
U <sup>235</sup>	10
U <sup>238</sup>	10
Np <sup>239</sup>	1
Pu <sup>239</sup>	10
Pu <sup>240</sup>	10
Pu <sup>241</sup>	10

Table 4-2: Fission products for which the reaction rates were tallied at every burn-up step.

<b>Nuclide (Fiss. products)</b>	<b>N. of available (libraries') temp.</b>
$I^{135}$	1
$Xe^{135}$	1
$Pm^{149}$	1
$Sm^{149}$	1

$Np^{239}$  was included in the shortlist as it is present in the decay chain starting after the capture of a neutron by  $U^{238}$  and leading to the formation of  $Pu^{239}$ .

Although a number of libraries were available also for  $Np^{239}$ , as its cross sections are smooth, reaction rates have always been tallied only for a fixed, preset temperature of 1184 °K. This value is the fresh fuel's mean temperature and was determined in a preliminary test.

In reference to Table 4-2,  $I^{135}$  is  $Xe^{135}$ 's parent in a decay chain starting from the fission product  $Te^{135}$  and  $Pm^{149}$  is  $Sm^{149}$ 's parent in a decay chain starting from the fission product  $Nd^{149}$ .

$Te^{135}$  and  $Nd^{149}$  were not included seen the short half-life.

The remaining nuclides joined the large group for which multi-group cross sections are calculated for fresh fuel and used throughout the burn-up, as described in 4.4.2.

However, also each of the nuclides belonging to this group was represented by an appropriate mixture of two libraries, whose weight was trimmed in order the resulting average to match the temperature of 1184 °K.

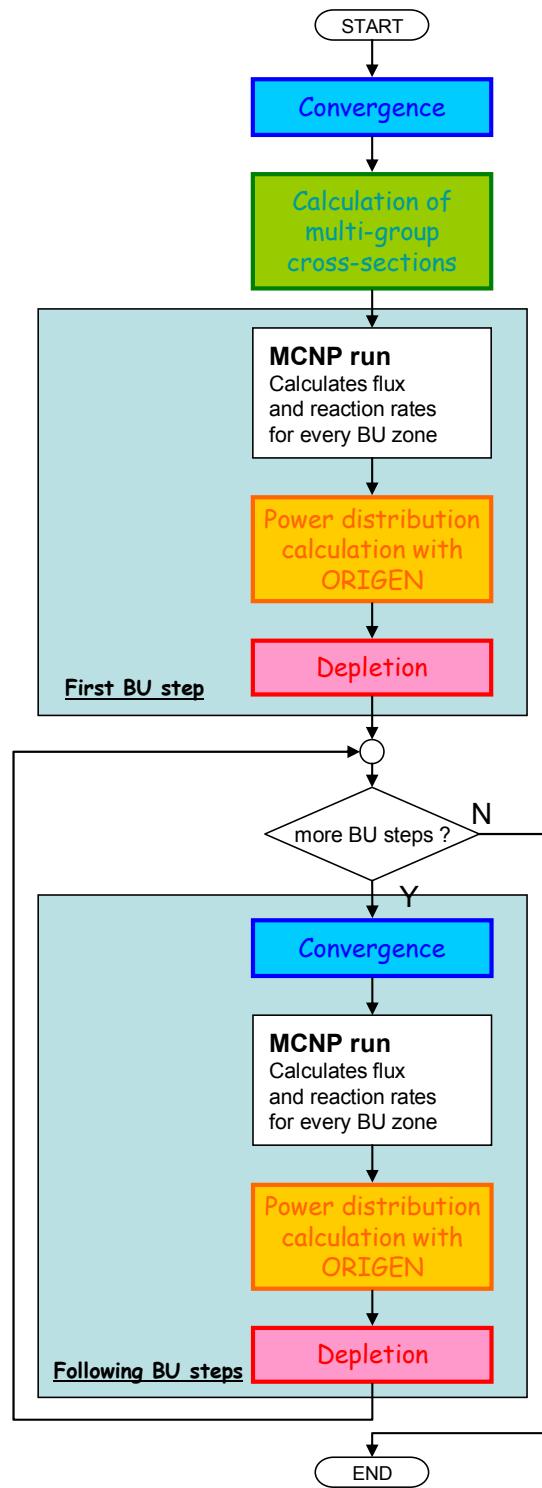


Figure 4-10: Flow-chart of the 3D burn-up simulation software.

## 5 Results

### 5.1 2D parametrical study of an HPLWR assembly's burn-up

The quality of the data sets produced at the IKE, confirmed by the successful comparisons with the experimental data, suggested the conduction of a credible, although preliminary sensitivity study, to assess the variability of the results in dependence of the physical model adopted for water, as function of the burn-up.

The goal was to obtain an index of the error affecting the results of transport and more in general of burn-up simulations carried out with inadequate thermal cross section sets for the moderator and the coolant.

The geometry chosen for this investigation is the square arrangement proposed by Bittermann (2001), depicted in Figure 1-4.

The application of the Monte Carlo was justified not only by the complexity of the fuel assembly, but also by the fact that it meets the precision requirements posed by a sensitivity calculation. On the other hand, some perplexity arose regarding the feasibility of a 3D simulation of the whole assembly.

Therefore, the goal was limited to a set of 2D burn-up simulations in correspondence of particularly meaningful values of moderator's and coolant's temperature and density.

In particular, two configurations have been implemented, featuring respectively the minimum and maximum coolant's foreseen temperatures, in combination with the minimum moderator's foreseen temperature, according to Chang's results.

These two combinations represent the configurations at the top and, approximately, at the bottom layers of the assembly.

The so conceived 2D study offered the opportunity to assess the influence of the coolant on the single horizontal layer of the fuel assembly addressing the concerns relating the large axial variation of density of the supercritical water.

The Bittermann's geometry (Figure 5-1) was implemented in MCNP with the following simplifications with respect to Chang's original work:

- temperature and density of moderator ( $T_m, \rho_m$ ) and coolant ( $T_c, \rho_c$ ) fixed all over the cross section of the fuel bundle

- identical initial enrichment for all the pins, which doesn't imply the uniform radial power distribution assumed in [3]

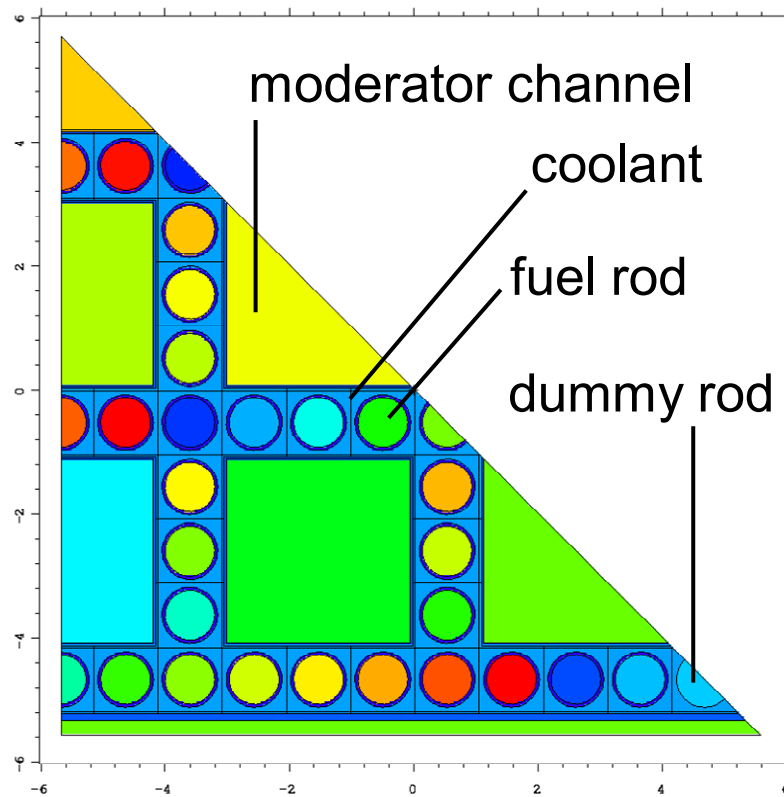


Figure 5-1: Bittermann's geometry rendered by the MCNP's plotter.

In practice the coupling of minimum foreseen  $T_m$  with, alternatively, the maximum and minimum foreseen  $T_c$  have been implemented as shown in Table 5-1.

Table 5-1: Parameter combinations for the 2D burn-up calculations.

	$T_{coolant}, \rho_{coolant}$	$T_{moderator}, \rho_{moderator}$
<b>Case 1 (top)</b>	497 °C, 88 kg/m <sup>3</sup>	282 °C, 774 kg/m <sup>3</sup>
<b>Case 2 (~bottom)</b>	297 °C, 749 kg/m <sup>3</sup>	282 °C, 774 kg/m <sup>3</sup>

Each of the two above-mentioned configurations has been implemented in three independent versions, using thermal cross sections sets developed at the IKE by Keinert et al. [15] for Hydrogen considered respectively as:

- Free gas
- Bound in the molecule of H<sub>2</sub>O in liquid phase
- Bound in the molecule of H<sub>2</sub>O in the form of vapour

maintaining of course the original  $T_m, \rho_m, T_c, \rho_c$  of the supercritical water and a fixed fuel temperature of 1500 °K.

Table 5-2: Time steps applied in the 2D parametric simulations of Bittermann's geometry.

<b>Step</b>	<b>Time (days)</b>	<b>BU (MWd/kg HM)</b>
1	0.00	0.00
2	0.50	0.02
3	1.00	0.05
4	1.50	0.07
5	3.00	0.14
6	4.50	0.21
7	7.50	0.34
8	10.50	0.48
9	15.50	0.71
10	20.50	0.94
11	35.50	1.63
12	50.50	2.31
13	100.50	4.60
13 <...< 46	+ 50	+ 2.29
46	1747.28	80.00

The influence of the physical model adopted for the moderating means is testified for example by the different spectra (Figure 5-2, Figure 5-3) arising in the fuel in dependence of the thermal cross section set used.

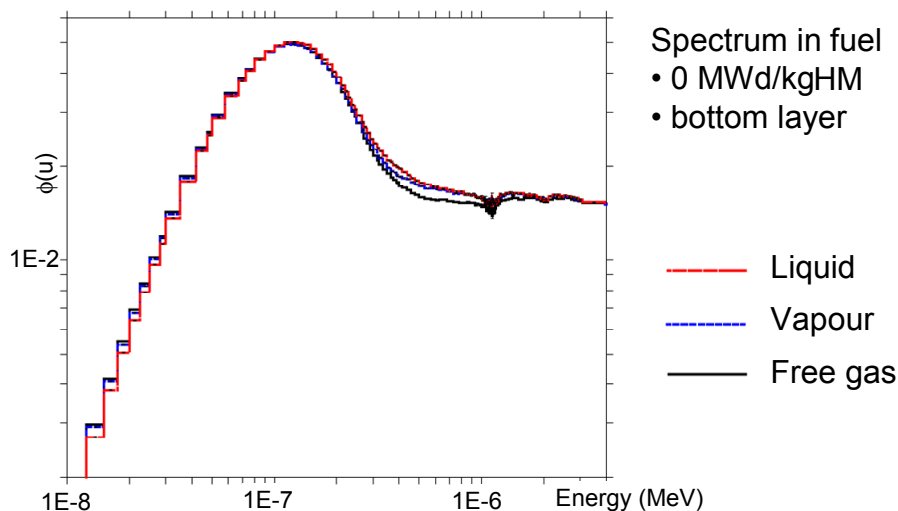


Figure 5-2: Spectra detected by MCNP in fresh fuel using the three different models for hydrogen. Coolant temperature = 297 °C (bottom layer).

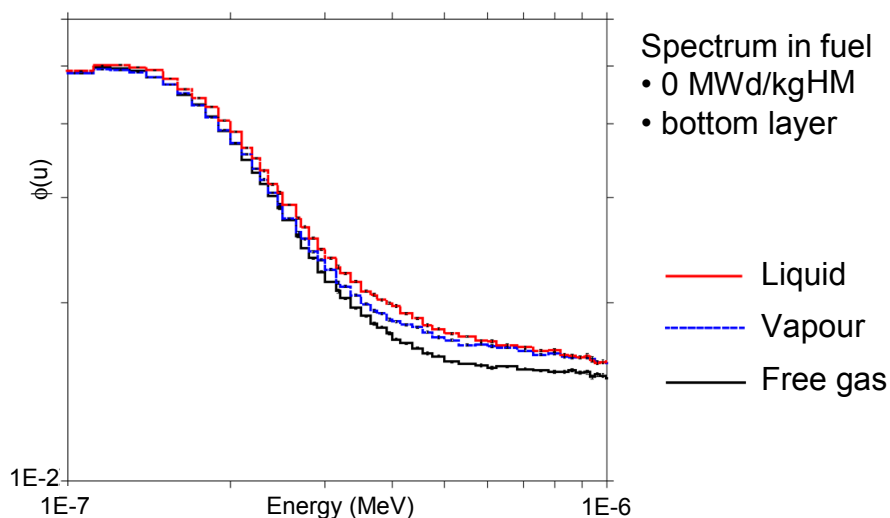


Figure 5-3: Detail of Figure 5-2.

Although the scattering is ruled by quantum mechanics, many results at macroscopic level are easily subject to reasonable interpretations according to classical mechanics.

The intuitive idea that a neutron hitting the nucleus of a Hydrogen atom bound in a molecule of  $H_2O$  scatters against a body much more massive than the Hydrogen atom itself, can give a rough explanation to the harder spectra found for liquid water and vapour, in that a more massive body has a lower capacity to absorb momentum.

Moreover, the independence enjoyed by the molecules of vapour, which only loosely interact with each other, gives vapour a moderating capacity somewhat in the middle between the liquid and the free gas models, whereas the same molecules in the liquid state, being bound in clusters, don't enjoy the same freedom to rotate and translate. A quantitative, although indirect index of the repercussions of the different moderating

properties are the corresponding discrepancies in the capture rates, shown in Figure 5-4 and Figure 5-5, due to the different average lethargy steps.

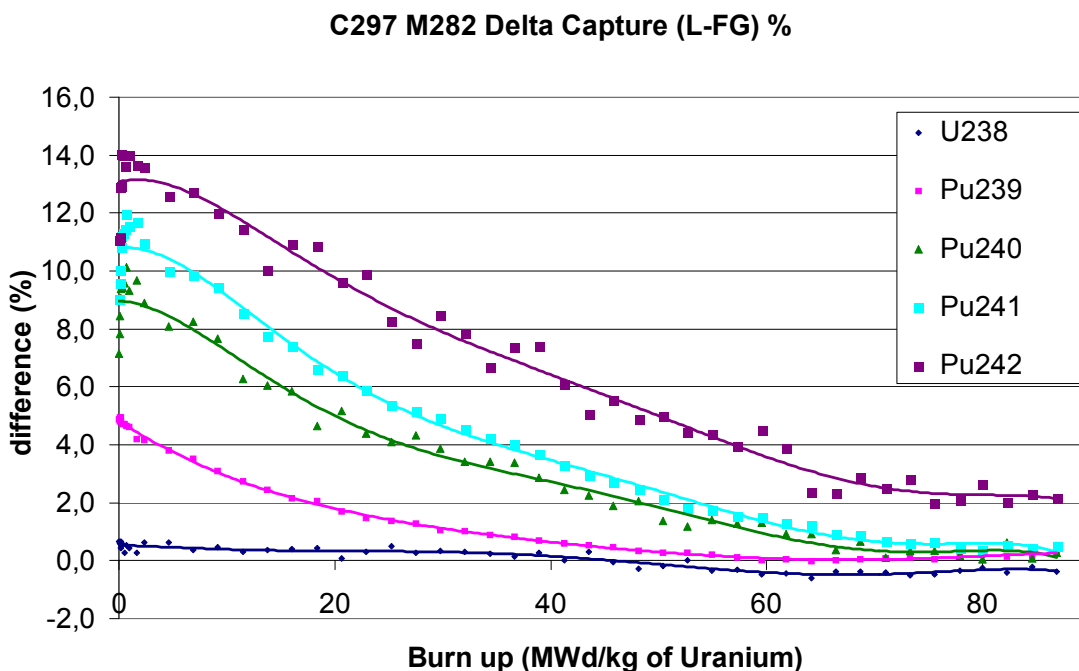


Figure 5-4: Difference between the capture rates in the fuel foreseen by the liquid and free gas models, in the bottom layer.

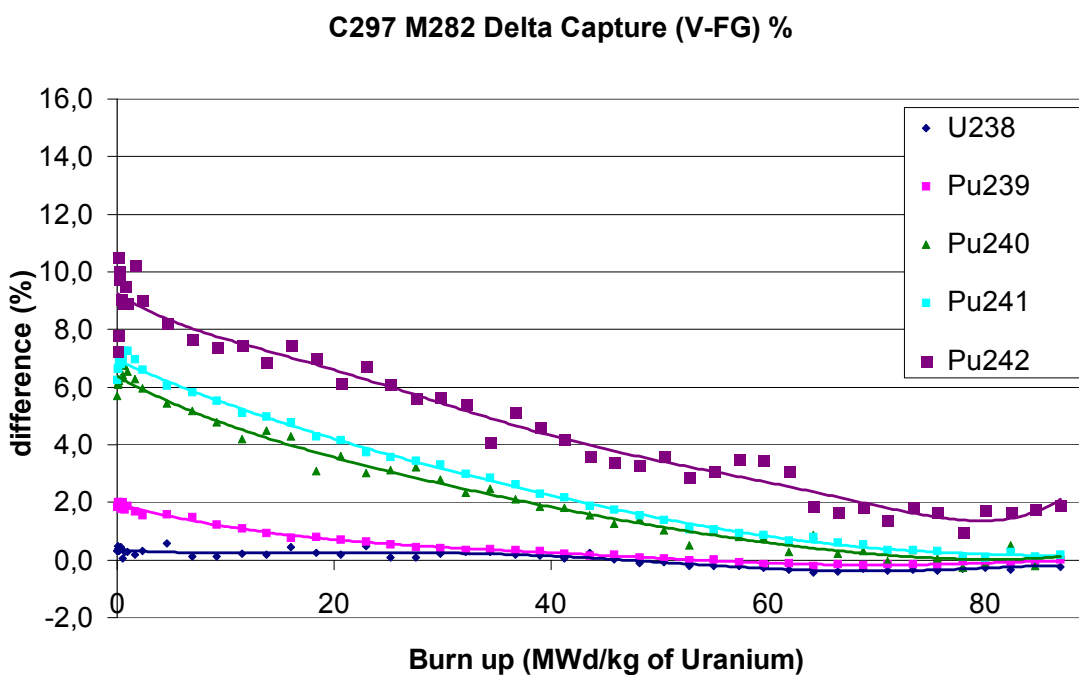


Figure 5-5: Difference between the capture rates in the fuel foreseen by the vapour and free gas models, in the bottom layer.

Consistently, the large discrepancies for fresh fuel and the trend towards agreement along the burn-up between the reaction rates observed using the different thermal cross-sections are featured also by the diagram in Figure 5-6, depicting the behaviour of the  $K_{inf}$ 's with respect to each other.

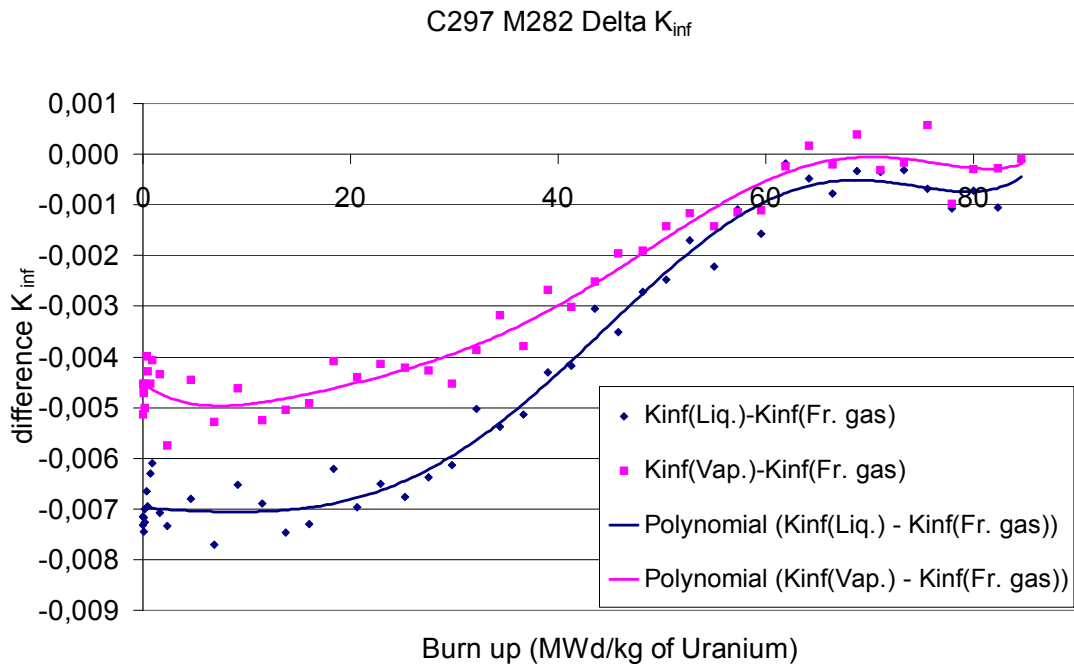


Figure 5-6: Difference between the  $K_{inf}$ 's foreseen in the bottom layer by the liquid and free gas models (blue line); by the vapour and free gas models (pink line).

Figure 5-7 and Figure 5-8 qualitatively confirm the  $K_{inf}$  behaviours' differences. Whereas the total fission rate difference (black line in Figure 5-7) remains negligible, the total capture rate's difference due to the main actinides (black line in Figure 5-8) increases until about 25 MWd/kg HM, and then gradually decreases to zero.

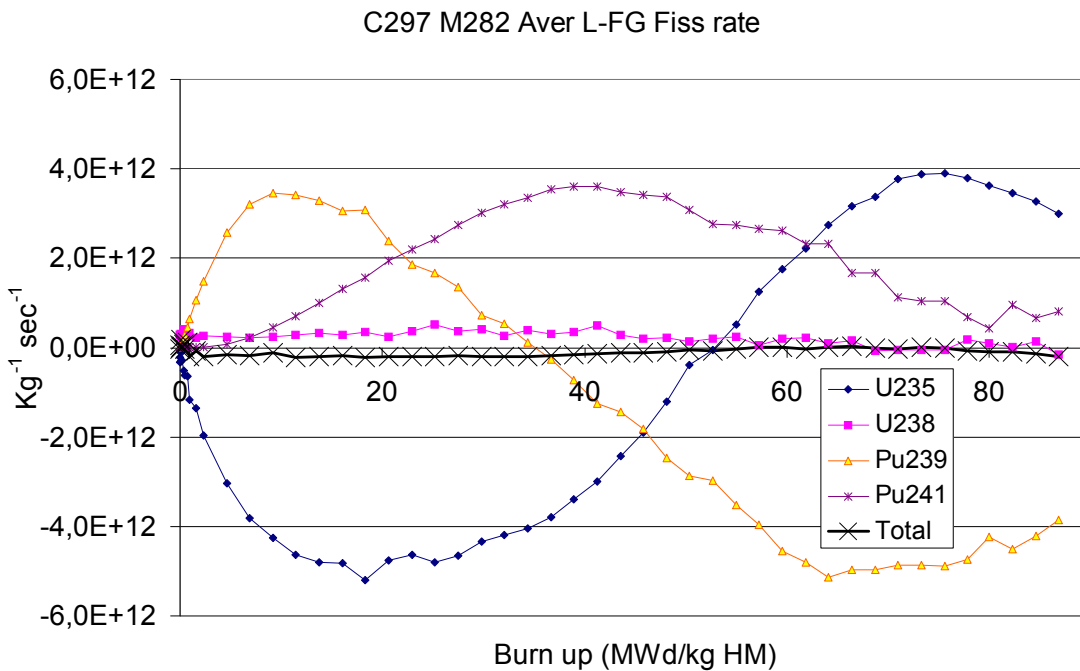


Figure 5-7: Difference between the fission rates foreseen by the liquid and free gas models in the bottom layer.

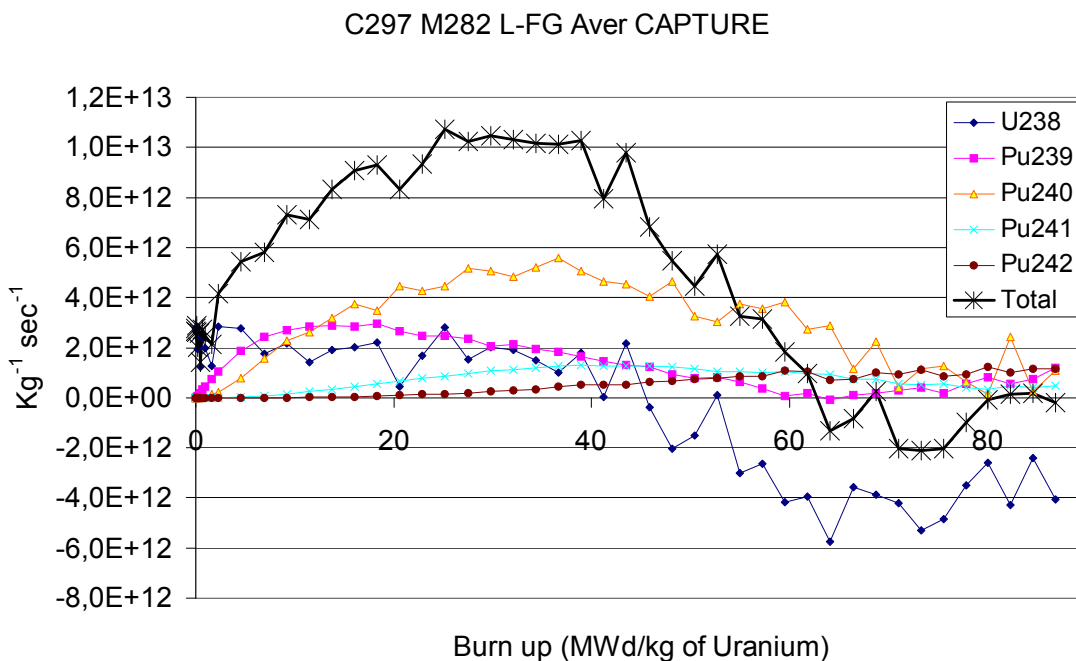


Figure 5-8: Difference between the capture rates foreseen by the liquid and free gas models in the bottom layer.

Figure 5-9 suggests a possible explanation of the gradual shrinking of the discrepancies: the higher rates of capture foreseen by the molecular models of water lead to a higher production and subsequent consumption of Pu, whose burning lets save U<sup>235</sup>. The fore-

seen difference in concentration of  $U^{235}$  between the molecular and the free gas models gets larger and larger with the burn-up, until it makes up for the effect of the worse moderator.

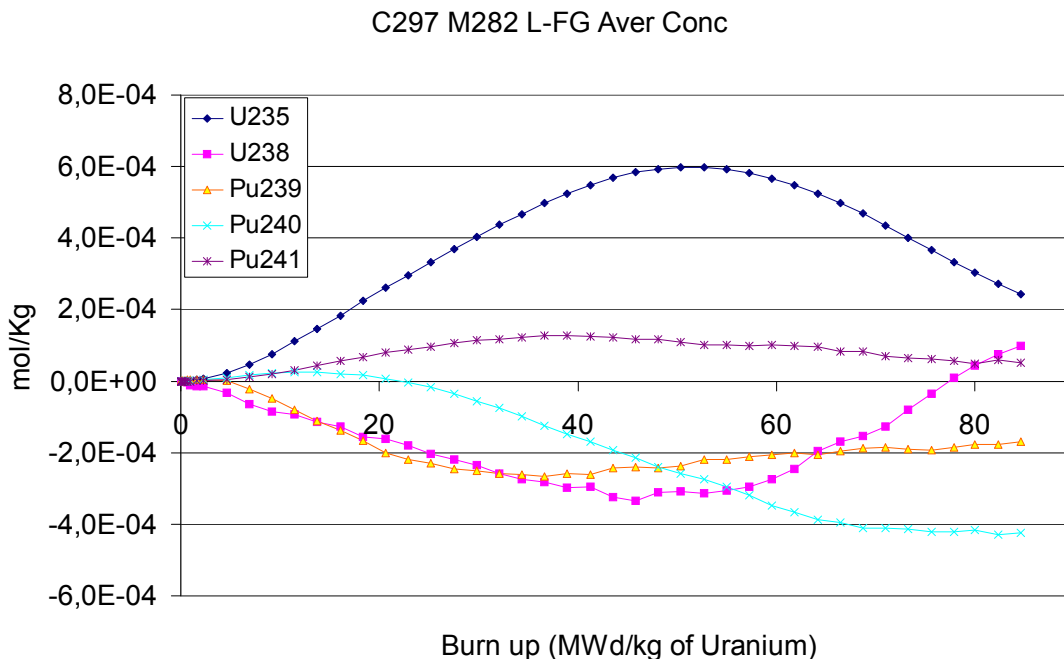


Figure 5-9: Difference between the major actinides' concentrations foreseen by the liquid and free gas models in the bottom layer.

This would be in agreement with the fact, visible in Figure 5-7, that the total fission rate in the geometry moderated with liquid water features a sensibly lower contribution from  $U^{235}$  during the first half of the burn-up than in the second, and confirms the idea that with liquid water  $U^{235}$  is saved (compared with the free gas model) during the first half of the burn-up and is burnt in the second (Figure 5-9).

Figure 5-7, on the other hand, gives a warning on the realism of these comparisons. The total fission rate's difference being constantly around zero reminds that comparisons have been made between results obtained from simulations carried out independently from each other, but imposing the same power.

It's reasonable to think that in a 3D geometry, using different thermal cross section sets would lead to corresponding slightly different axial power distributions.

The power developed in corresponding layers would in general not be the same, and the described mechanism involving  $U^{235}$  shouldn't necessarily be expected.

A second compensation effect, at least qualitatively not dependent on the particular circumstances of these 2D-simulations, could be the Pu resonances' self shielding.

Figure 5-10 depicts the spectrum in the bottom layer for increasing values of the burn-up.

The big resonance of Pu<sup>240</sup>'s capture cross section at about 1 MeV (Figure 5-11) is at the origin of the increasing negative peak in the spectrum at corresponding energy, represented in Figure 5-10.

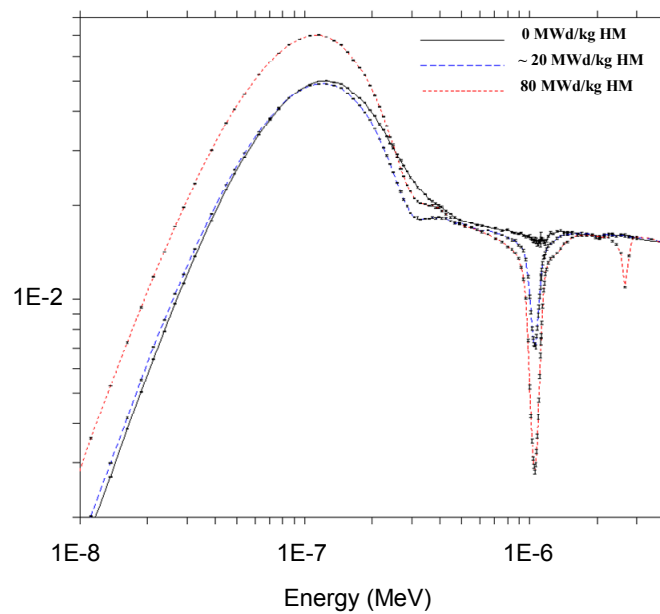


Figure 5-10: Spectra in the fuel in the bottom layer tallied at 0, around 20 and 80 MWd/kg HM. The negative peaks at about 1E-06 MeV and 3E-06 MeV correspond to resonances in the capture cross sections.

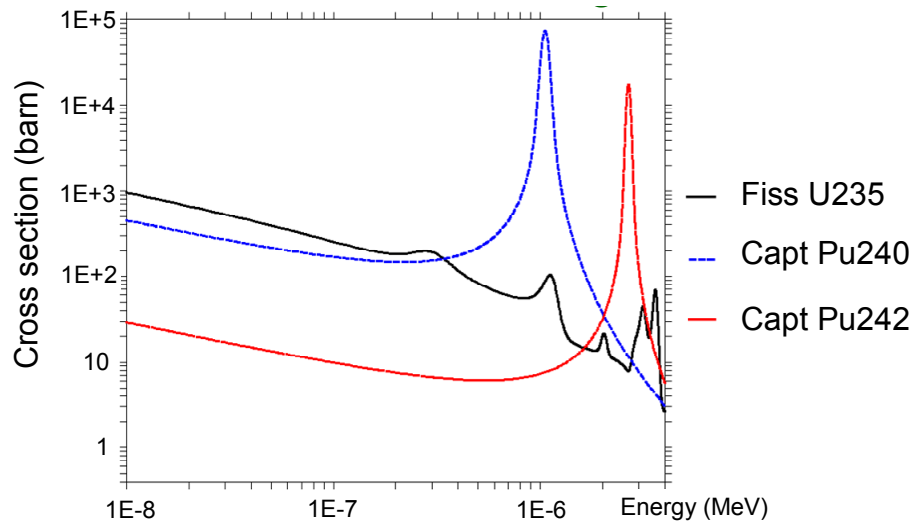


Figure 5-11: Capture cross sections resonances that manifestly cause the growing negative peaks in the spectrum shown in Figure 5-10. Also the fission cross section of  $U^{235}$  has small peaks in the same energy regions, but they are clearly irrelevant.

The big negative peak destroys the discrepancies in the spectra due to the different thermal cross sections in the interval around 1 MeV, possibly leading to similar capture rates, considered that that resonance is responsible of most of  $Pu^{240}$ 's captures. Such an idea would be consistent with the curve referring to  $Pu^{240}$  in Figure 5-8.

The remarkable difference between the spectra arising in the top and bottom layers shown in Figure 5-12 testifies the coolant's relevant contribution to the moderation.

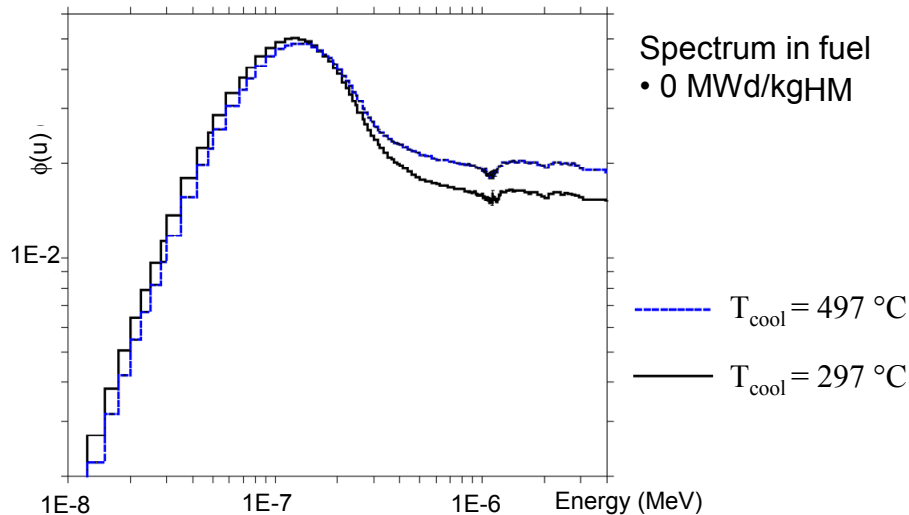


Figure 5-12: Spectra in the fresh fuel in the (~) bottom (black line) and top (blue line) layers.

Whereas the sensibly harder spectrum for fresh fuel in the top layer doesn't lead to a dramatically different  $K_{inf}$  (Figure 5-13), Figure 5-14 and Figure 5-15 show relevant differences in the net production of the fissile Pu isotopes.

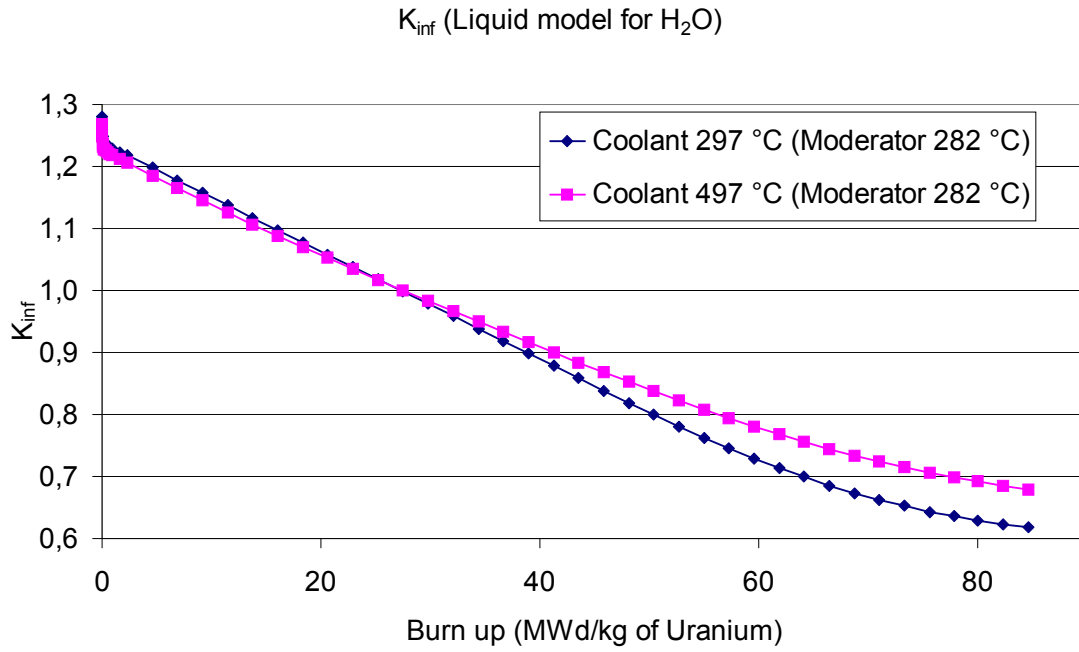


Figure 5-13: The blue line refers to the bottom layer. The pink one to the top layer.

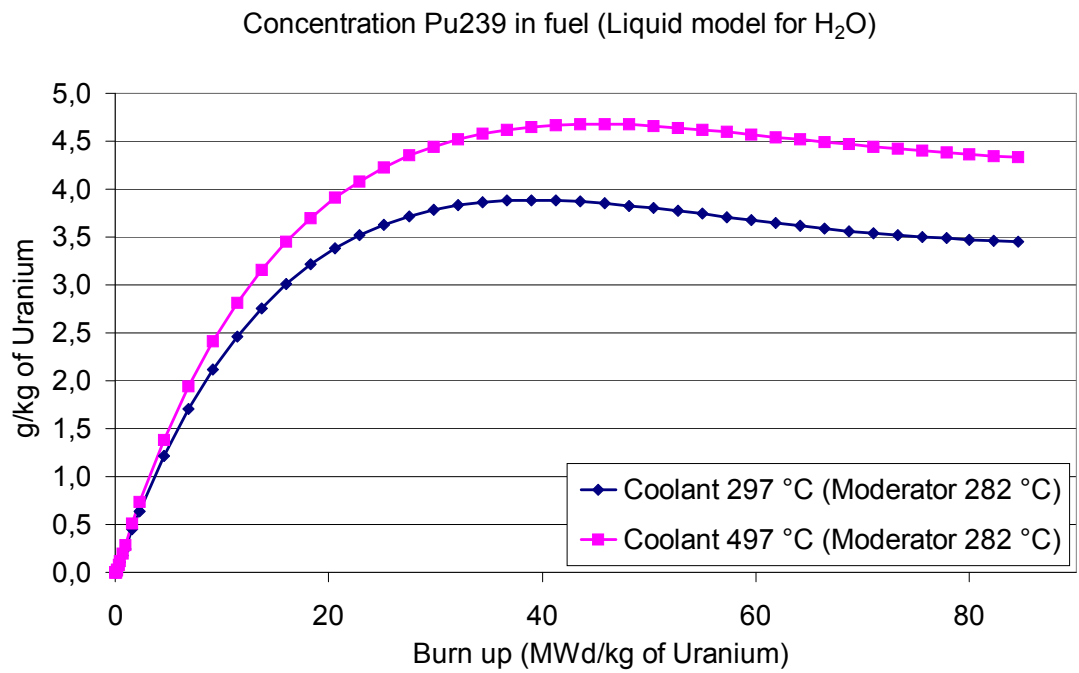


Figure 5-14: Concentration of Pu<sup>239</sup> in the (~) bottom (blue line) and top (pink) layers.

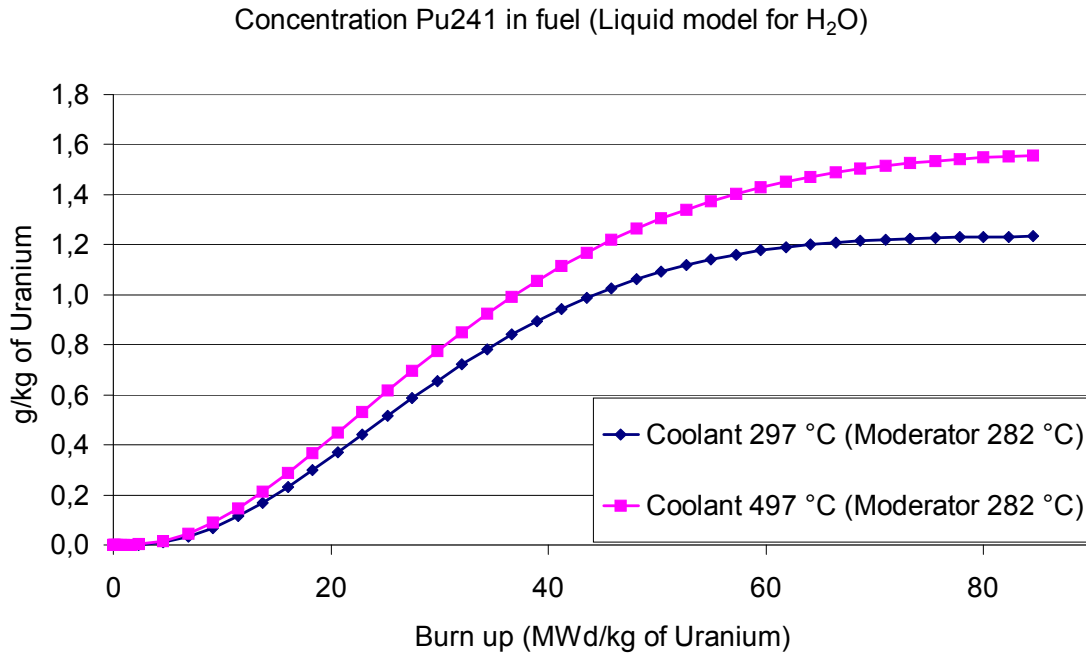


Figure 5-15: Concentration of Pu<sup>241</sup> in the (~) bottom (blue line) and top (pink) layers.

According to the BWR's experience, the bottom layer's  $K_{inf}$  is outpaced along the burn-up by the top layer's  $K_{inf}$  (Figure 5-13) just because of the increasing relative abundance of the Pu fissile isotopes in the hot layer with respect to the cold one.

This mechanism has probably been amplified by the limits of the 2D-simulations, carried out imposing the same, constant power and fuel temperature to both layers and constant coolant's and moderator's temperatures throughout the burn-up.

In particular, having imposed the same power to both hot and cold layer involved the same fission (for low burn-up nearly exclusively from U<sup>235</sup>) rate in the two cases, and this in turn forced much higher capture (for low burn-up nearly exclusively by U<sup>238</sup>) rates in the hot one, where the moderation capacity is worse. The subsequent foreseen difference in Pu production between the extreme layers is supposedly much higher than it would be in a 3D geometry, in which the power distribution would be affected by the water density and the Doppler Effect.

In this context, quantitative data must be taken with caution.

### 5.1.1 Conclusions

The unavailability of thermal cross section sets specifically prepared for supercritical water gives rise to uncertainties regarding the most important parameters representing the fuel performance. The variability of the results in dependence of the adopted water's

thermal cross section set is beyond the tolerances accepted in the nuclear reactors licensing.

Considering that for fresh fuel a reactivity gap of about 1\$ has been observed between the simulations carried out applying the liquid and the free gas models, and that the free gas model doesn't even take into account the molecular structure of water, transport and burn-up simulations regarding the HPLWR carried out using the free gas model can not be considered credible.

For high burn-up, the results tend to agree. But the compensation effects underlying this tendency largely lie in a delicate mechanism of power repartition among the different fissile isotopes in the burnt fuel. As the power simulated in a 2D simulation is arbitrary, the magnitude of these phenomena is subject to verification through a 3D simulation.

The comparison between hot and cold layers reveals that the coolant has a relevant moderating role, leading to phenomena typical of a BWR.

The warning on the limits of a 2D simulation applies also and even more so here but, in this case, the necessity of a coupled transport-thermal-hydraulics calculation must be stressed, in that the water's density and temperature axial distributions found by Chang were calculated neglecting the thermal interaction between fuel and water.

## 5.2 3D burn-up simulation of an HPLWR assembly

As reaching the first neutronic-thermal hydraulic convergence had turned out to be quite resource-consuming (see 4.5.1), a more straightforward sequence of burn-up steps was set up than in the previous 2D parametrical study: in a first experiment the number of steps for the first 50.5 days was reduced from 11 to 7, while from 50.5 days on a fixed step length of 100 days was applied.

This choice led to relevant stability problems of the power profile, mainly due to the fact that the long steps didn't let  $\text{Xe}^{135}$  develop properly.

Bearing in mind the lessons of the first try, a second experiment was set up, with the goal of obtaining a more gradual evolution of the power profile.

The dense steps sequence for the first 50.5 days (which had been used in the 2D simulations) was maintained in order to help  $\text{Xe}^{135}$  develop correctly. For these first 11 burn-up steps the convergence criterion was retained unchanged.

From 50.5 days on a fixed step-length of 7 days was chosen. Correspondingly, in order to contain computation times, the convergence criterion stated at the end of 4.5.1 had to be given up in favour of a fixed rule of two convergence loops preceding every depletion step.

Structured this way, the simulation must be composed of 243 steps. Actually, the process was stopped after 83 steps because of a hardware problem, so that the fuel was burnt only until 26.50 MWd/kg HM.

Figure 5-16 to Figure 5-25 show some of the obtained axial power profiles.

The initial profile, peaked at the bottom, gets gradually more and more balanced, without the wide oscillations observed in the first experiment.

The power becomes quite uniformly distributed along the axial coordinate (apart from the extremes, of course) at  $\sim 10$  MWd/kg HM.

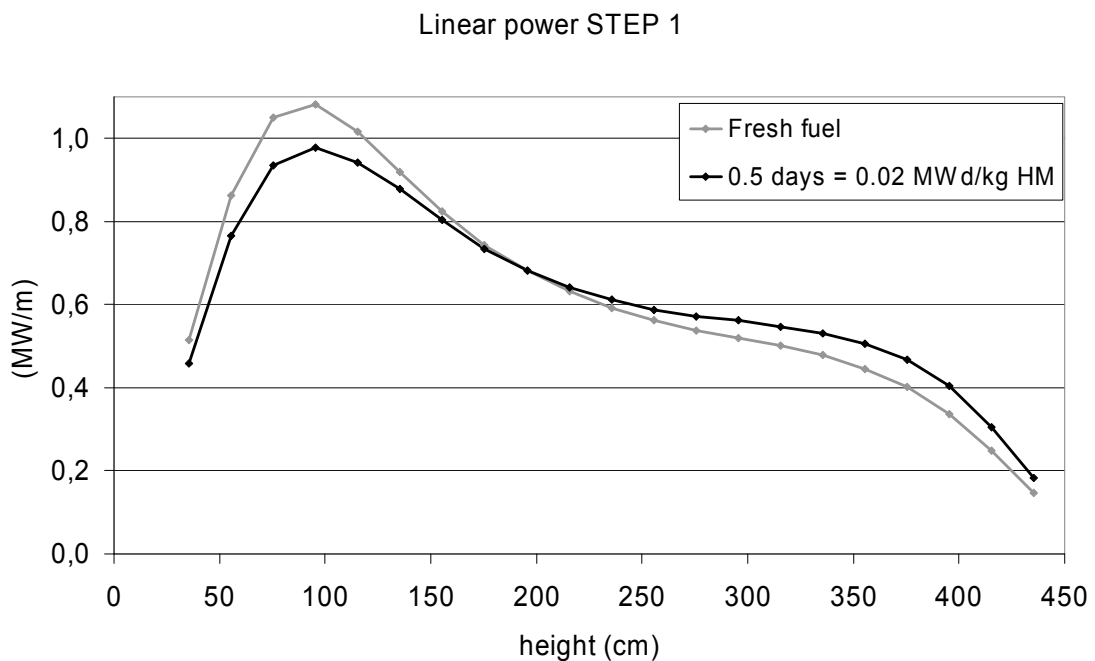


Figure 5-16: Fuel assembly's linear power axial profile at the beginning and at the end of the 1<sup>st</sup> burn-up step.

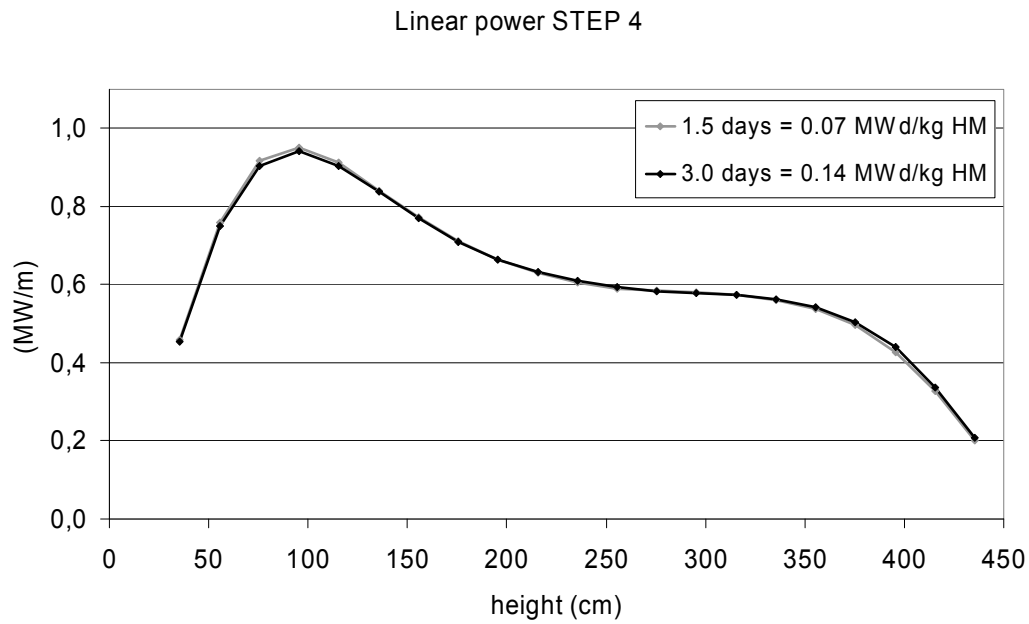


Figure 5-17: Fuel assembly's linear power axial profile at the beginning and at the end of the 4<sup>th</sup> burn-up step.

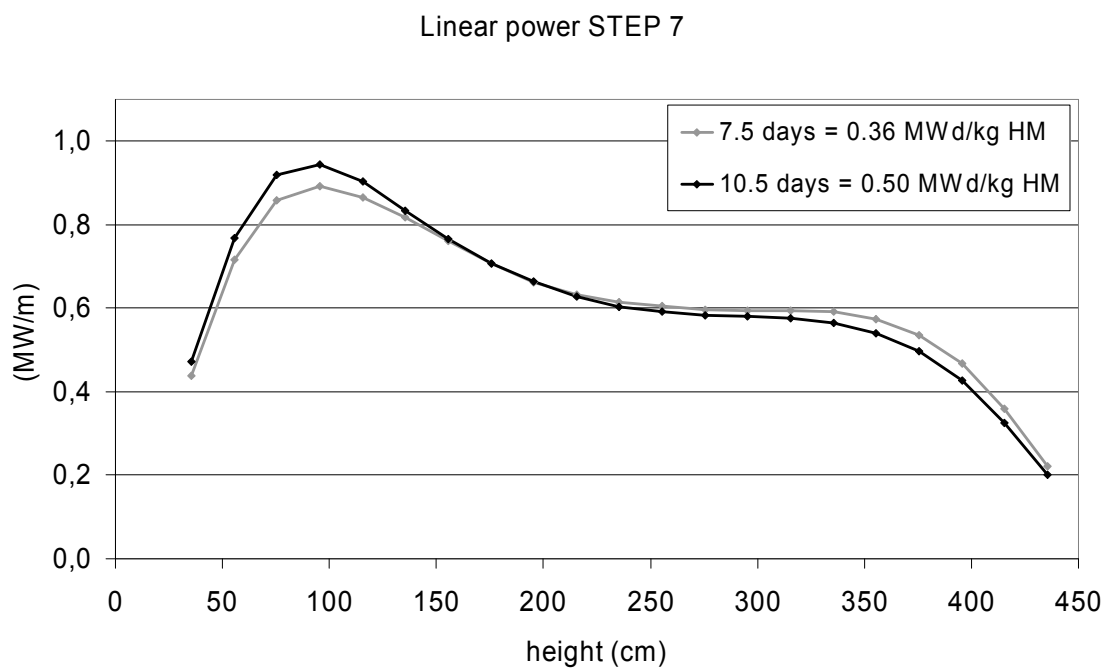


Figure 5-18: Fuel assembly's linear power axial profile at the beginning and at the end of the 7<sup>th</sup> burn-up step.

## Linear power STEP 11

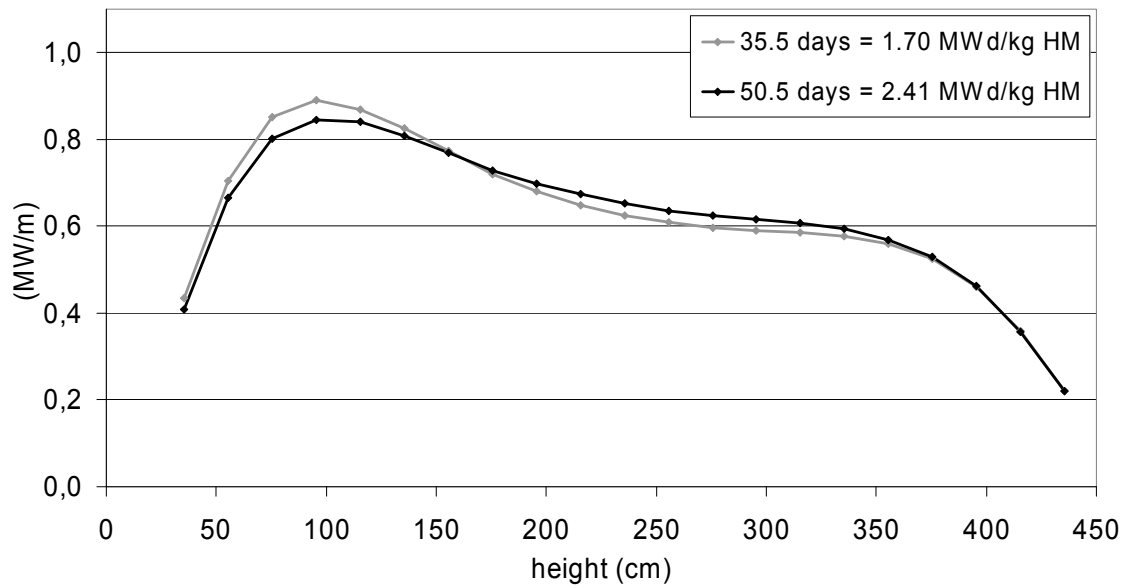


Figure 5-19: Fuel assembly's linear power axial profile at the beginning and at the end of the 11<sup>th</sup> burn-up step.

## Linear power STEP 18

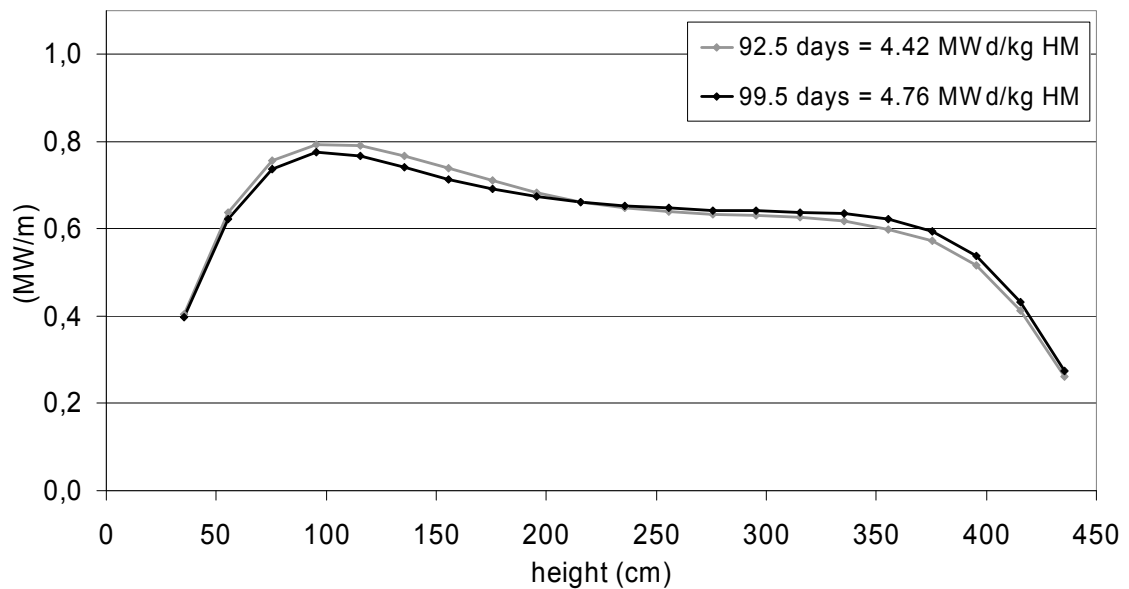


Figure 5-20: Fuel assembly's linear power axial profile at the beginning and at the end of the 18<sup>th</sup> burn-up step.

## Linear power STEP 31

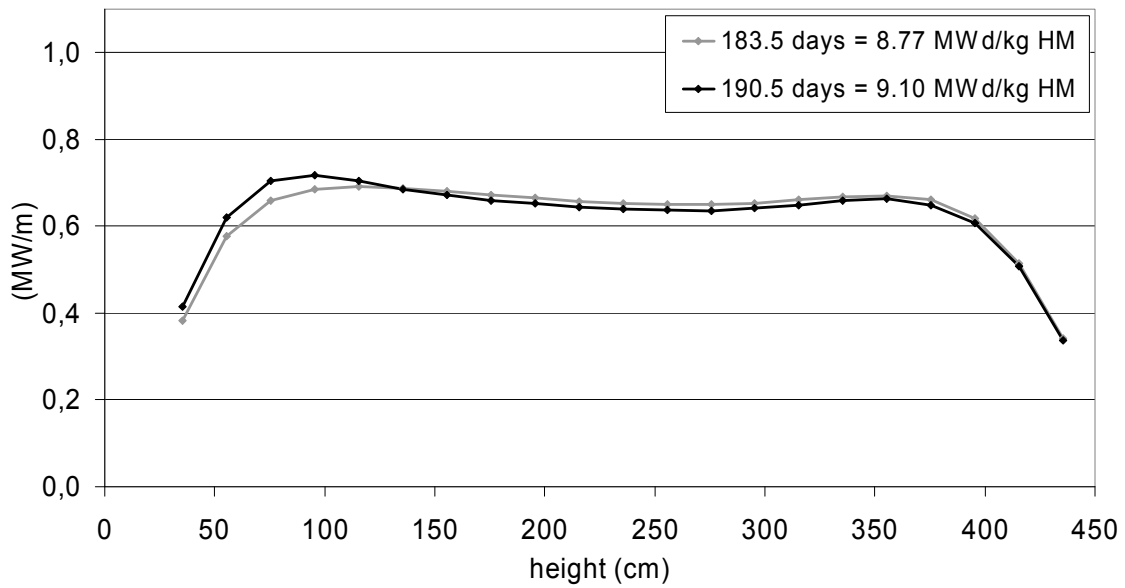


Figure 5-21: Fuel assembly's linear power axial profile at the beginning and at the end of the 31<sup>st</sup> burn-up step.

## Linear power STEP 44

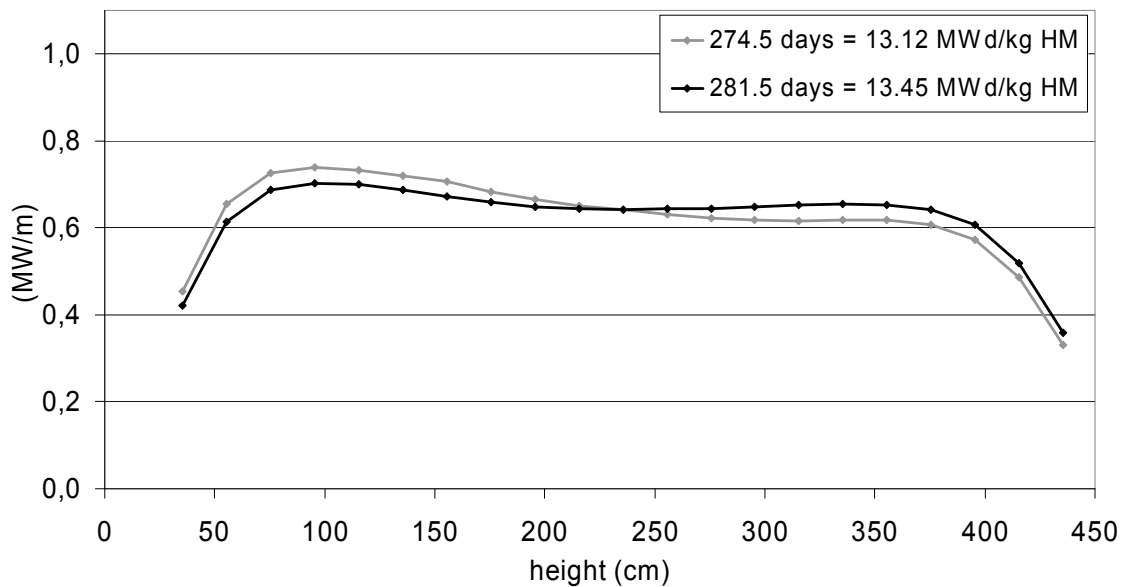


Figure 5-22: Fuel assembly's linear power axial profile at the beginning and at the end of the 44<sup>th</sup> burn-up step.

## Linear power STEP 57

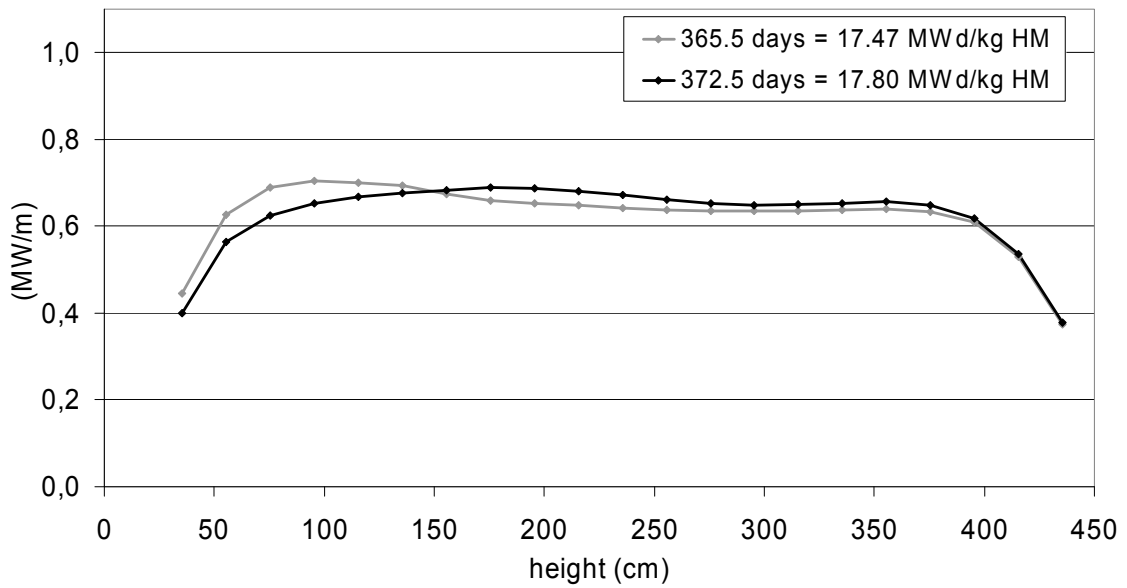


Figure 5-23: Fuel assembly's linear power axial profile at the beginning and at the end of the 57<sup>th</sup> burn-up step.

## Linear power STEP 70

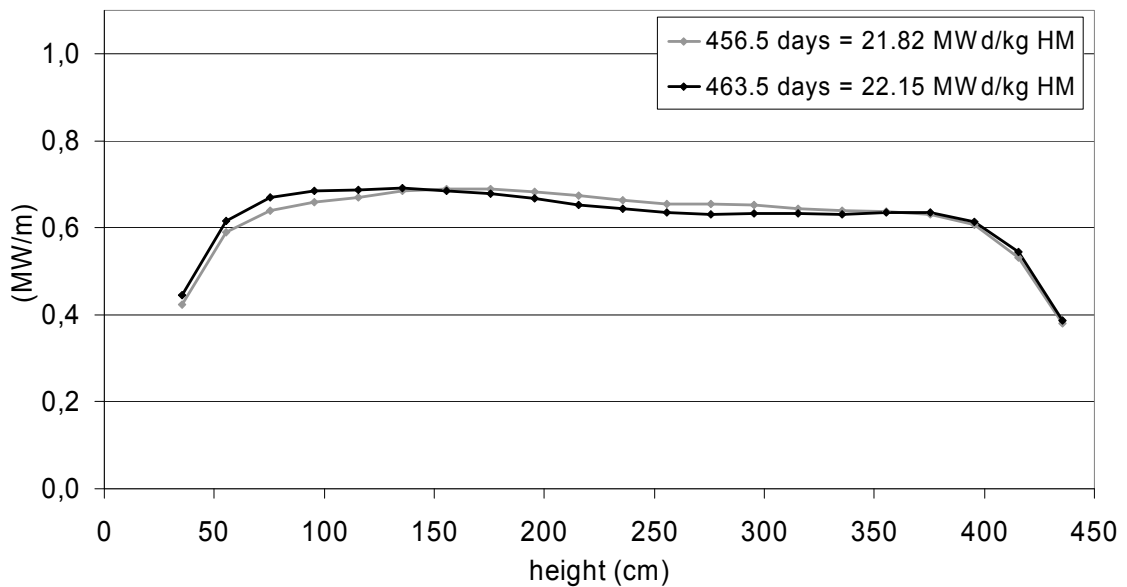


Figure 5-24: Fuel assembly's linear power axial profile at the beginning and at the end of the 70<sup>th</sup> burn-up step.

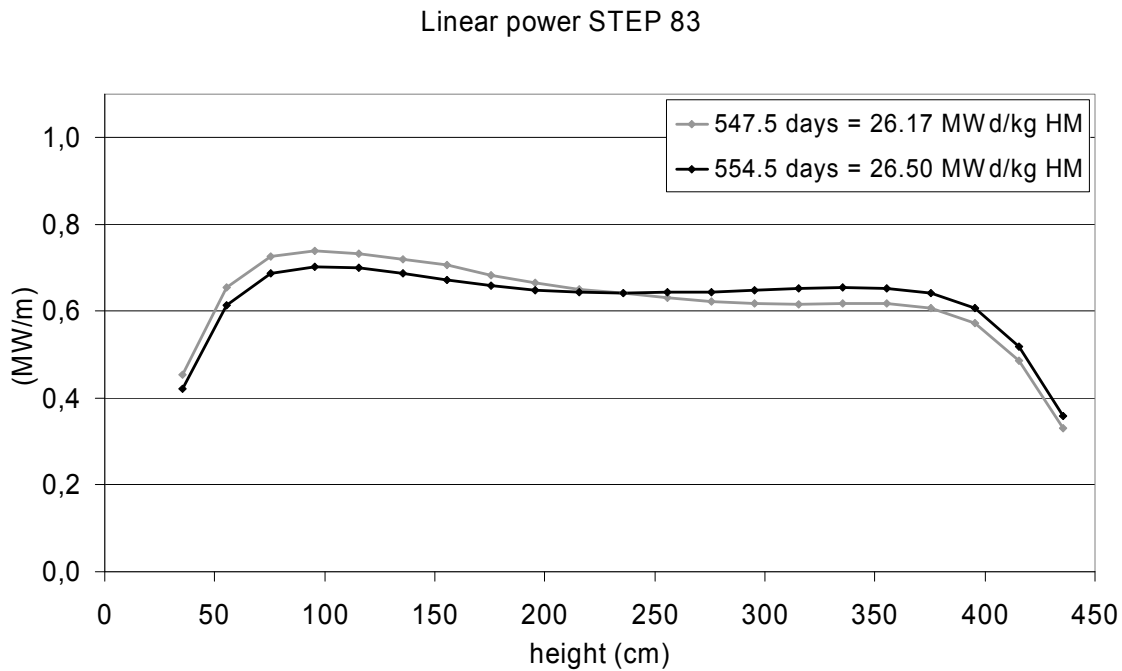


Figure 5-25: Fuel assembly's linear power axial profile at the beginning and at the end of the 83<sup>rd</sup> burn-up step.

An issue that was source of perplexity in the 2D simulations was the realism of imposing the same power to the top and bottom layers. Figure 5-26 shows that such an assumption is not far from reality.

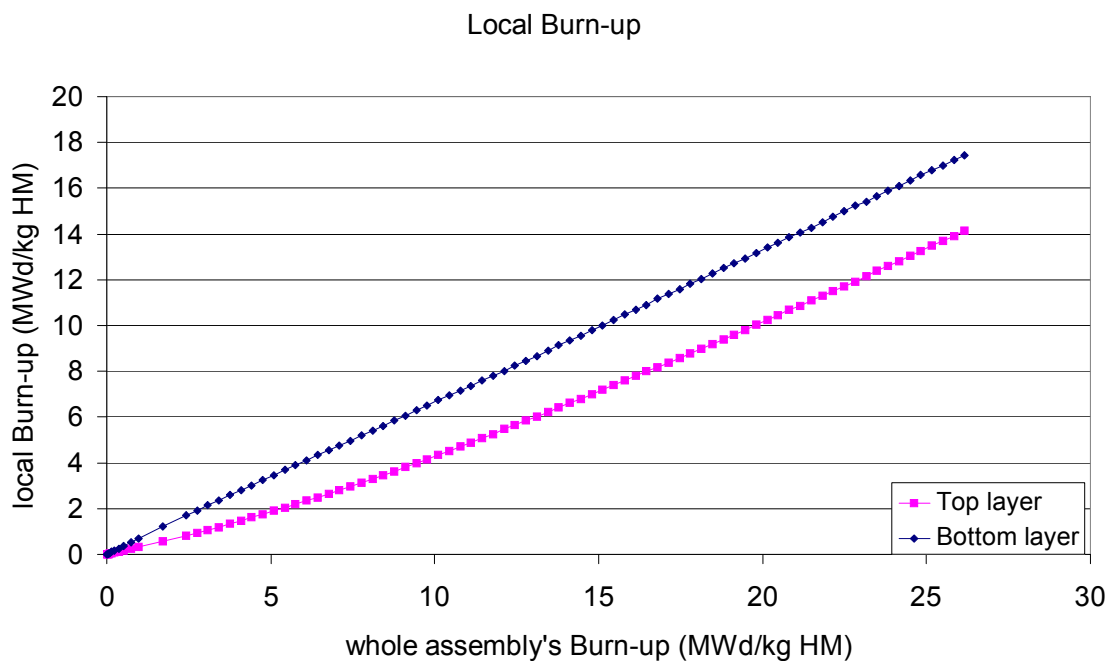


Figure 5-26: Local burn-up in top and bottom layers as a function of the whole assembly's burn-up.

The power developed at the extreme layers is sensibly different only until about 10 MWd/kg HM. The diagram in Figure 5-26 shows how the progression of the local burn-up in the top layer, initially slower, begins to have the same inclination in proximity of the over-mentioned global burn-up. From there on the vertical distance between the two curves remains at about 3 MWd/kg HM.

The change from the initial power distribution, peaked at the bottom, to a more uniform one has positive repercussions on the assembly's moderation.

The coolant's temperature rise in the low layers is smaller, and this leads to a higher average density of the water in this region (see Figure 5-27), making the overall water density's profile a bit more balanced.

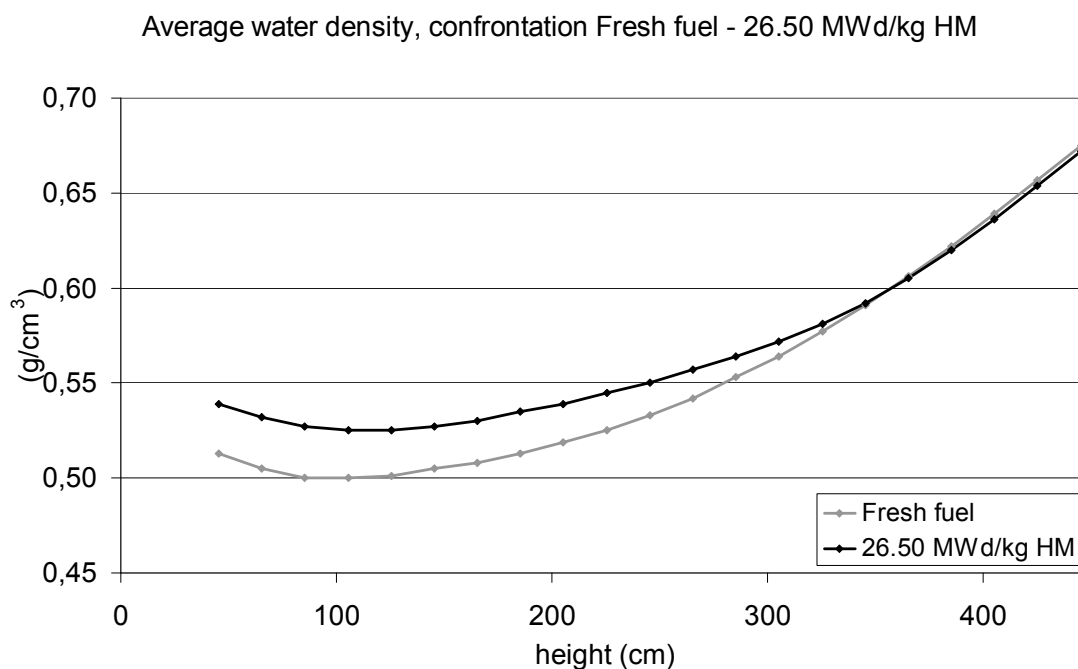


Figure 5-27: The average includes coolant, moderator in the box and in the gap. 554.5 days correspond to 26.50 MWd/kg HM.

The conclusions regarding the cladding's thermal stress that had been drawn for the time being by Waata [5] on the basis of an analysis with only fresh fuel, had to be retracted.

At 35.5 days a transgression of the limit of 620 °C is observed for the first time in the cladding temperature of sub-channel 9 (Figure 5-28).

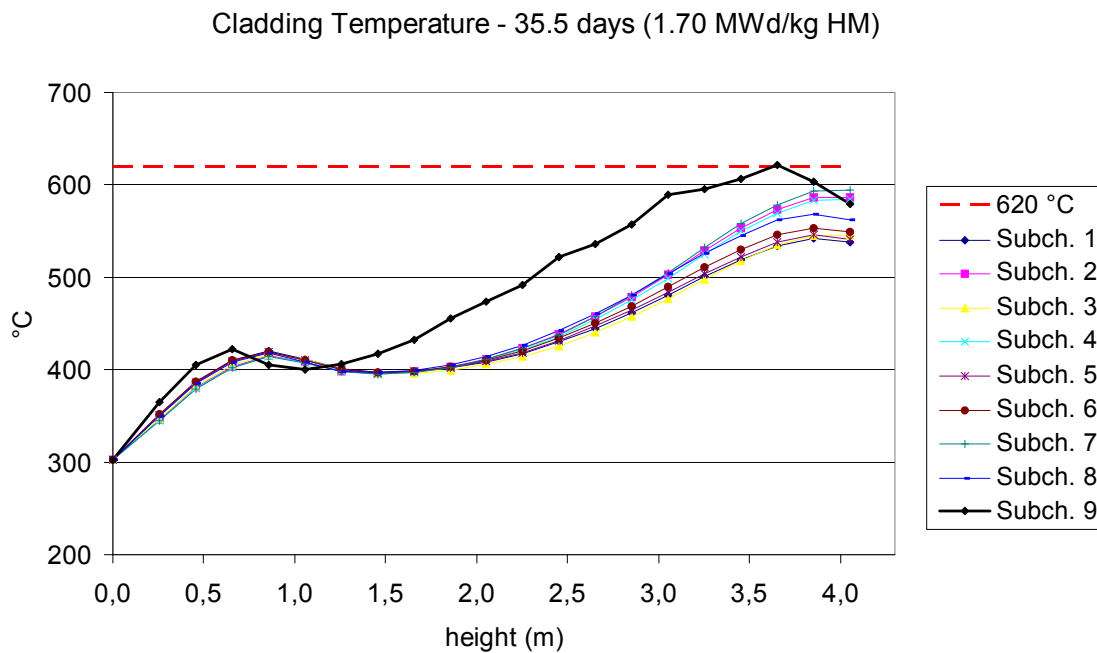


Figure 5-28: The line in bold refers to the sub-channel where the temperature rose above the 620 °C limit. 35.5 days correspond to 1.70 MWd/kg HM.

At 239.5 days a transgression also in sub-channel 7 is observed. Figure 5-29 also gives an idea of the magnitude of the problem, at this point, in sub-channel 9.

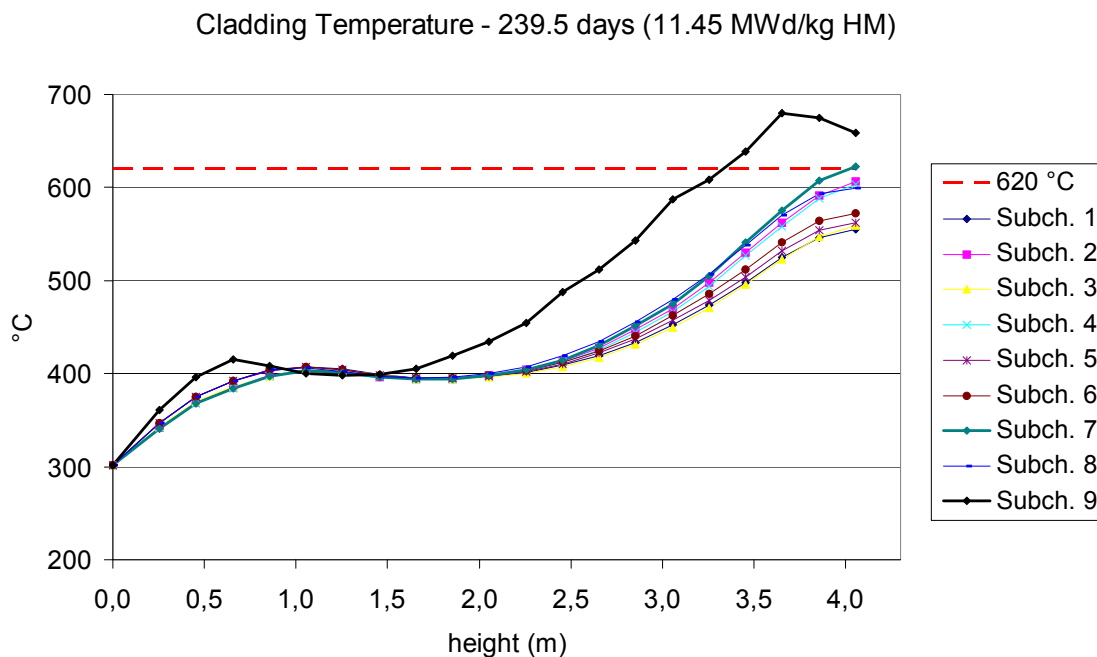


Figure 5-29: The lines in bold refer to the sub-channels where the temperature rose above the 620 °C limit. 239.5 days correspond to 11.45 MWd/kg HM.

### 5.2.1 Conclusions

In the context of the coupling of a transport, a thermal-hydraulic and a depletion programs, in order to perform 3D burn-up simulations, the use of a Monte Carlo program in this moment is not recommended.

The 3D simulation was performed using 24 processors: to simulate 26.50 MWd/kg HM it took about 2.5 months. It must be kept in mind that from the 12<sup>th</sup> step on, no convergence criterion was respected, but a fixed number of 2 iterations between MCNP and STAFAS was imposed. Although the diagrams look credible, such an approach can not be systematically applied in the industrial domain. The problem with the neutronics – thermal-hydraulics coupling are the oscillations of the power profile about the equilibrium, which involve a number of additional iterations to satisfy the convergence criterion, even when the profile's shape is nearly correct. These oscillations have nothing to do with the fact that the Monte Carlo is affected by statistical uncertainty. Actually, MCNP's input was set up so that the tallied flux and the tallied power in every burn-up zone were affected by relative errors well below 1%. This in contrast to the convergence criterion, which had a tolerance of 5 % on the whole power deposited in each of the three pieces the assembly was axially subdivided in (first 7 layers, layers from 8 to 14, layers from 15 to 21).

Of course one could turn to a looser integral criterion, for example spanning over all the 21 layers: but it gets always harder to justify the employment of a very precise but expensive tool like the Monte Carlo when the proposed convergence criterion gets looser and looser.

On this basis, taking into consideration the possibility of sensitivity calculations using different thermal cross section sets for water doesn't even make sense.

The inaccuracy bound to the convergence problems didn't keep from ascertaining two features put in light by the burn-up simulation.

First of all, the cladding temperature exceeding the limit of 620 °C, not only in the narrow sub-channel 9 but also in sub-channel 7.

Second, the beneficial repercussions of the burn-up on the power profile, which achieves a nearly uniform axial distribution at ~10 MWd/kg HM. It must be borne in mind, however, that this conclusion can not be extended to the whole of a cluster without appropriate simulation of the interplay of the fuel element with its neighbours.

### 5.3 2D burn-up simulation of the definitive geometry

With a philosophy similar to the one described in 5.1, a set of 2D burn-up simulations was set up in correspondence of certain configurations, considered most interesting.

In Table 5-3 the 6 considered configurations are resumed.

Table 5-3: “L” =  $S(\alpha,\beta)$  for liquid, “V” =  $S(\alpha,\beta)$  for vapour, “FG” = Free Gas approximation. “cold wall” = steel sheets wet by the moderator, “hot wall” = steel sheets wet by the coolant. Note that each of the configurations “Evap. Middle” and “2<sup>nd</sup> Superheater Top” have been considered twice, using different  $S(\alpha,\beta)$  for the coolant.

	<b>Evap. Bottom</b>	<b>Evap. Middle</b>	<b>Evap. Top</b>	<b>2<sup>nd</sup> Superh. Top</b>
	Mod: L Cool: L	Mod: L Cool: L,V	Mod: L Cool: V	Mod: L Cool: FG,V
T. cladd. (°K)	708	730	744	824
T. mod. box (°K)	635	620	575	585
T. cool. (°K)	635	660	680	780
T. gap (°K)	635	625	575	585
T. honeycomb (°K)	635	640	627.5	682.5
T. cold wall (°K)	635	625	575	585
T. hot wall (°K)	660	660	680	780
T. fuel (°K)	1000	1000	1000	1000

The main goal was to get an idea of the power distribution among the fuel rods, with its dependence on the considered layer and on the burn-up.

In this context, the evaporator’s bottom layer was picked out because having the highest water average density; the evaporator’s middle layer because close to the point where the pseudo-transition of phase takes place; the evaporator’s top layer in that the moderator density there is the highest; and the 2<sup>nd</sup> superheater’s top layer because the coolant density there is the lowest.

In MCNP's input the following simplifications were introduced with respect to the real geometry:

The honeycomb of steel and the alumina in the middle of the “sandwich” have been homogenized.

As the so called “cold wall”, that is the steel sheets wet by the moderator, are perforated, the steel has been homogenized with the (very little) moderator water filling the holes.

As visible in Figure 1-8, the wire wrap around each fuel rod has been represented as a ring concentric to the rod, in which the wire's steel is homogenized with the coolant.

The implemented time steps follow the same pattern as in the 2D simulations subject of 5.1.

### 5.3.1 Results

Figure 5-30 to Figure 5-32 show the behaviour of the power distribution in the fuel rods along the burn-up in some of the simulated configurations.

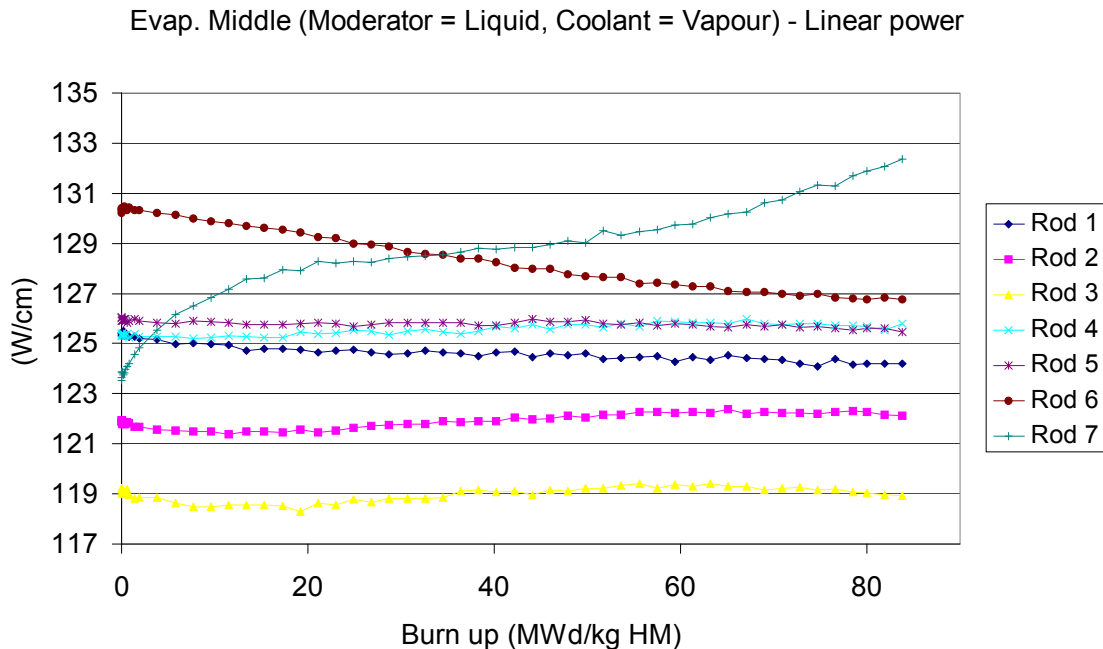


Figure 5-30: Fuel rods linear power in the middle layer of the evaporator.  $S(\alpha, \beta)$  used: Liquid for moderator, Vapour for coolant.

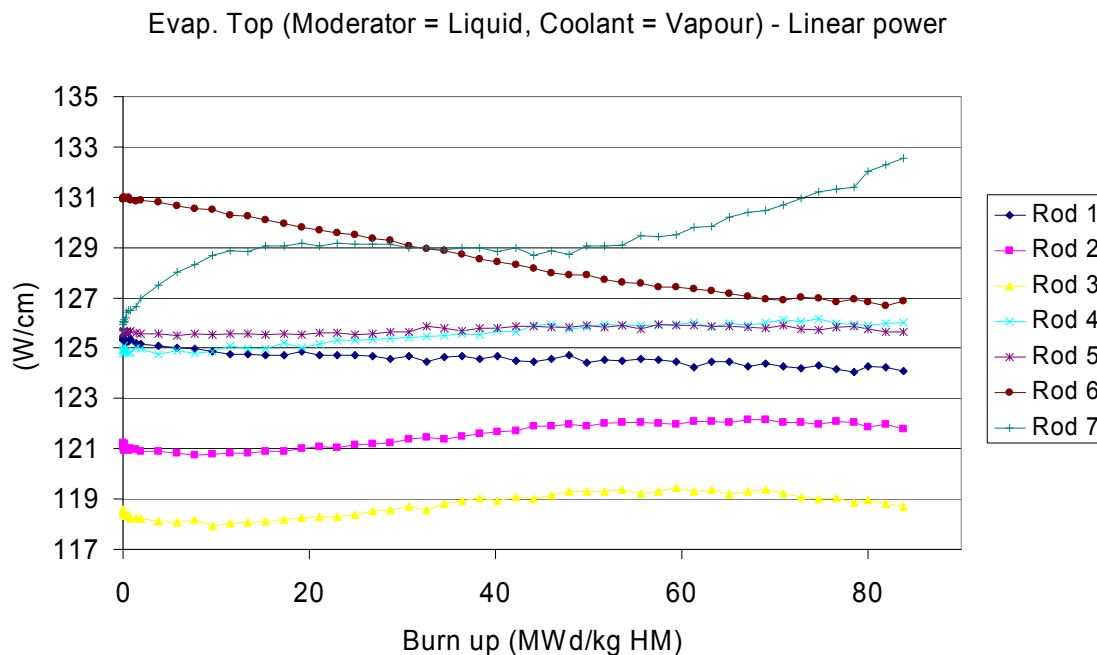


Figure 5-31: Fuel rods linear power in the upper layer of the evaporator.  $S(\alpha, \beta)$  used: Liquid for moderator, Vapour for coolant.

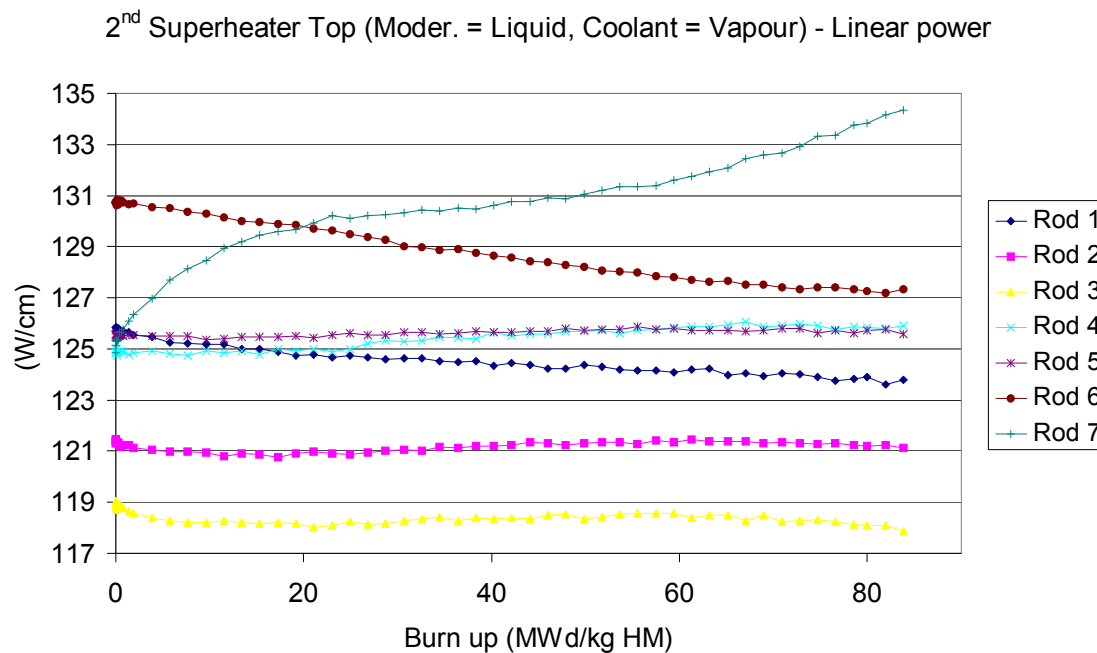


Figure 5-32: Fuel rods linear power in the upper layer of the 2nd superheater.  $S(\alpha, \beta)$  used: Liquid for moderator, Vapour for coolant.

The most apparent features that these diagrams have in common are the decreasing linear power in rod 6 and the constantly increasing power in rod 7. The rods 6 and 7 are the best moderated ones, and the flux intensities detected in their fuel are the highest from the beginning to the end of the burn-up, as shown in Figure 5-33 to Figure 5-35.

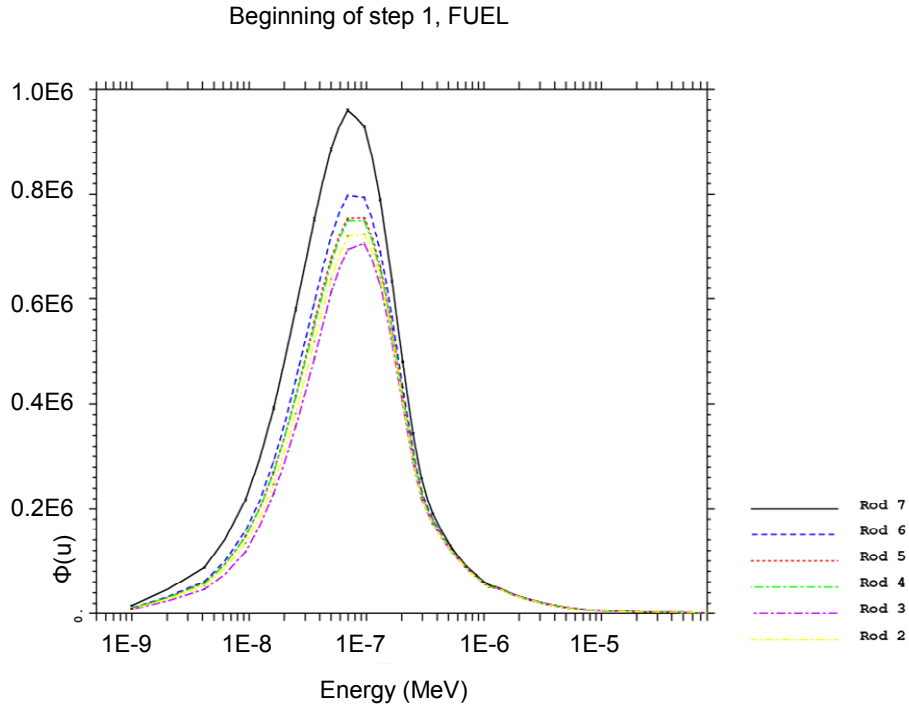


Figure 5-33: Spectra in the fuel at 0 MWd/kg HM. The flux density (per unit of lethargy) is given in normalized unit.

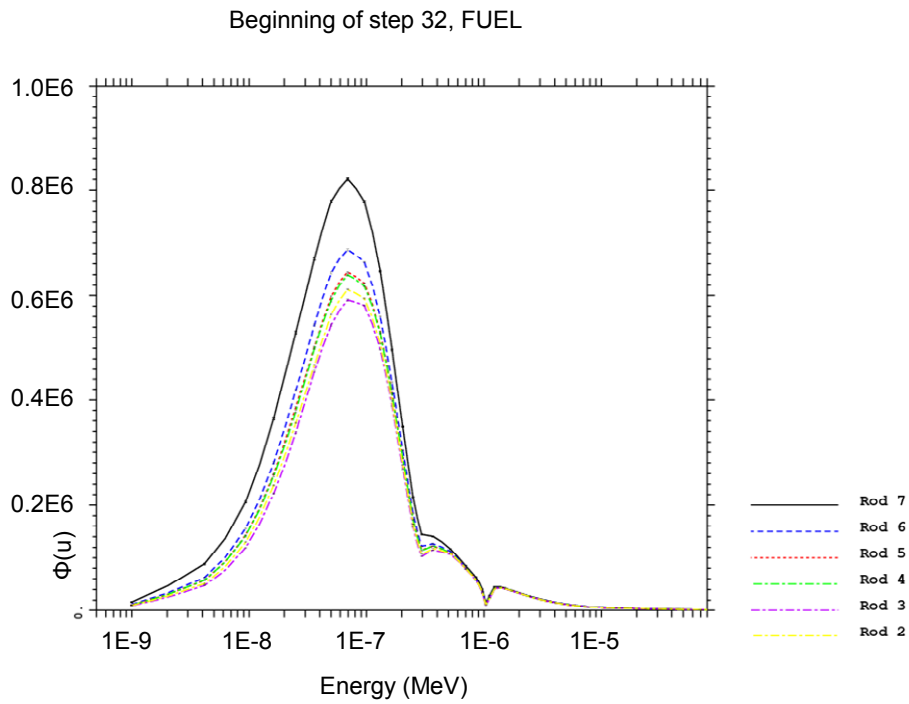


Figure 5-34: Spectra in the fuel at about 40 MWd/kg HM. The flux density (per unit of lethargy) is given in normalized unit.

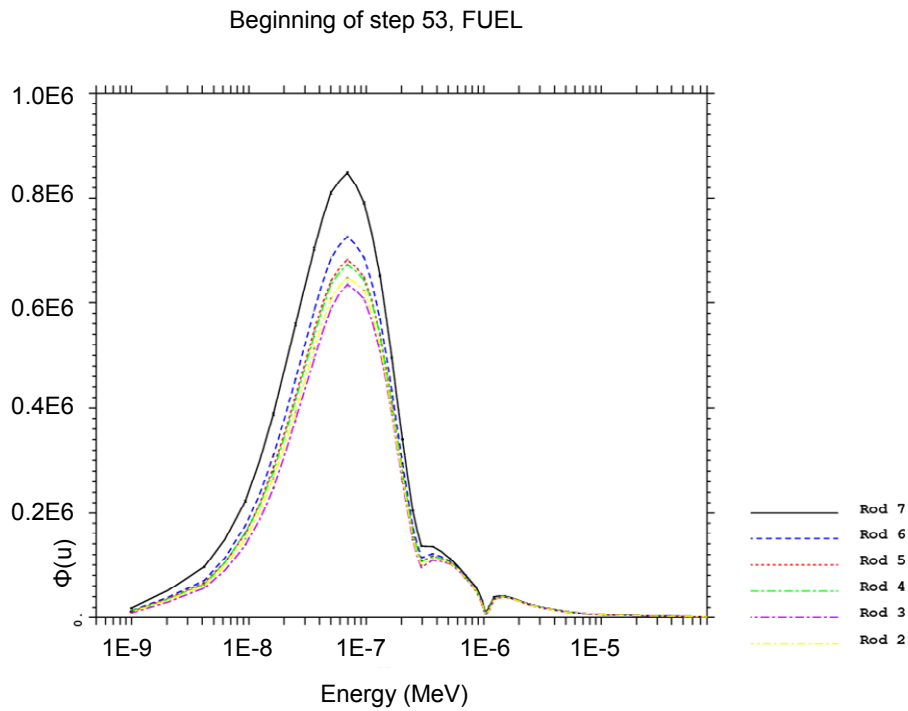


Figure 5-35: Spectra in the fuel at 80 MWd/kg HM. The flux density (per unit of lethargy) is given in normalized unit.

The high flux in rod 6 explains the highest power observed in it at the beginning, visible in Figure 5-30 to Figure 5-32. This high power implies a higher consumption of  $U^{235}$  than in the other rods which, in turn, as the burn-up rises, causes an increasing deficiency in  $U^{235}$  with respect to the less moderated rods (Figure 5-36). This explains the fact that the power progressively goes down in rod 6.

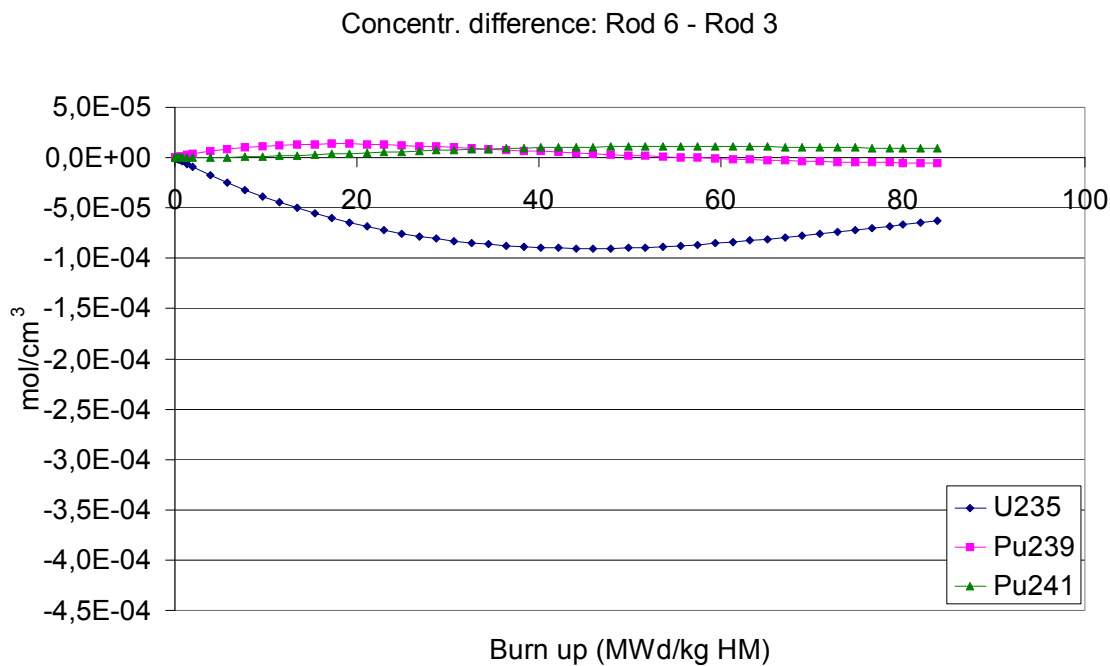


Figure 5-36: Difference of the most important actinides concentrations between the well moderated rod 6 and a second, arbitrarily chosen rod. For high burn-up, as the power in rod 6 decreases and the consumption of  $U^{235}$  as well, the difference tends to ease off.

Figure 5-37 confirms this explanation showing that the dynamics of the  $U^{235}$  concentration in the other, less moderated rods effectively is qualitatively different.

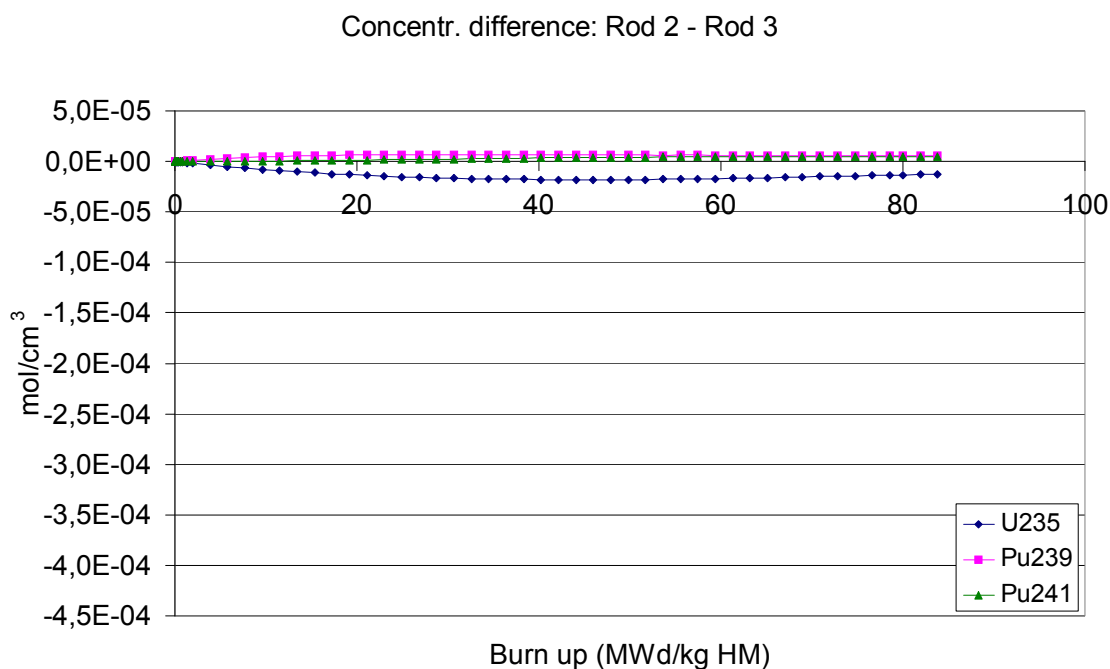


Figure 5-37: The negligible differences between two less moderated rods reveal that what happens in rod 6 is not common among the other rods.

As shown in Figure 5-30 to Figure 5-32, the highest flux in rod 7 initially doesn't suffice to compensate for the lower enrichment, so that the power is relatively low. Consistently, Figure 5-38 shows how the capture rate of  $U^{238}$  is high in rod 7.

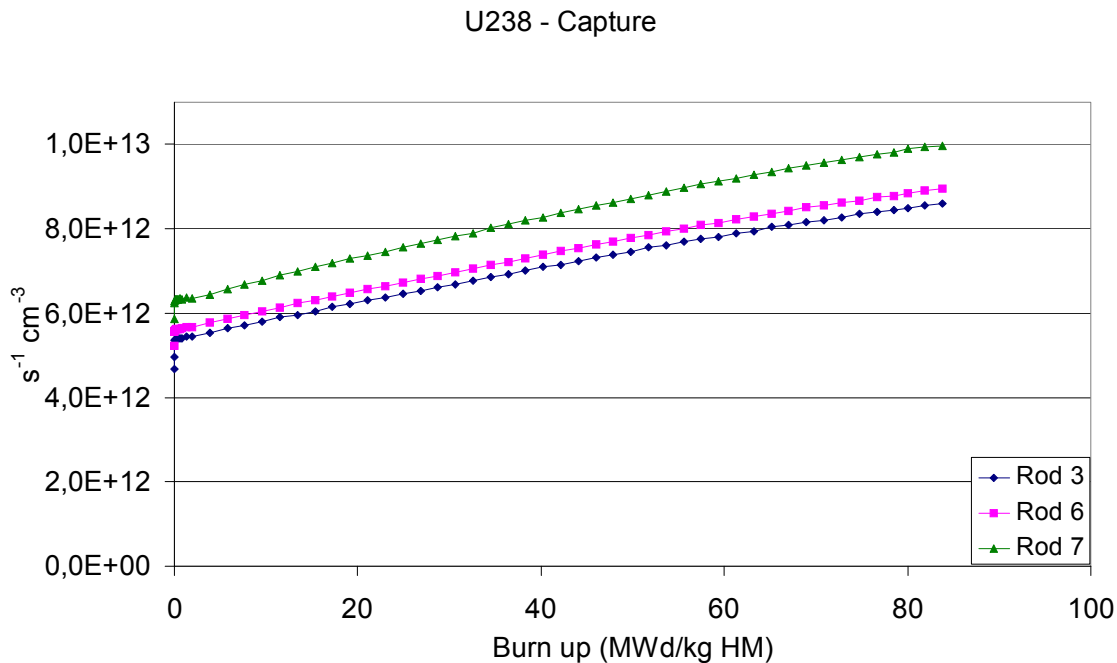


Figure 5-38: Capture rate in  $U^{238}$  in the two best moderated rods (6 and 7) and in one of the other rods (in this case rod 3).

Subsequently, the fission reaction rates in the generated fissile Plutonium isotopes before long become relevant, as shown in Figure 5-39, Figure 5-40.

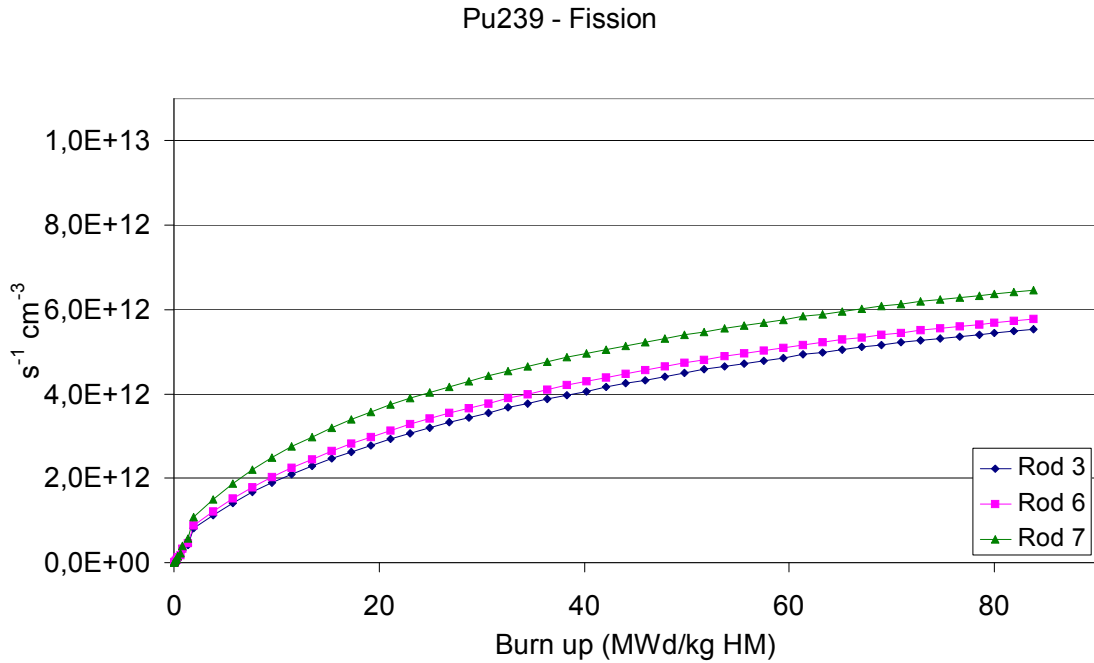


Figure 5-39: Fission rate of Pu<sup>239</sup> in the two best moderated rods (6 and 7) and in one of the other rods (in this case rod 3).

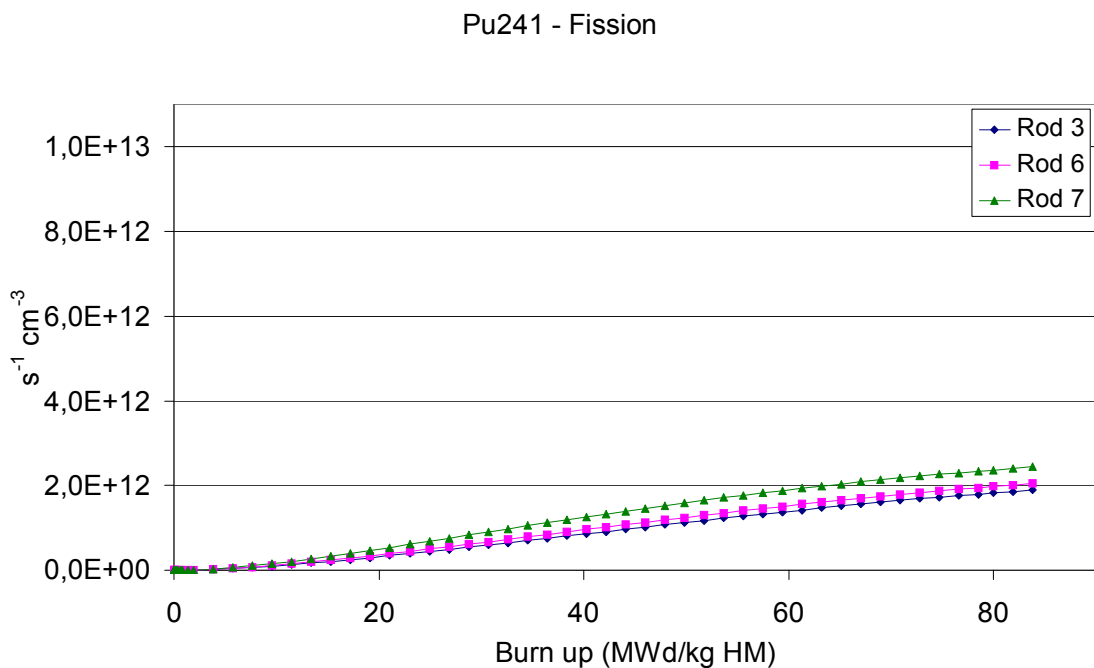


Figure 5-40: Fission rate of Pu<sup>241</sup> in the two best moderated rods (6 and 7) and in one of the other rods (in this case rod 3).

Burning more Plutonium than in the less moderated rods lets save U<sup>235</sup>, so that the enrichment lag affecting rod 7, initially large, (enrichment of 5 % with respect to 6 % in the other rods) gets progressively smaller, as shown in Figure 5-41.

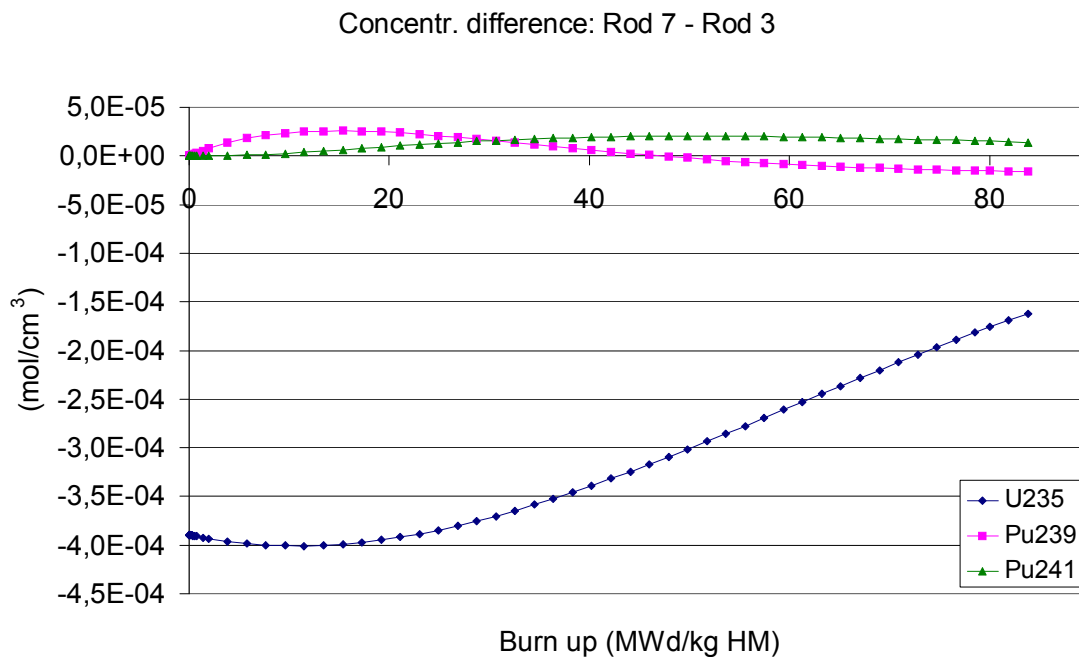


Figure 5-41: Difference between the concentration of the most important actinides in the best moderated rod and in one of the other rods (in this case rod 3).

The fact that the  $U^{235}$  abundance gap between rod 7 and the other rods gets progressively smaller could be an additional factor contributing to rod 7's increasing power along the burn-up.

On the other hand, the fact that in the bottom layer of the evaporator this phenomenon takes place to a much lesser extent (Figure 5-42), can be seen as a confirmation of the above given explanation.

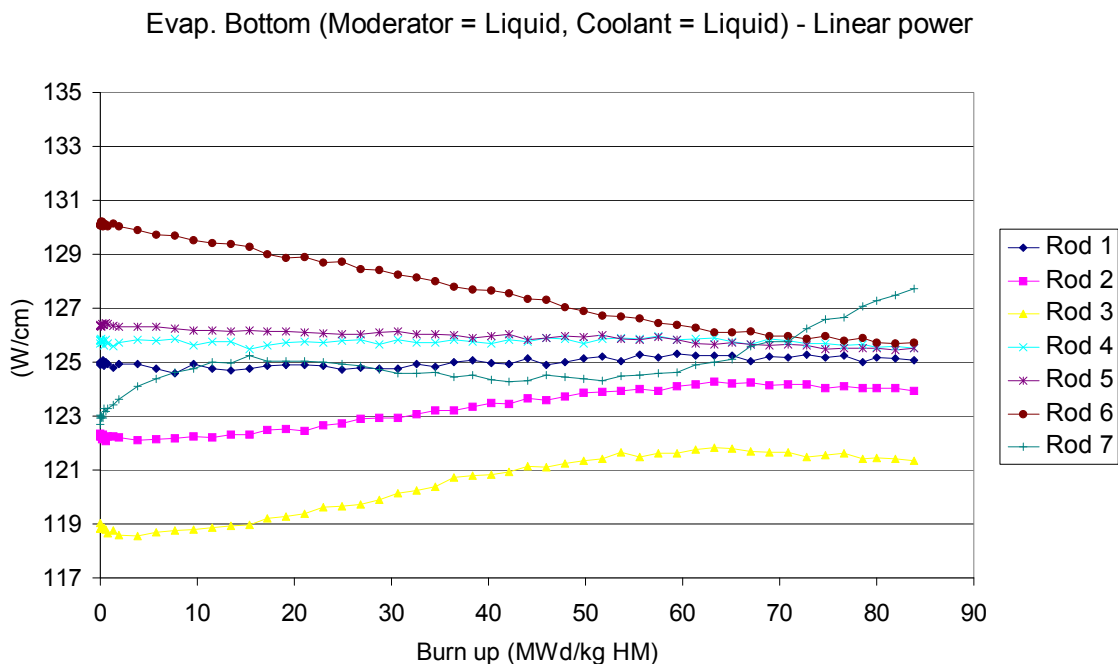


Figure 5-42: Fuel rods linear power in the bottom layer of the evaporator.  $S(\alpha, \beta)$  used: Liquid for moderator, Liquid for coolant. Note that the power excursion in rod 7 is considerably smaller than in the other considered cases.

Effectively, the evaporator's bottom layer is the only considered configuration in which the coolant temperature is still under the supercritical point, and therefore its density is still relevant. Therefore, as the coolant acts better as moderator, being in the corner is a less advantageous privilege, and all the ensuing phenomena are of a smaller magnitude.

### 5.3.2 Conclusions

The last 2D simulations have unfolded the dynamics of rod 7's heating.

The higher flux, combined with the lower enrichment, leads to larger capture rates in  $U^{238}$  and therefore to faster formation of Plutonium. This gives a massive contribution to the power production, letting save  $U^{235}$  and therefore progressively reducing rod 7's enrichment lag.

With these premises, the usage of a burnable poison could be more effective in attenuating the phenomenon than further reducing rod 7's enrichment.

It must be kept in count that these 2D simulations have been carried out imposing the same fuel temperature in every rod, and in every considered configuration. This has probably played down the gravity of the problem. In a 3D simulation in which the fuel temperatures were realistically calculated, the Doppler Effect could speed up the production of Plutonium in the hottest rod, intensifying the phenomenon.

## References

- [1] **K. Dobashi, Y. Oka, S. Koshizuka** (1998): Conceptual design of a high temperature power reactor cooled and moderated by supercritical light water. ICONE6, May 10-15, 1998.
- [2] **D. Bittermann** (2001): General plant characteristics. HPLWR project report, FIKI-CT-2000-00033-D3, European Commission, September 2001.
- [3] **X. Cheng, T. Schulenberg, D. Bittermann, P. Rau** (2003): Design analysis of core assemblies for supercritical pressure conditions, Nucl. Eng. and Design, Vol. 223, pp. 279-294.
- [4] **J. Hofmeister** (2006): Auslegung eines Brennelements für einen Leichtwasserreaktor mit überkritischen Dampfzuständen, Wissenschaftliche Berichte, FZKA-7248, Karlsruhe.
- [5] **C. L. Waata** (2006): Coupled Neutronics/Thermal-hydraulics Analysis of a High-Performance Light-Water Reactor Fuel Assembly, Wissenschaftliche Berichte FZKA 7233, Karlsruhe.
- [6] **T. J. Krieger and M. S. Nelkin** (1957): Slow-Neutron Scattering by Molecules, Phys. Rev., Vol. 106, pp. 290-295.
- [7] **A. C. Zemach and R. J. Glauber** (1956): Dynamics of Neutron Scattering by Molecules, Phys. Rev., Vol. 101, pp. 118-129.
- [8] **A. C. Zemach and R. J. Glauber** (1956): Neutron Diffraction by Gases, Phys. Rev., Vol. 101, pp. 129-136.
- [9] **R. G. Sachs and E. Teller** (1941): The Scattering of Slow Neutrons by Molecular Gases, Phys. Rev., Vol. 60, pp. 18-27.
- [10] **Mark Nelkin** (1960): Scattering of Slow Neutrons by Water, Phys. Rev., Vol. 119, pp. 741-746.
- [11] **E. Melkonian** (1949): Slow Neutron Velocity Spectrometer Studies of O<sub>2</sub>, N<sub>2</sub>, A, H<sub>2</sub>, H<sub>2</sub>O, and Seven Hydrocarbons, Phys. Rev., Vol. 76, pp.1750-1759.
- [12] *Neutron Cross Sections*, compiled by D. J. Hughes and R. B. Schwartz, Brookhaven National Laboratory Report BNL-325 (Superintendent of Documents, U. S. Government Printing Office, Washington, D. C., 1958), 2<sup>nd</sup> ed.
- [13] **B. N. Brockhouse** (1957): *Proceedings of the Conference on the Condensed State of Simple Systems, Varenna, September, 1957* [Suppl. Nuovo cimento **9**, 45 (1958)].

- [14] **H. Boutin, S. Yip** (1968): *Molecular Spectroscopy With Neutrons*, The M.I.T. Press, Massachusetts Institute of Technology, Cambridge, Massachusetts, and London, England.
- [15] **J. Keinert, M. Mattes, W. Bernnat**: Institut für Kernenergetik und Energiesysteme, University of Stuttgart (private communication).
- [16] **J. Martí** (1999): Analysis of the hydrogen bonding and vibrational spectra of supercritical model water by molecular dynamics simulations, *J. Chem. Phys.*, Vol. 110, pp. 6876-6886.
- [17] **A. K. Soper, F. Bruni, and M. A. Ricci** (1997): Site-site pair correlation functions of water from 25 to 400 °C: Revised analysis of new and old diffraction data, *J. Chem. Phys.*, Vol. 106, pp. 247-254.
- [18] **John E. Bertie, M. Khalique Ahmed, Hans H. Eysel** (1989): Infrared intensities of liquids. 5. Optical and dielectric constants, integrated intensities, and dipole moment derivatives of water and water-d<sub>2</sub> at 22.degree.C, *J. Phys. Chem.*, Vol. 93, pp. 2210-2218.
- [19] **L. Lanz, L. G. Molinari, M. Raciti** (2008): *Introduzione alla fisica teorica*, vol. I. C.U.S.L., Milano, Italy.
- [20] **L. Lanz, B. Vacchini** (2007): *Introduzione alla Fisica Teorica*, vol. II. C.U.S.L., Milano, Italy.
- [21] **E. Pedrocchi, M. Silvestri** (1991): *Introduzione alla TERMODINAMICA TECNICA*, CittàStudi, Milano, Italy.
- [22] **M. M. R. Williams** (1966): *The Slowing Down and Thermalization of Neutrons*, North-Holland Publishing Company, Amsterdam.
- [23] **V. F. Turchin** (1965): *Slow Neutrons*, Israel Program for Scientific Translations, Jerusalem.
- [24] **A. G. Croff** (1980): *ORIGEN2-A Revised and Updated Version of the Oak Ridge Isotope Generation and Depletion Code*, ORNL-5621, Oak Ridge National Laboratory, Oak Ridge, Tennessee.
- [25] **A. M. Mood, F. A. Graybill, D. C. Boes** (1996): *Introduzione alla statistica*, McGraw-Hill Libri Italia srl, Milano, Italy.
- [26] **MCNP4C Monte Carlo N-Particle Transport Code System (User's manual)**, Oak Ridge National Laboratory.

## Erklärung

Hiermit erkläre ich, dass ich die vorliegende Doktorarbeit selbständig angefertigt habe. Es wurden nur die in der Arbeit ausdrücklich benannten Quellen und Hilfsmittel benutzt. Wörtlich oder sinngemäß übernommenes Gedankengut habe ich als solches kenntlich gemacht.

---

Ort, Datum

---

Unterschrift



Institut für Kernenergetik und  
Energiesysteme

Universität Stuttgart

Pfaffenwaldring 31

D-70550 Stuttgart

